Evaluation of Wear Rate and Mechanical Properties of Platinum-Graphene Nano-Composite by Molecular Dynamics Simulation

A Dissertation
by

Mohammad Din Al Amin
1017102074

Under the supervision of

Dr. Mohammad Abdul Motalab

MASTER OF SCIENCE IN MECHANICAL ENGINEERING

Department of Mechanical Engineering
Bangladesh University of Engineering and Technology

Dhaka, Bangladesh

July, 2023

This thesis titled, **"Evaluation of Wear Rate and Mechanical Properties of Platinum-Graphene Nano-Composite by Molecular Dynamics Simulation"**, submitted by Mohammad Din Al Amin, Roll No.: 1017102074, Session: October 2017, has been accepted as satisfactory in partial fulfillment of the requirement for the degree of MASTER OF SCIENCE in Mechanical Engineering on 15th July, 2023.

BOARD OF EXAMINERS

Dr. Mohammad Abdul Motalab **Professor** **Dept. of Mechanical Engineering, BUET, Dhaka-1000**	**Chairman** **(Supervisor)**
Dr. Muhammad Ashiqur Rahman **Professor and Head** **Dept. of Mechanical Engineering, BUET, Dhaka-1000**	**Member** **(Ex-Officio)**
Dr. Mohammad Jane Alam Khan **Assistant Professor** **Dept. of Mechanical Engineering, BUET, Dhaka-1000**	**Member** **(Internal)**
HRashed **Dr. H. M. Mamun Al Rashed** **Associate Professor** **Dept. of MME, BUET, Dhaka-1000**	**Member** **(External)**

Candidate's Declaration

This is to certify that the work presented in this thesis entitled, "Evaluation of Wear Rate and Mechanical Properties of Platinum-Graphene Nano-Composite by Molecular Dynamics Simulation", is the outcome of the research carried out by Mohammad Din Al Amin under the supervision of Dr. Mohammad Abdul Motalab, Professor, Department of Mechanical Engineering, Bangladesh University of Engineering and Technology (BUET), Dhaka-1000, Bangladesh.

It is also declared that neither this thesis nor any part thereof has been submitted anywhere else for the award of any degree, diploma, or other qualifications.

Signature of the Candidate

Md. Din Al-Amin

Mohammad Din Al Amin
1017102074

Dedication

First and foremost I would like to dedicate this study to the science communities worldwide which have helped me in every aspect of this study with their knowledge and without its advancement the study was not possible. I would also like to dedicate this to my family and my supervisor Dr. Mohammad Abdul Motalab for their unconditional support throughout this journey. And lastly this study is dedicated to everyone who has helped me with their goodwill.

Contents

List of Figures

List of Tables

List of Abbreviations

BC	Boundary Condition
EAM	Embedded Atom Method
Gr	Graphene
LAMMPS	Large-scale Atomic/Molecular Massively Parallel Simulator
LJ	Lennard-Jones
MD	Molecular Dynamics
MMNC	Metal Matrix Nanocomposite
NC	Nanocomposite
NW	Nanowire
OVITO	Open Visualization Tool
PEMFC	Proton Exchange Membrane Fuel Cell
Pt	Platinum

Acknowledgement

First and foremost, I would like to express my sincerest appreciation and thanks to my supervisor, Dr. Mohammad Abdul Motalab, who was abundantly helpful and offered invaluable assistance, support and guidance. I would like to convey my gratitude to Bangladesh University of Engineering and Technology for providing the financial support and high-performance computing facilities. Special thanks are also due to the numerous teachers and mentors who helped me to compile the softwares/codes in the high performance computer. Also, thanks to the Department of Mechanical Engineerin, BUET for facilitating all the support. At last, thanks to all the people who have encouraged and helped me in this study both directly and indirectly.

Abstract

As the energy industry develops and natural resources become more scarce, scientists are focusing their attention on finding new materials where comes the emergence of nanocomposites and their applications in various sectors. Despite the increase in the discovery of novel nanocomposites, assessment of their mechanical and tribological characteristics is limited owing to the intricacy of their structures.

In this study, one of the main goals is to evaluate the mechanical properties of platinum graphene nanocomposites (Pt-Gr NC) using molecular dynamics simulation. Pt-Gr NC was chosen for this study because of the extraordinary qualities of graphene as a fiber and platinum's use in energy storage systems and other disciplines, such as biomedical and industrial ones. The study began with the material design and finding its proper interaction potentials. Then MD simulations of the system for both tensile and bending testing were done to find its mechanical properties, and the results showed that the mechanical properties of Pt were improved with the inclusion of graphene fiber. Almost a 35% of increment in Young's modulus occurred with the inclusion of single layer of graphene with platinum. Validation of the results was also done with previously developed equation of mixture for bulk composites. After investigating the material's mechanical characteristics and failure processes, it was found that Pt-Gr NC performed as predicted when subjected to tensile loads but badly when subjected to lateral loads. In addition, the effect of additional graphene layers and temperature variation on the mechanical properties of the Pt-Gr NC were eventually investigated. MD simulation being a perfect method for studying the underlying complex behavior of friction and wear, a study of the tribological properties of this selected nanocomposite was also conducted. The change in coefficient of friction due to temperature variation showed a decreasing trend. The effect of variations in sliding velocity on friction and how a higher sliding velocity led towards material wear were also studied. The effect of wear rate due to different normal loads, as well as a comparison of wear rate with pristine platinum, were also investigated in this study. Results showed that, wear rate for Pt-Gr NC is higher than pristine Pt at different indentation depth.

This study yields results applicable to the disciplines of nanocomposite and nanotechnology. Information on the mechanical properties and tribological characteristics of the Pt-Gr nanocomposite can help in the design and fabrication of supercapacitors, fuel cells, biosensors, etc., where this material is generally used. The research results could also help figure out what materials could be used instead to make structures stronger and more durable.

Chapter 1

Introduction

Over the last several decades, designers of composite materials have focused primarily on increasing the strength and modulus of structures, which they have done by creating a wide variety of composites [5, 6]. Composites' capacity to have their physical and mechanical characteristics precisely managed is one of their most valuable qualities. Composite materials in which both the metal and reinforcing particles have at least one dimension at the nanoscale are known as metal-based nanocomposites [7]. Nanocomposites made of metal-carbon exhibit special characteristics due to the combination of the favorable properties (lightweight, abundance, flexibility) of carbon and the ideal physical-mechanical properties of nanoparticles [8].

1.1 Problem Statement

Graphene, a two-dimensional carbon material, has attracted interest for both theoretical and applied investigation because of its outstanding mechanical strength [9], ultralow friction [10, 11], and good thermal conductivity [12, 13]. The extraordinary electromechanical properties of graphene have been used to create cutting-edge nanocomposites. In addition, integrating graphene into composites provides a technique for scaling up graphene's nanoscale electromechanical properties to the microscale and macroscale [14]. Graphene is a strong substance that is both lightweight and flexible. It possesses the greatest known intrinsic strength of 130 GPa and the highest known Young's modulus of 1 TPa [15]. Therefore, graphene can be used as an emerging fiber for Metal Matrix Nanocomposties (MMNC).

Platinum-based composites, reinforced by graphene, recently have attracted substantial attention as the Pt acts as spacers resulting in mechanically exfoliated, high-surface-area material of potential interest for supercapacitors and fuel cells [16]. Even in electronic industries, Pt has been used in production of computer hard disks, thermocouples, optical fibers, LCDs, etc [17]. Graphene's strong conductivity allows it to operate as a fiber in a Pt matrix. According to research, adding graphene to metals increases their tensile strength and decreases their coefficient of friction [18]. Pt-Graphene nanocomposites are also used as biosensors in the biotechnology, clinical diagnostics, and food industries [19].

In spite of the fact that it is a valuable material in a variety of applications, there is still a shortage of published research that focuses on the assessment of the mechanical characteristics of Pt-Graphene nanocomposites. As a result, the purpose of this work is to evaluate the mechanical characteristics of Pt-Graphene nanocomposites using tensile and bending tests by employing atomistic modeling. These mechanical parameters include Young's modulus and ultimate strength. In the course of this study, examinations of tribological characteristics will also be carried out.

1.2 Objectives of the Thesis

The objectives of the present work can be summarized as follows:

(i). To evaluate the mechanical properties such as Youngs modulus, Yield strength, etc. of graphene reinforced Pt metal matrix nanocomposite using LAMMPS.

(ii). To investigate how the mechanical properties change by varying the amount of graphene in the nanocomposite.

(iii). To investigate change in mechanical properties due to variation of ambient temperatures.

(iv). To evaluate the flexural properties of the nanocomposite by performing three point bending simulation.

(v). To evaluate the effect of graphene on the wear rate of the nanocomposite to study the improvement in the material tribology.

(vi). To validate the atomistic model by simplifying it to the pristine Pt case and then comparing the results with that available in literature.

1.3 Thesis Outline

The introductory chapter provides the background, problem statement and its possible outcome, and the objectives of this study. The discussion about the previous studies on the topic discussed and how ended up finding a particular gap to be studied in this thesis is done on chapter 2.

Chapter 3 begins with the discussion on the two main hurdles (a) initial material design (b) proper interaction potential selection, and how it is tackled in this study. Then it proceeds with basics of molecular dynamics simulation.

The main study commences from chapter 4, where the mechanical properties are evaluated through tensile testing. Chapter 5 extends this study with bending test and comparison between tensile and bending tests. In the walk, effects of change in different parameters on the mechanical properties of nanocomposites are studied.

Tribological properties of Pt-Gr NC are evaluated in the following chapters (Ch. 6 and Ch. 7). Along with the parametric studies, every chapter from 4 to 7 are consisted of theoretical background and simulation methodology. Finally conclusions of the study mentioned in chapter 8.

Chapter 2

Literature Review

High electrical conductivity is one of the primary characteristics of platinum graphene nanocomposites (Pt-Gr NC), which makes them attractive for use in a variety of electronic and energy storage applications. Due to the inadequacy in the availability of platinum, which is an excellent catalyst for fuel cells, researchers have come up with a solution by using it as a nanoparticle. Platinum NPs as small as 0.9 nm can be employed to replace a solid Pt sheet without losing catalytic activity due to quantum size effects [20, 21]. Graphene may provide the ideal support for Pt NP catalysis, with its unmatched electrical conductivity, strength, and surface-to-volume ratio [22, 23]. In addition, theoretical studies have predicted that by placing certain elements on graphene, enhanced catalytic reactions can be achieved [24]. According to the findings of physicists, the interfacial interaction between graphene and Pt NPs is very sensitive to the NPs' shape, size, and contact details [25]. It is challenging to model this system since temperature changes the shape of suspended graphene, the adsorption process, and the binding energy [26].

The synthesis of platinum graphene nanocomposites has been investigated via chemical reduction, electrodeposition, and plasma-assisted deposition, among others. Xu et al. [27] studied the interaction between Pt and graphene nanosheets in an experiment. This research has shown that these nanostructures are sufficiently stable to be used in electrical devices.

Pt-Gr NCs have been studied for a variety of applications, including fuel cells, lithium-ion batteries, and supercapacitors. Although proton exchange membrane fuel cells (PEMFCs) are an appealing advancement in the energy industry, commercialization of PEMCFCs is extremely difficult [28–30]. The reasons for this are (i) the degradation of Pt-base catalysts due to heavy carbon support corrosion, and (ii) the lack of an effective triple-phase boundary, which is required for PEMFCs, so trapped Pt NPs in carbon micropores cannot work [31–33]. Using a combination of graphene and Pt nanoparticles, Daping et al. produced a novel catalyst with optimum efficiency, which considerably increases the likelihood that graphene nanosheets may be used as catalyst supports in proton exchange membrane fuel cells [34]. Additionally, in computational research using molecular dynamics (MD), Feng et al. [35] examined the impact of graphene nanoparticles in a Pt atomic structure on the optimization of traditional chemical catalysts. The findings of these simulations indicate that the inclusion of graphene nanoparticles improves the catalytic performance of the original structures [35].

In fuel cells, platinum graphene nanocomposites have been shown to have higher electrocatalytic activity and stability for oxygen reduction reactions, which are important for the performance of the fuel cell. Divya et al. [36] simulated the spontaneous arrangement of Pt atoms in graphene nanosheets. The findings indicate that this nanostructure is a viable contender for use as a proton transporter in a fuel cell [36]. In lithium-ion batteries, Pt-Gr NCs have been used as electrodes for both the anode and cathode and have been shown to improve the charge/discharge rate and capacity of the battery [37, 38]. In supercapacitors, platinum graphene nanocomposites have been used as electrodes and have demonstrated high energy density and power density [39].

In one experiment, Berghian-Grosan et al. [40] evaluated the influence of graphene nanoparticles on the physical and catalytic behavior of the Pt matrix. This work demonstrates the stability of graphene nanoparticles inside a Pt matrix. In contrast, the incorporation of these nanoparticles into the Pt matrix enhances the atomic structure's physical behavior [41]. Moreover, Divya et al. examined the hydrogen storage capacity of the Pt-Gr nanocomposite [42]. This study reveals that Pt-Gr nanocomposite is a viable hydrogen storage material.

Due to their benefits, dye-sensitized solar cells (DSSCs) have garnered considerable attention [43]. Here, Pt is used as a counter electrode (CE) which is used for catalyzing the redox couple regeneration and collecting electrons [44, 45]. In an experimental study, Cheng et al. [43] report that the photovoltaic performance of DSSCs improved with graphene-incorporated CEs as the location and thickness of graphene were optimized. Specifically, this composite structure performs well in the transfer of charge carriers in solar cells [43]. In an experimental investigation, Wang et al. produced a Pt and graphene nanosheet composite. These structures function suitably in the region of oxygen molecule adsorption, which has several commercial uses, according to the results of this study [46].

Literature reveals that platinum graphene nanocomposites have the potential to considerably enhance the performance of a variety of energy-related technologies, such as fuel cells, batteries, and supercapacitors. On the other hand, improving the mechanical behavior of the Pt matrix (due to its biocompatibility), which has many uses in medical applications, can be very effective in the healing process of patients [41]. However, more study is required to improve their synthesis and performance, and to completely comprehend their action processes. A molecular dynamics study of the Pt-Gr NC for its mechanical properties as well as tribological properties is still lacking. Particularly, friction and wear mechanisms at the nanoscale are difficult to realize due to their underlying complexities, where MD simulations can be a possible solution. Furthermore, the effects of the number of graphene nanosheets and the atomic ratio of this type of nanocomposites have not been yet studied using this technique. In this work, the MD simulation has thus investigated the mechanical behavior of Pt-graphene nanocomposites. Also, researchers have shown that the addition of graphene to metals reduces the friction coefficient and wear rate while enhancing tensile strength [18]. So, tribological properties through MD simulations are also studied for the Pt-Gr NC in this research.

Chapter 3

Molecular Dynamics Simulation

Newton's equations (or analogous equations) employ an empirical model (interatomic potential) to describe the interactions between atoms in a molecular dynamics (MD) simulation. One can think of an atom, or a collection of atoms, as a distinct particle with its own mass and charge. Newton's second law is described by:

$$F = ma \tag{3.1}$$

here, F denotes the force acting on each atom, atomic mass is denoted by m and a is the acceleration of atoms. The above equation can be written as,

$$-\nabla E = m(\delta^2 r/\delta t^2) \tag{3.2}$$

Here, atomic position (r), time (t), and the potential energy (E) experienced by each individual atom. A particle moves forward in time by a small amount, denoted by the symbol t, since the forces acting on it have been determined. All of the atoms in the system go through this process for a fixed number of iterations. The position can be fetched by time-integrating the velocity, and the acceleration can be fetched by doing the same with the velocity.

In order to numerically solve both equations, the domain must be discretized into discrete steps δt, and the inner region of the function must be approximation. The value of δt is decided by finding a balance between the approximation uncertainty and the computational costs. The Velocity Verlet and Leapfrog algorithms are the most popular and easy-to-understand numerical strategies for time-integration. Furthermore, the Adams and Nordsieck procedures are two other prevalent kinds of examples. [1,47]

3.1 Initial Positions:Material Design

The first step in designing a system for molecular dynamics simulation is to define the initial position of the atoms. This can be done by adopting a lot of different methods. The simplest of them is to define the atomic positions explicitly in three dimensions by writing a file projecting the positions as numerals. However, with the increasing difficulty of the system, it becomes tiresome to write the positions explicitly. For this simulation work, a NanoComposite (NC) system will be designed containing platinum (Pt) and graphene (Gr) layers stacked one upon another. For the sake of simplicity in designing the system, atomsk will be used [48].

For different size and layered NC system, the atomsk codes had to run over and over again. To solve this issue, a jupyter notebook was developed for making this iterative process simple. In this section, the steps in making the initial system will be described briefly along with the snippets of python codes.

First of all, some of the parameters for Gr and Pt sheets were given and the basic size of the system were stored.

```
# Parameters for graphene
c_c_bond = 1.41
graphene_x = c_c_bond*2*math.cos(math.pi/6)
graphene_y = c_c_bond*2*(1+math.cos(math.pi/3))

# Storing the values of calculated graphene parameters
graphene_x_value = graphene_x
graphene_y_value = graphene_y

# * Platinum Block Size *
block_x = input("x-direction: ")
block_y = input("y-direction: ")
block_z = input("z-direction: ")

pt_lattice = 3.9239

# * Graphene Block Size *
# * This will generally be matched with the x and y value of Platinum *
graphene_x_lattice = graphene_x_value
graphene_y_lattice = graphene_y_value

# Graphene values for duplicating in other directions
# These values has to be integers
Graphene_x = (int(block_x) / graphene_x_lattice)
Graphene_y = (int(block_y) / graphene_y_lattice)
```

```
# Platinum values for duplicating in other directions
Platinum_x = int(block_x) / pt_lattice
Platinum_y = int(block_y) / pt_lattice
Platinum_z = int(block_z) / pt_lattice
```

Afterwards, the initial graphene sheet will be designed from a graphite block (Fig. 3.1) using the following code.

```
g_str1 = 'atomsk --create graphite '
          + str(graphene_x_lattice)
          + ' ' + str(graphene_y_lattice)
          + ' C -cut below 0.2 Z -orthogonal-cell g_1.cfg'
subprocess.run(g_str1, shell = True)

g_str2 = 'atomsk g_1.cfg -duplicate '
          + str(round(Graphene_x))
          + ' ' + str(round(Graphene_y)) + ' 1 g_2.cfg'
subprocess.run(g_str2, shell = True)

subprocess.run('atomsk g_2.cfg -center com g_3.cfg'
               , shell = True)
subprocess.run('atomsk g_3.cfg -disturb 0 0 0.1 g_base.cfg'
               , shell = True)
```

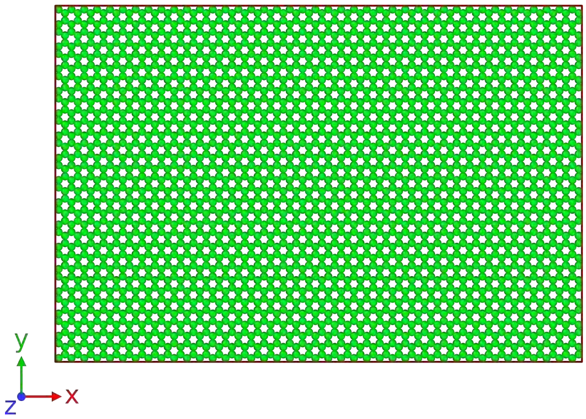

Figure 3.1: Formation of the graphene sheet.

Then, the Pt block (Fig. 3.2) for each layer is designed as follows:

```
p_str = 'atomsk --create fcc 3.9239 Pt -duplicate '
         + str(round(Platinum_x)) + str(' ')
         + str(round(Platinum_y)) + str(' ')
         + str(round(Platinum_z)) + ' pt_1.cfg'
subprocess.run(p_str, shell = True)
subprocess.run('atomsk pt_1.cfg -center com pt_base.cfg'
```

```
                    , shell = True)
```

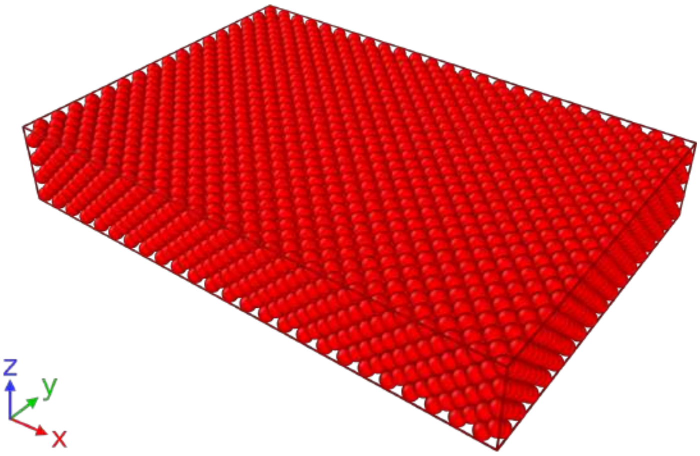

Figure 3.2: Formation of Platinum block.

Lastly, the desired number of Gr layers were merged with the Pt block as sandwiched system as shown in the Fig. 3.3 and Fig. 3.4

```
# Define the number of graphene layers
g_layer = input("Number of Graphene layers: ")

# Merging the Gr sheets with Pt blocks
subprocess.run('atomsk --merge z 3 pt_base.cfg g_base.cfg
            pt_base.cfg ini_NC.cfg', shell = True)
subprocess.run('atomsk --merge z 2 g_base.cfg pt_base.cfg
            duplicator.cfg', shell = True)

if int(g_layer) == 1 :
        os.rename('ini_NC.cfg', 'NC.cfg')
else:
        os.rename('ini_NC.cfg', 'NC1.cfg')
        for layer in range(int(g_layer) - 1):
                layer_str = 'atomsk --merge z 2 NC'
                        + str(layer+1)
                        + '.cfg duplicator.cfg NC'
                        + str(layer+2) + '.cfg'
                subprocess.run(layer_str, shell = True)
        file_name = 'NC' + str(g_layer) + '.cfg'
        os.rename(file_name, 'NC.cfg')

# Cutting the extra portions to have uniform shape
# Without cutting the extra portion may lead to
# failed boundary condition
cut_x = 'atomsk NC.cfg -cut above '
        + str(Platinum_x * pt_lattice) + ' x NC_x.cfg'
```

```
cut_y = 'atomsk NC_x.cfg -cut above '
        + str(Platinum_y * pt_lattice) + ' y NC_c.cfg'
```

```
subprocess.run(cut_x , shell = True)
subprocess.run(cut_y , shell = True)
subprocess.run('atomsk NC.cfg -center com F_NC.cfg'
                , shell = True)
```

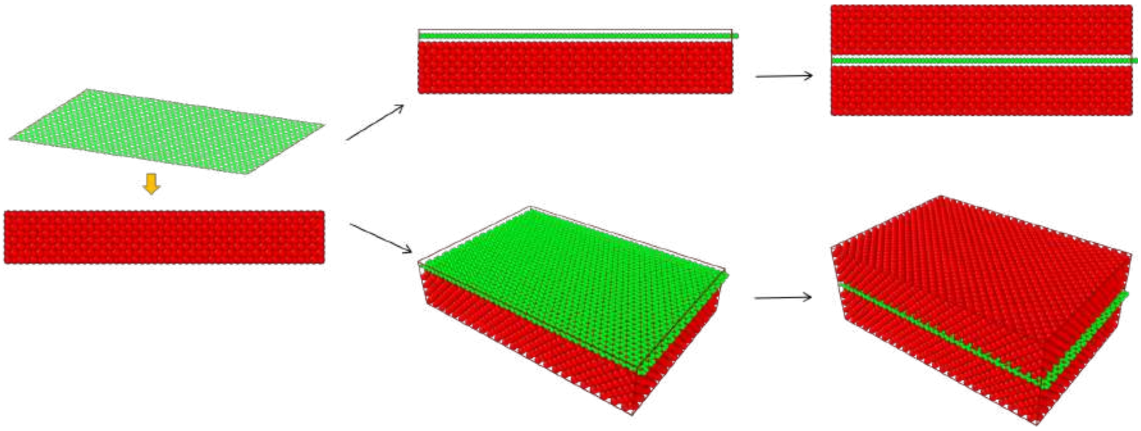

Figure 3.3: Formation of monolayered Pt-Gr NC (both perspective and front view)

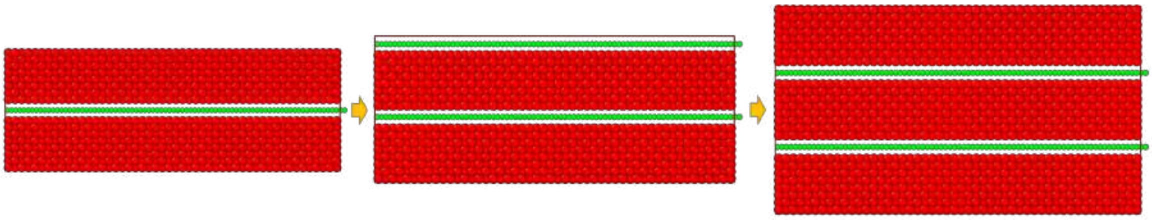

(a) Front view

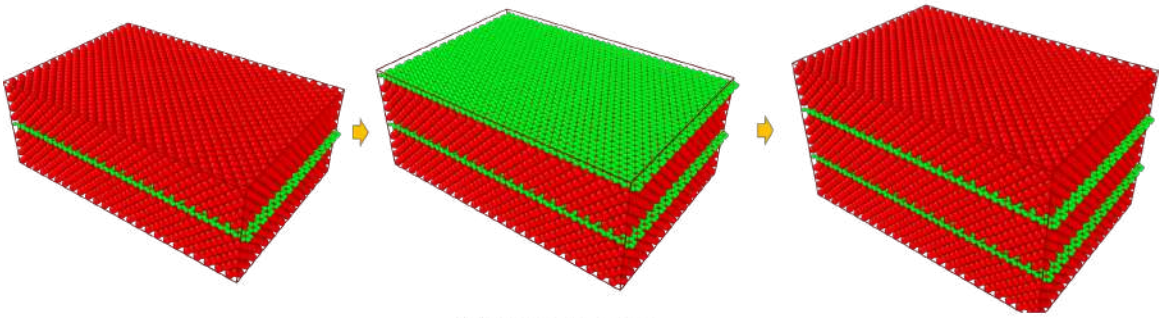

(b) Perspective view

Figure 3.4: Formation of double layered Pt-Gr NC.

3.2 Interatomic Potentials

When deciding on a potential, one must take into account the overall objectives of the study. The idea is to find candidates that describe the properties of the material of interest, going with the most natural fit [4]. The Lennard-Jones potential (LJ), proposed by John Edward Lennard-Jones in 1924, is a good illustration of a generic empirical potential [49]. According to the following relation, the LJ potential only describes van der Waals interactions and Pauli repulsion forces:

$$V(r) = 4\epsilon \left[(\frac{\sigma_D}{r})^{12} - (\frac{\sigma_D}{r})^{6} \right] \tag{3.3}$$

Here, σ_D represents a constant for the distance, making the interatomic potential zero; the well depth of energy is ϵ; and r is the distance between atoms. The Pauli repulsion at very close range is described by the first term, and the van der Waals interactions are described by the second term. The computational efficiency of these generic potentials is excellent, but they do not accurately represent all of the properties of real materials [4].

There are mainly three types of materials, namely metals, covalent materials, and ionic compounds, for the molecular dynamics study of mechanical and tribological properties. These three categories are distinguished from one another on the basis of the bonding properties they possess and serve as limiting cases in a van Arkel-Ketelaar, also known as a bond triangle [4]. To account for the interaction between atoms and between an atom and its free electrons, the Embedded Atom Method (EAM) [50, 51] incorporates a set of atom-specific parameters. It is typical practice to use this potential when dealing with metals [4]. Ionic materials must account for long-range interactions (Coulomb forces), which increases computational expenses. Valence electrons form directional bonds in covalent substances; Stillinger-Weber [52] is an example of the potential for this type of material. The bond-order potentials were produced by including a bond-order parameter in the original potential. This allows for the strength of multiple bonds to be evaluated simultaneously using just a single potential, despite the high computational cost of bond-order potentials and the widespread use of parallel implementations [4].

3.2.1 Interatomic Potential for Pt (Metal Matrix)

The EAM potential is the one that is used most frequently for any metal [53–55]. It is the most effective way to describe the metallic bond because it is able to capture the many body effects that are present in metals using a function that describes the amount of energy needed to embed an atom in the background electron density that is produced by its neighbors. To put it another way, EAM considers the issue from the point of view of the total energy and takes into account two contributions: the interatomic interaction that occurs between two atoms, as well as the embedding energy that occurs as a result of the interaction that occurs between an atom and the free electron sea [4]. The EAM potential model [56] can be expressed in its functional form as follows:

$$E_i = F_\alpha\left(\sum_{i\neq j}\rho_\beta(r_{ij})\right) + \frac{1}{2}\sum_{i\neq j}\phi_{\alpha\beta}(r_{ij}) \tag{3.4}$$

Here, r_{ij} = distance between atom i and j, $\phi_{\alpha\beta}$ = pair wise potential function, ρ_β = contribution to the electron charge density from atom j of type β at the location of atom j, and F_α = embedding function [57].

As a result, for the purpose of this research, a group of potentials was chosen to investigate the interaction of Pt. To validate the selection of potential, a strain controlled tensile test MD simulation was conducted on a Pt sample of 9.80975 nm X 6.67063 nm X 3.53151 nm volume. From the previous studies, a suitable strain rate of 1e9 gives Young's modulus for a Pt sample to be around 138.52 GPa, whereas the theoretical value is 168 GPa [57].

To start with, the EAM potential proposed by Zhou et al. [58] was used and check the value of Young's modulus obtained from the simulated stress-strain curve (Fig. 3.5)

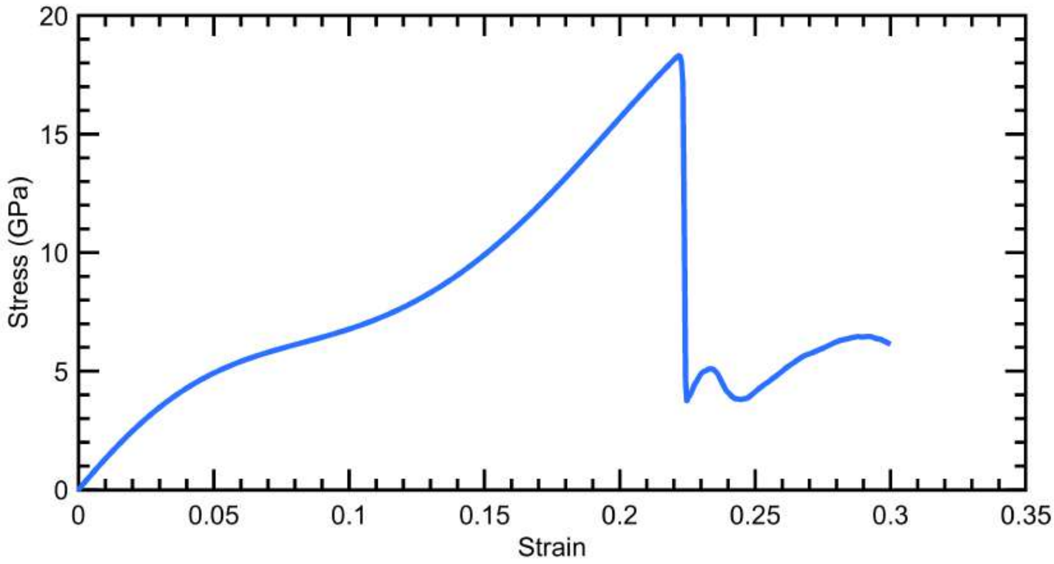

Figure 3.5: Stress-Strain curve for Pt NW using potential by Zhou et al.

The stress-strain curve using this potential is not giving out what it is opted to be. As can be seen, around a strain of 0.05 the stress has shown an anomalous behavior. Instead of yielding, it starts to showing hardening effect despite having a flow of dislocation after some steps. Although the initial part having a Young's modulus of 142.153 GPa seems to be correct, the overall curve does not go properly with how a system of Pt NW should be acted like. Therefore, I have discarded this potential for this study.

For the next set of potentials, optimizing this interatomic interactions using quantum corrected Sutton-Chen (Q-SC) type potentials was done. In a bulk solid state, the interaction between metal atoms can be described by the Sutton-Chen potential [59]. Many properties of metals and alloys can be described accurately by using these potentials, which represent many-body interactions and have parameters optimized to describe the lattice parameter, cohesive energy, bulk modulus, elastic constants, phonon dispersion, vacancy formation energy, and surface energy [60]. For a system of atoms, the potential energy according to Q-SC type potential is given by:

$$U = \epsilon_{pp} \sum_{i=1}^{N} \left[\frac{1}{2} \sum_{j \neq i}^{N} \left(\frac{\sigma_{pp}}{r_{ij}} \right)^{n} - c\sqrt{\rho_i} \right] \tag{3.5}$$

and ρ_i is defined as,

$$\rho_i = \sum_{j \neq i}^{N} \left(\frac{\sigma_{pp}}{r_{ij}} \right)^{m} \tag{3.6}$$

where r_{ij} is the separation distance between atoms, c is a dimensionless parameter, ϵ_{pp} is the energy parameter, σ_{pp} is the lattice constant, and m and n are positive integers with $n > m$. The three parameters c, ϵ_{pp} and σ_{pp} are calculated from the equilibrium lattice parameters and the lattice energy of the fcc lattice [61]. Repulsion between atomic nuclei is represented by the first term in Eq. 3.5, while bonding energy between nuclei is approximated by the second term, which is a result of the surrounding electrons. Sutton and Chen decided to represent the electron density locally for atoms rather than explicitly including it in the potential function [59].

In this study, two sets of parameters of the Q-SC type potentials have been considered. Afterward, a python package was used, atsim.potentials, [62] to form a tabulated potential file using these parameters mentioned in the literature. The following table (Table. **??**) contains the parameters used to conduct this research, taken from two separate articles.

Table 3.1: Two sets of parameters for Q-SC type potential for Pt NW

Functional Parameters	**Sutton-Chen [Param 1]**	**Sutton-Chen [Param 2]**
a (A)	3.92	3.92
ϵ (meV)	19.833	9.7894
c	34.408	71.336
m	8	7
n	10	11

Tabulation of the parameters for interatomic potentials has been done in the atsim.potentials python package using the following input file:

Listing 3.1: Input file example

```
[Tabulation]
target : setfl
#
cutoff_rho : 800
drho : 0.005
#
cutoff : 10.0
dr : 0.001

[EAM-Embed]
Pt : product(as.constant 9.7894e-3, as.sqrt -71.336)

[EAM-Density]
Pt : as.exponential 14129.65859 -7

[Pair]
Pt-Pt : product(as.constant 9.7894e-3,
        as.exponential 3323804.554 -11)
```

Using the first sets of parameters the following result was obtained which can be viewed in the Fig. 3.6. The obtained Young's modulus form the first set of parameters [61] is around 102.3964 GPa which falls short by around 26.07% from the findings by the previous research [57].

Therefore, the second type of parameters were tested to obtain the stress-strain curve (Fig. 3.7) from which the Young's modulus for Platinum is calculated to be 142.039 GPa.

After considering all of the three interaction potentials, the Q-SC type potential (Param 2) was chosen for the interaction between Pt atoms.

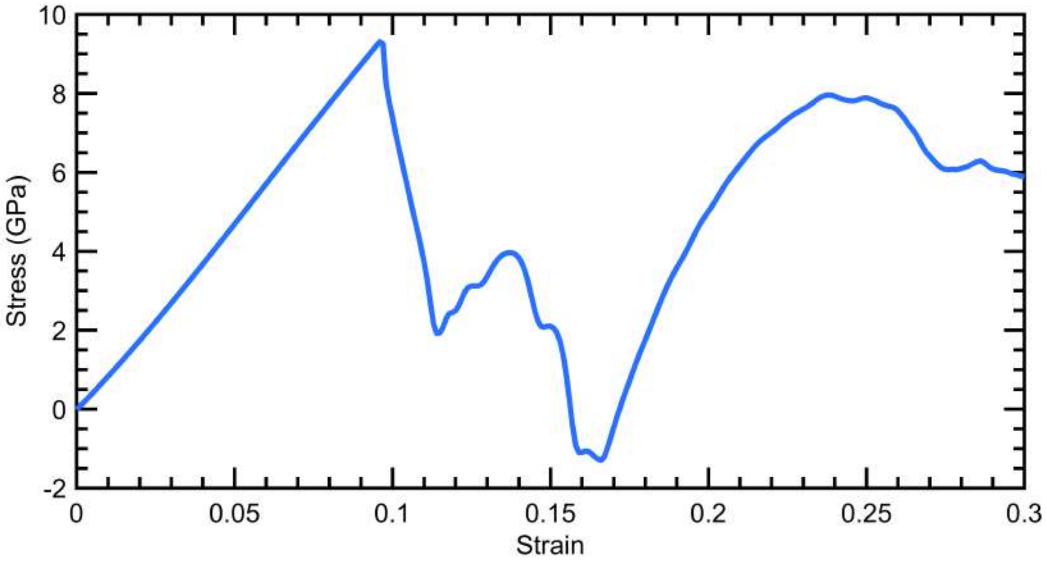

Figure 3.6: Stress-Strain curve of Pt NW using Sutton-Chen [Param 1] interatomic potential

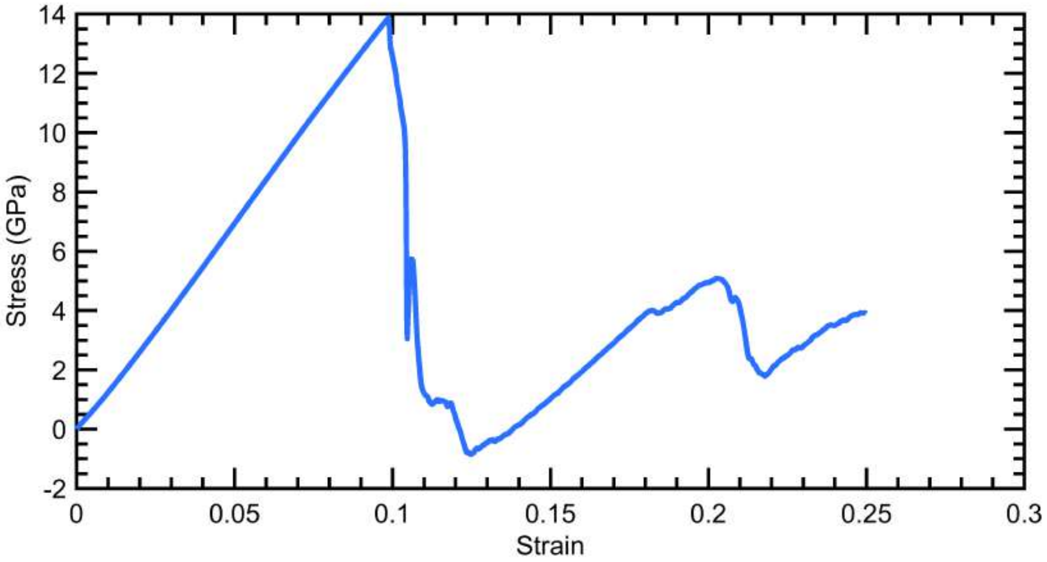

Figure 3.7: Stress-Strain curve of Pt NW using Sutton-Chen [Param 2] interatomic potential

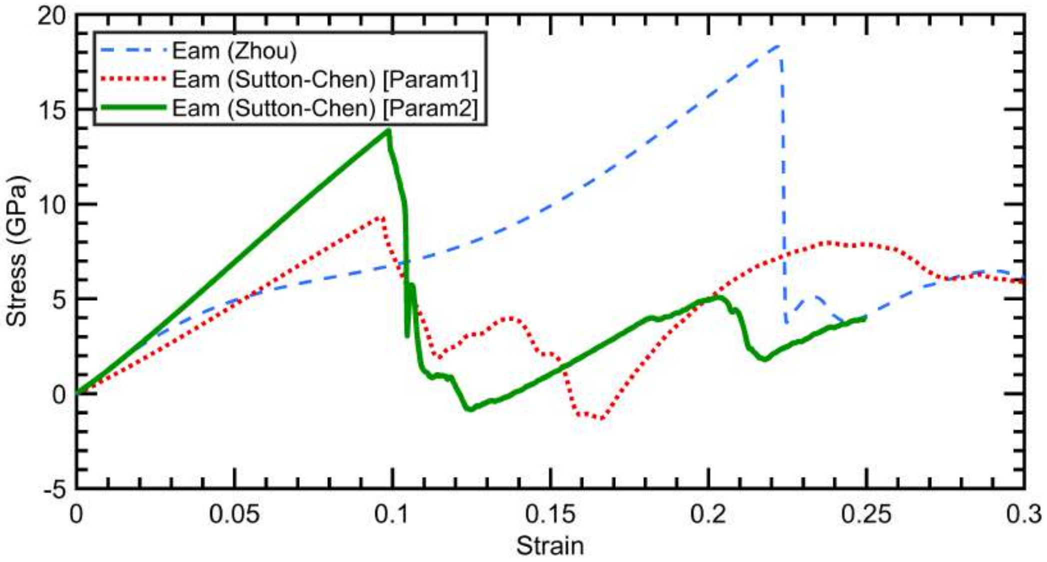

Figure 3.8: Comparison of Stress-Strain curves for three sets of potential files for the interaction between Pt atoms.

3.2.2 Interatomic Potential for Graphene (Fiber)

Covalent substances include silicon and silicon dioxide, carbon-based substances (graphite, diamond, and diamond-like carbon), organic substances, and numerous oxides. Typically, covalent bonds are formed by the valence electrons of two atoms, which are localized between the atoms [63]. A covalent bond has two distinguishing characteristics: it is extremely strong (binding energy ranges from 1 to 5 eV) and it is distinctly directional. One modeling approach that represents these qualities is to explicitly define the bond based on configurational positions of atoms such that the potential is dictated by bond lengths (stretching) and bond angles (bending), and sometimes dihedral angles (torsion) [4].

3.2.2.1 Stillinger-Weber Potential

This spatially constrained accounting of many-body interactions eliminates the contributions from the second, third, or fourth neighbors in real solids, as the SW potential defines the total energy of an atomic system as a sum over the nearest neighbor interactions alone [52]. By considering bonds in terms of their length, angle, and torsional twist, we may not only better understand the atomic interaction but also make it easier to stabilize the material's structure. Many covalent materials have been studied using the SW formulation of solids, which successfully represents the many-body physics of mechanical deformation using a simple set of two-body and three-body interactions [64].

A MD simulation of tensile test on a Graphene sheet has been conducted in the armchair direction to validate if this potential can be used. Fig. 3.9 shows the typical stress-strain behavior of a Graphene nanosheet which align well with previous studies [65].

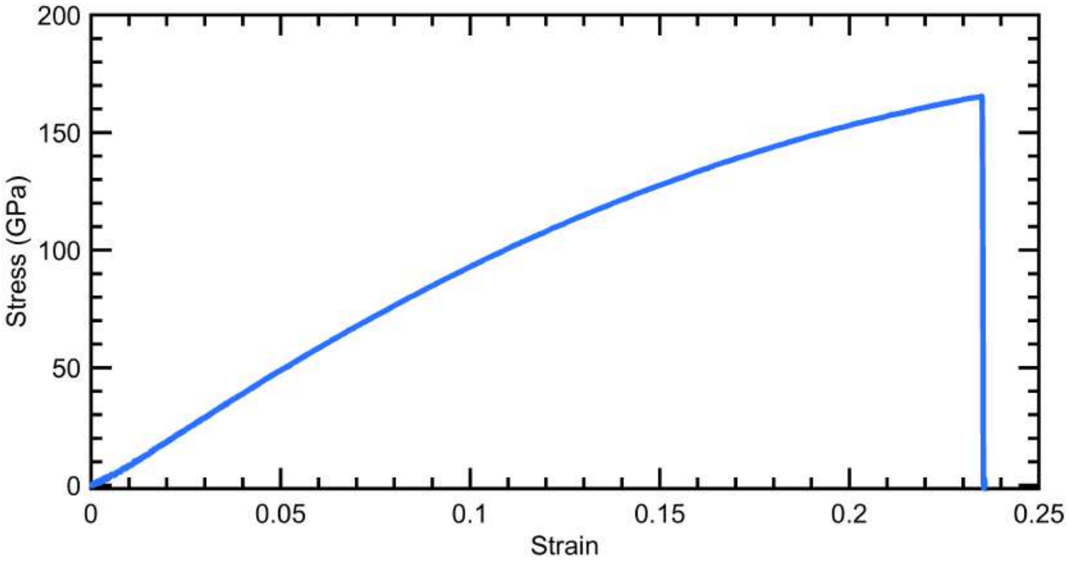

Figure 3.9: Stress-Strain curve of Graphene Nanosheet using SW potential

An investigation has also been conducted on how the failure of Gr NS material is occurred due to this potential. Initially the failure started with the stretching of bond length in the direction of loading. Eventually this leads towards the failure of the Gr NS. As can be seen from the Fig. 3.10, Gr NS failed abruptly like a brittle material. This glass-like brittle fracture has also been observed in the experimental works [66–68].

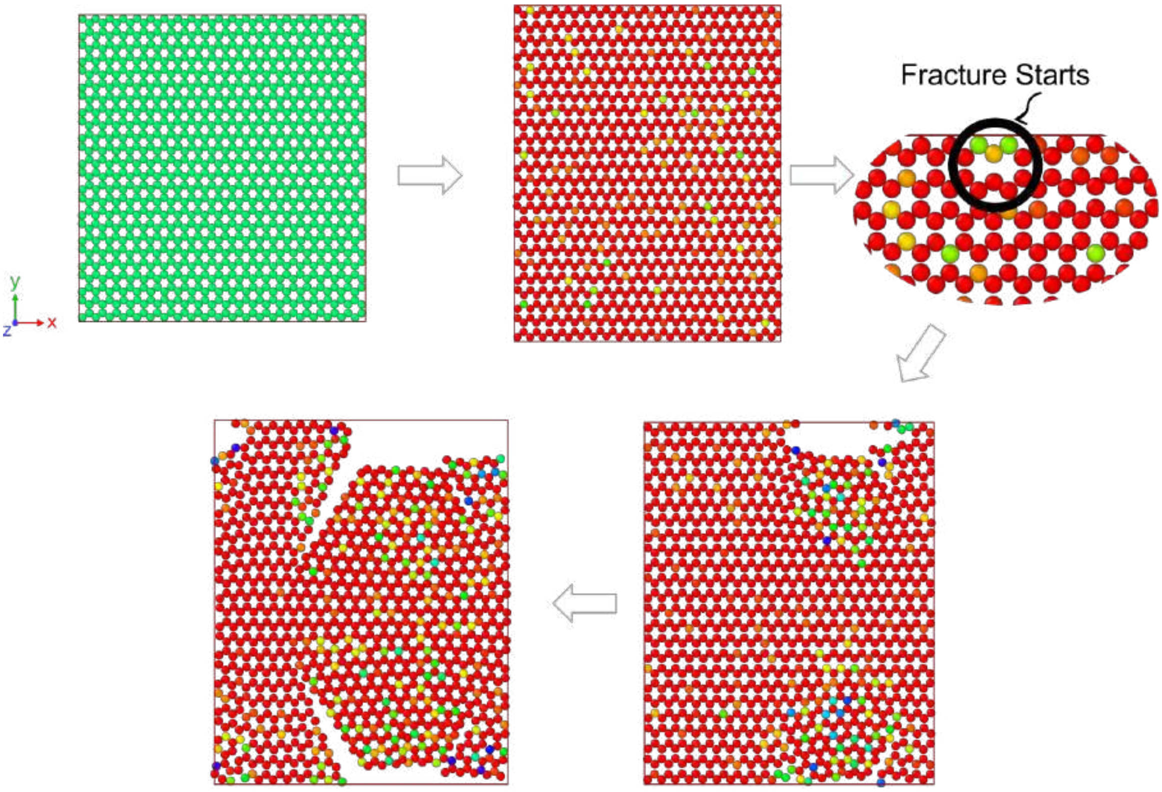

Figure 3.10: Evolution of failure of Gr NS with the increment in strain during tensile test

Table 3.2: Parameters for Tersoff potential and Modified Tersoff potential

Parameters	**Tersoff Potential**	**Modified Tersoff Potential**
$costheta_o$	-0.57058	-0.930
B	346.74	430.00
R	1.95	2.1
D	0.15	0.0

3.2.2.2 Tersoff Potential

This SW approach has a disadvantage due to the fact that there is only one equilibrium configuration, therefore it cannot capture alternative stable structures. Bond-order potentials were developed to alleviate this constraint by providing a bond-order parameter to measure the strength of different bonds, allowing stable states associated with different bonds to be described simultaneously by a single potential. However, because they evaluate additional factors, bond-order potentials are computationally demanding and frequently require parallel implementations [4].

This potential for mimicking the primary bond activity between atoms in inorganic materials was proposed by Tersoff in 1989 [69]. Initially, it was only relevant to silicon, but it was later modified to include carbon [70, 71]. The tersoff potential modifies the bond strengths according to the number of neighbors. The cutoff distance is 2.1 Å, which makes the potential fast in calculations with few atoms, but beyond 2.1 Å no interaction is computed [72].

Lindsay and Broido [73] have enhanced the original Tersoff potential by refining parameters to produce a better fit to structural data, thermal conductivity, and in-plane phonon dispersion. Tersoff potential with optimized parameters is known as the optimized Tersoff potential, and its optimized parameters are listed in Table 3.2

Using these both sets of potential files, (a) Tersoff Potential and (b) Modified-Tersoff Potential, same tensile MD simulation has been conducted on Gr NS. From the Fig. 3.11 and Fig. 3.12 the stress-strain behavior can be found for both of the potentials. The Tersoff potential shows a poor response whereas modified-Tersoff potential depicts a proper trend expected from the simulation.

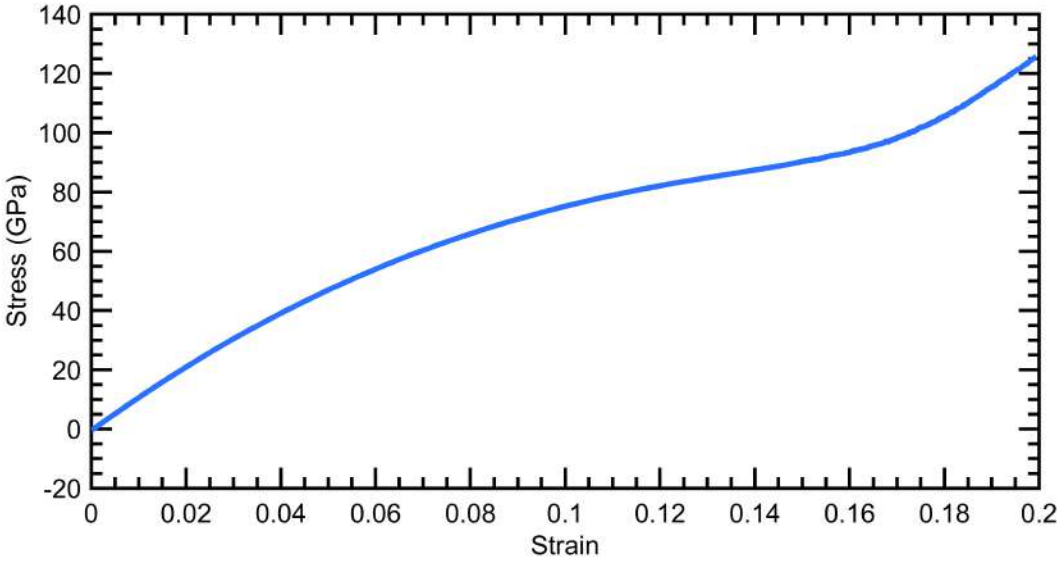

Figure 3.11: Stress-Strain behavior of Gr NS using Tersoff potential

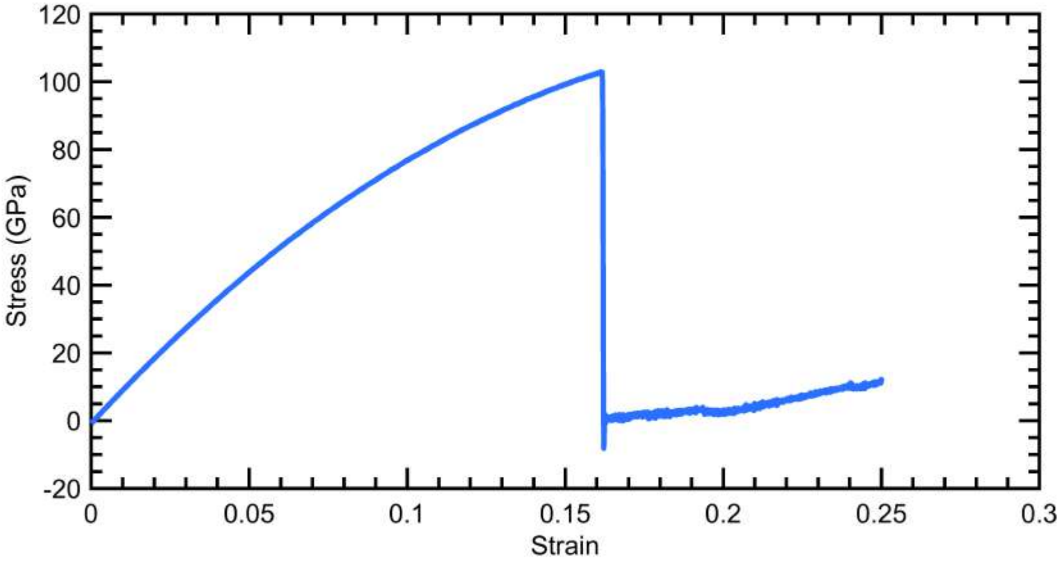

Figure 3.12: Stress-Strain behavior of Gr NS using modified - Tersoff potential

3.2.2.3 Airebo Potential

REBO potential (also known as Tersoff-Brenner potential) may be regarded superior to Tersoff potential [69, 74]. This potential was initially designed to replicate the chemical vapor deposition of diamond [74] and was later upgraded to provide a more precise representation of the energetic, elastic, and vibrational properties of solid carbon and tiny hydrocarbons; it is known as ”2nd generation REBO potential” [75] .

Even though REBO potential is effective at representing intermolecular interactions in carbon and hydrogen materials [74], it is not suitable for all hydrocarbon systems due to its inability to explicitly capture non-bonded and torsional interactions. After correcting these deficiencies of REBO potential, AIREBO potential [76] was created as an expansion of REBO potential. Three subcomponents comprise AIREBO: REBO, Lennard-Jones, and torsional potentials. The mathematical statement provides the total energy of the atomic system:

$$E^{AIREBO} = \frac{1}{2}\sum_{i}\sum_{j\neq i}\left[E_{ij}^{REBO} + E_{ij}^{LJ} + \sum_{k\neq i,j}\sum_{l\neq i,j,k} E_{kijl}^{tors}\right] \tag{3.7}$$

A MD simulation for Gr NS using AIREBO potential has been conducted here. This finding is well matched with previous studies [65].

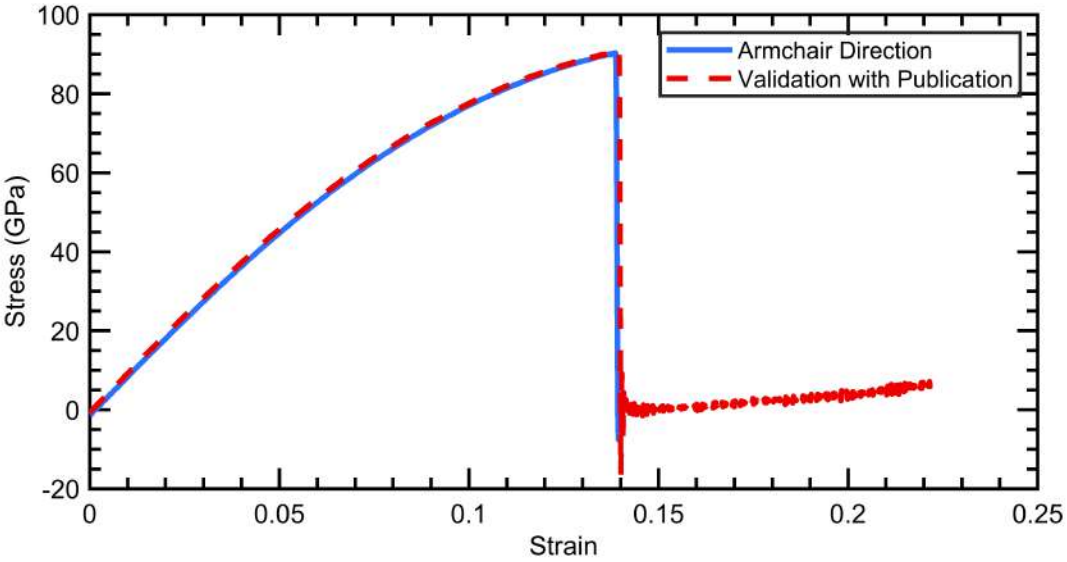

Figure 3.13: Validation of Stress-Strain curve using AIREBO potential for Gr NS

Simulation using AIREBO potential has also been done on the both zigzag and armchair direction, refer to Fig. 3.14.

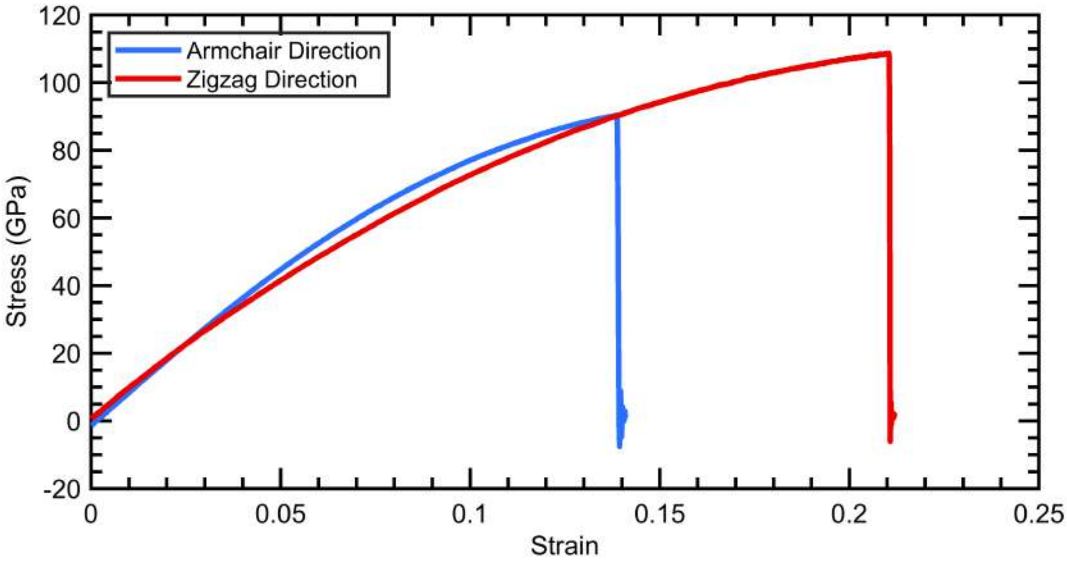

Figure 3.14: Stress-strain curve for Gr NS [Zigzag and Armchair direction]

Also, a simulation has been done using AIREBO-m potential which shows (Fig. 3.15) very poor simulated result.

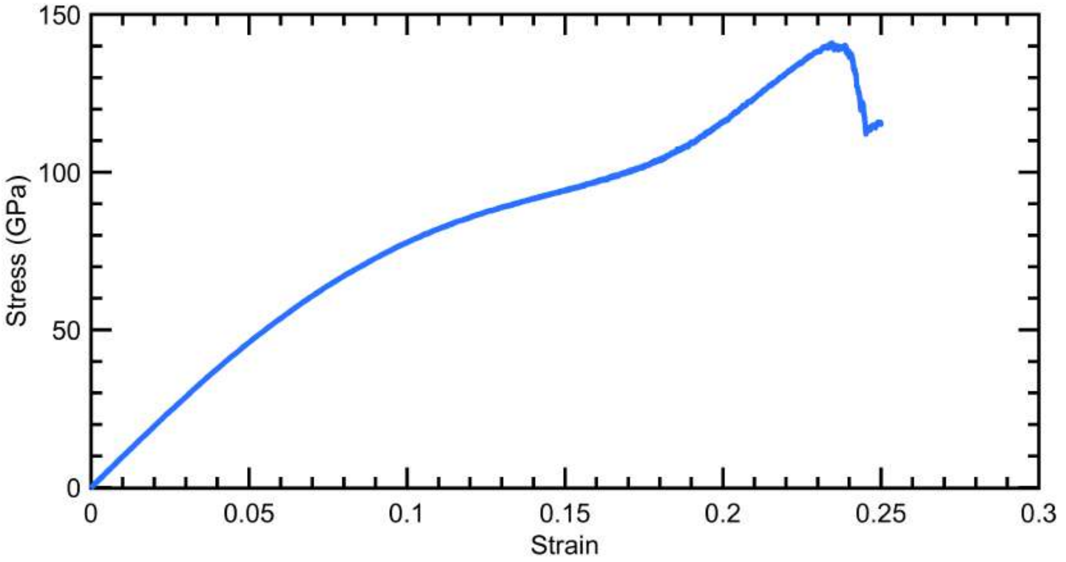

Figure 3.15: Stress-Strain curve of Gr NS using AIREBO-m potential

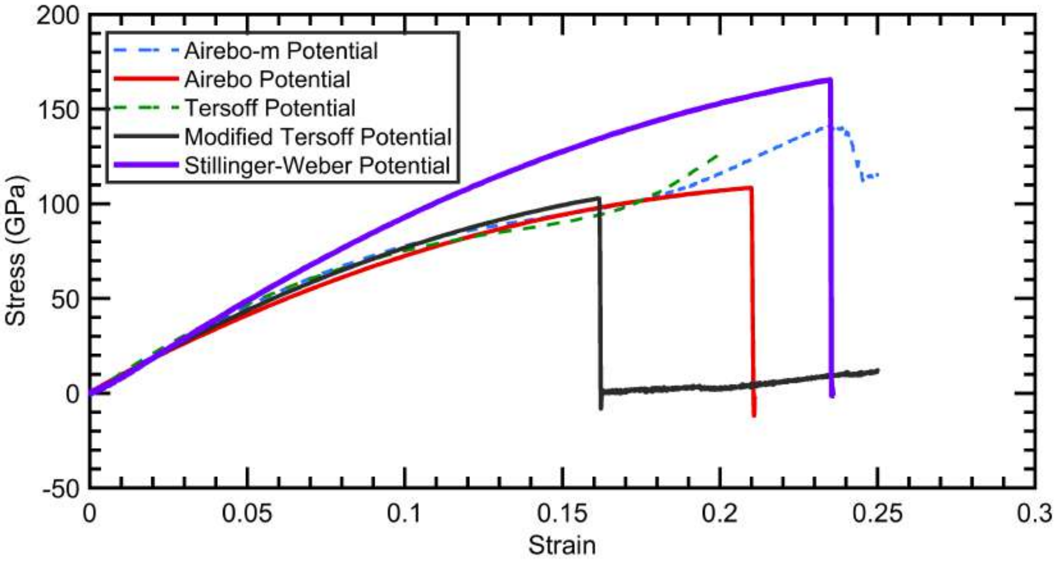

Figure 3.16: Combined Stress-Strain curve of Gr NS for different potentials used in this study

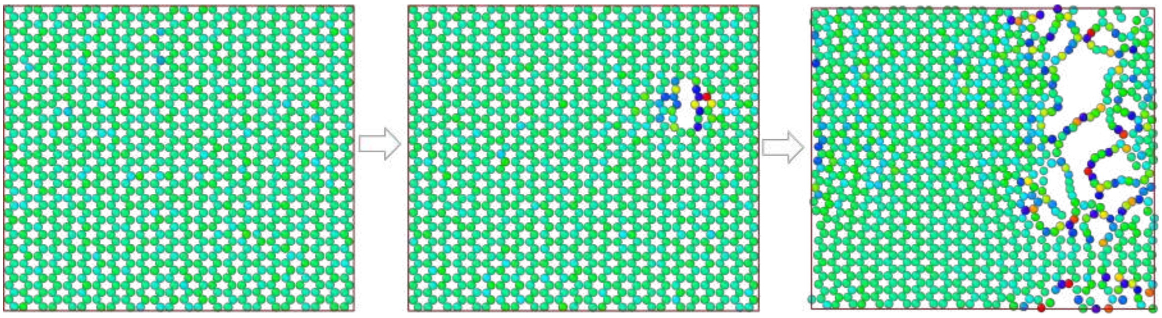

Figure 3.17: Evolution of failure using AIREBO potential on a Gr NS

3.2.2.4 Selection of Potential for Graphene

The AIREBO potential [76], which has proven highly popular for analyzing the mechanical properties of graphene, reveals youngs modulus of 828 GPa along the armchair (AC) direction and 995 GPa along the zigzag (ZZ) direction [77]. This indicates that graphene is an elastically anisotropic media, which is in contrast with the results from first principles or the experimental observations [77]. Bond-order potentials like the Tersoff [69], REBO, and AIREBO-M potentials demonstrate unphysical stress-strain behavior for graphene (and CNT) in their original form [74]. Existing empirical potentials, such as the AIREBO and Tersoff potentials, exhibit chainlike atomic couplings across the failure surfaces (Fig. 3.17), which contrasts with the glass-like brittle fracture [78–81] that was actually observed [66–68]. Among all the potentials for graphene fiber, the SW potential has been selected for the purposes of this current research.

3.2.3 Potential for interaction between Pt metal matrix and Graphene fiber

The most challenging aspect of this simulation work is identifying a possible function that adequately describes the interaction between platinum and carbon(Gr). There are very few published potential parameters for this type of metal-nonmetal interaction. One proposed option is to employ quantum mechanical calculations to directly estimate the potential energy function between a platinum and a carbon(Gr) atom. Alternatively, the Q-SC potential can be used to derive a Lennard-Jones potential. Using the Lorentz-Berthelot mixing rule, the calculated potential parameters ϵ_{pt}^{eff} and σ_{pt}^{eff} can subsequently be utilized to estimate the Pt-Gr parameters. The value of the potential parameters for the Pt-Gr interaction, ϵ_{pt}^{eff} and σ_{pt}^{eff}, is then found to be 2.905 A and 256 K, respectively [82]. Use of these values yield a stress-strain curve of very poor result as shown in the Fig. 3.18.

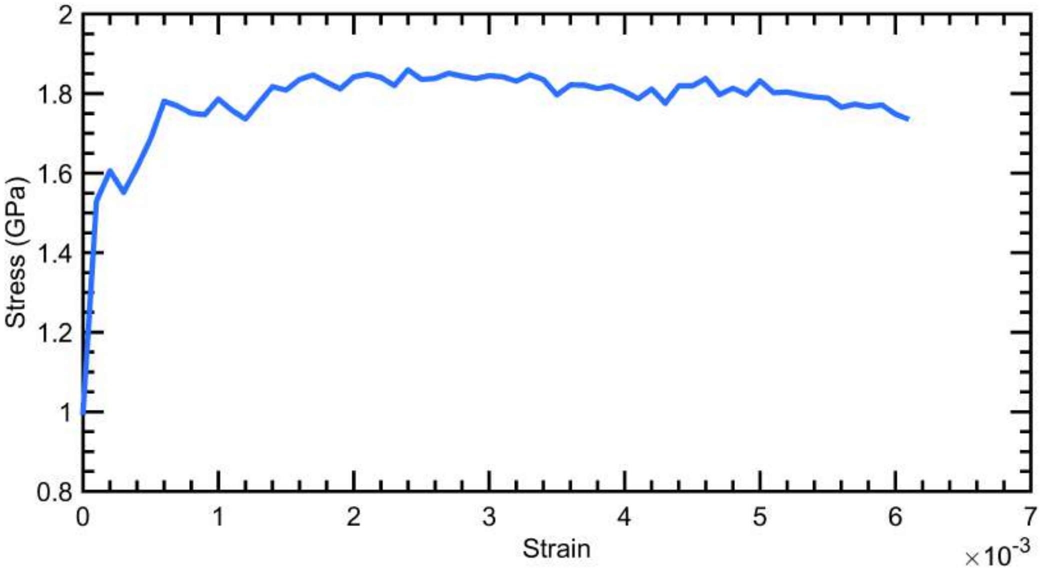

Figure 3.18: Stress-Strain curve of Pt-Gr NC using lj potential

Another option is to combine potentials of various types that were individually optimized to describe the energetics and mechanical characteristics of platinum and covalently bonded carbon [83]. For this study, One may combine the Q-SC potential for Pt-Pt interaction, the Stillinger-Weber potential for interplay between carbon atoms in Gr layers, and the lj or Morse potential for Pt-Gr interaction. It can be emphasized how problematic it is generally to add potentials that are structurally different. The approach may, however, be practical in the current situation because the system's components—metal and graphene—maintain their structural integrity and the van der Waals type interaction between them can be viewed as an addition to their internal—metallic and covalent—interactions [83]. In contrast to

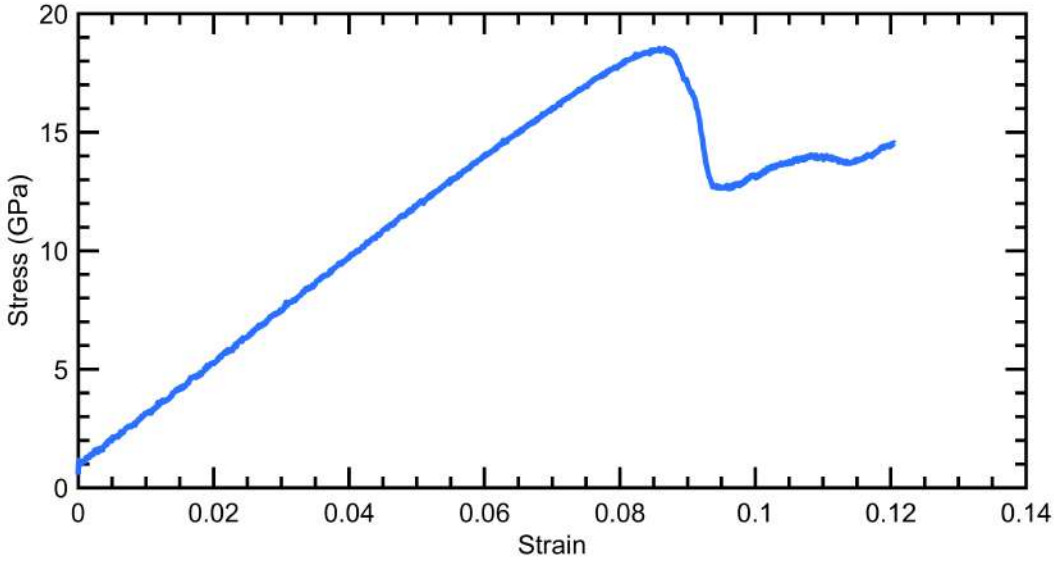

Figure 3.19: Stress-Strain curve of Single Layered Pt-Gr NC using Q-SC+SW+morse hybrid potential

what was found in earlier research, it was found that the LJ potential has obvious flaws since it is overly stiff and hence considerably overestimates the forces operating across the Pt-Gr contact [83].

In this study, a Morse potential is considered of the following form:

$E_m = D(exp[-2\alpha(r - r_0)] - 2exp[-\alpha(r - r_o)])$

where r is Pt–Gr distance, r_0 indicates the equilibrium bond distance, D is the well depth, and α dictates the potential stiffness(smaller the attractive/repulsive forces means smaller α). The parameters for the Pt–Gr Morse potential, taken from previous research [83], are D = 0.0071 eV, r_0 = 4.18 Å, and α = 1.05 $\mathring{A}^{-}1$.

Using these parameters, and combining Q-SC, SW with it for a single layered Pt-Gr NC system a stress-strain curve from a MD simulation is obtained which found out to be better fit in the current study.

3.3 Boundary conditions

In compared to actual systems, the sizes of simulated systems are often quite tiny, and numerous variables stemming from the limited size may influence the results. Utilizing periodic boundary conditions (PBC) to replicate an infinite system size with a limited system size is one method for mitigating these impacts. Atoms in system boundaries can be handled in a number of ways: with no boundary conditions, they will pass through the boundary; with reflecting boundary conditions, they will be redirected by changing the sign of their velocity; and with periodic boundary conditions, they will reappear on the opposite side of the simulation box after crossing the boundary. The boundary criteria may permit the insertion of more accurate points [1]. Fig. 3.20 depicts PBC for a two-dimensional (2D) system.

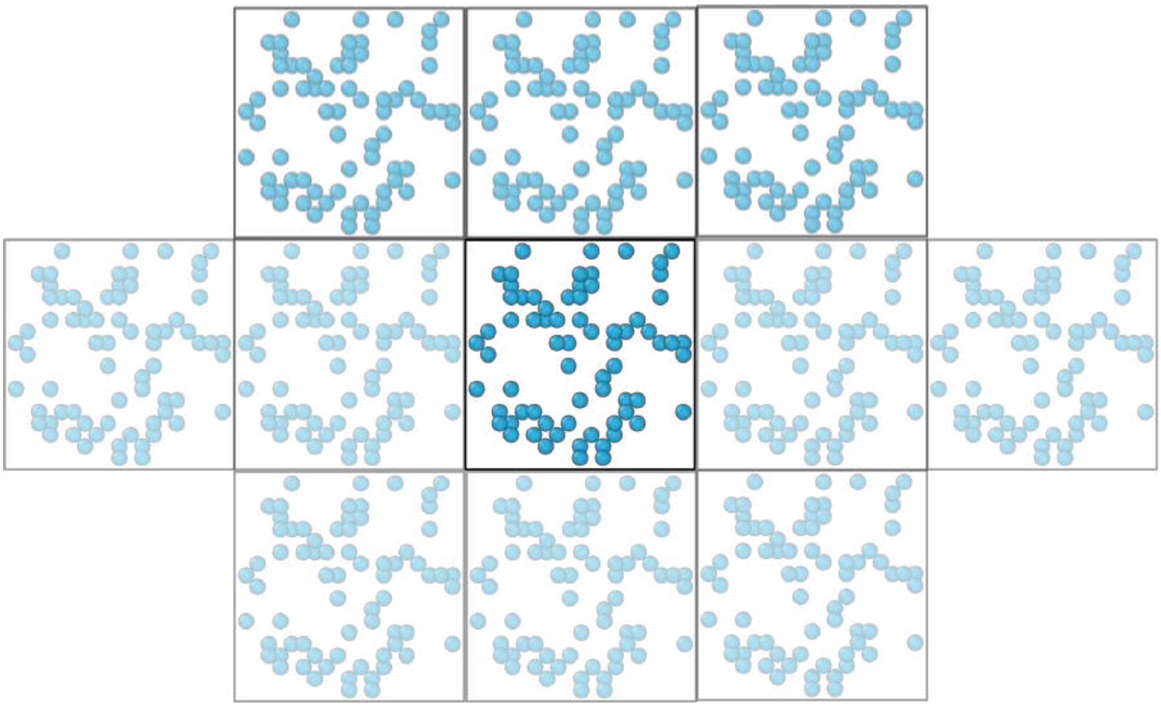

Figure 3.20: PBC for a 2D case

When adopting PBCs, the wraparound effect may be accounted for by utilizing the minimum image convention for computing position-dependent values [1] [84]. In Fig. 3.21, a replica of the blue atom is situated closer to the red atom than the blue atom itself, exhibiting a minimum image convention for a 2D system.

3.4 Ensembles

The macroscopic state of a system is defined by macroscopic properties like temperature (T), pressure (P), and volume (V). Numerous thermodynamic parameters may be calculated using equations of state and other fundamental thermodynamic equations. In contrast, the microstate allows us to determine the positions and velocities of all particles in the system. To relate the macroscopic characteristics of a system to the microscopic characteristics of its component particles, the concept of an ensemble must be formulated. These microstates constitute a macrostate or ”ensemble” [85]. That is to say, a single macrostate may reflect several microstates. Various ensembles exist, each with a specified set of constants for char-

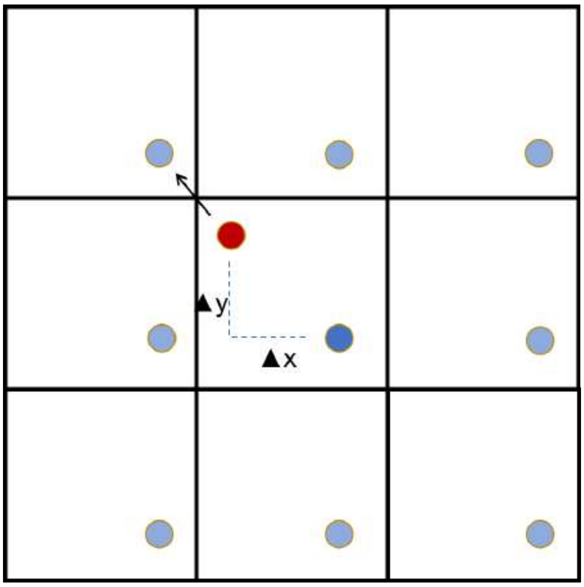

Figure 3.21: The minimal minimum in terms of image convention for a 2D system. The arrow indicates the route between the red and blue atoms that is the shortest. [1]

acteristics like temperature (T), pressure (P), volume (V), number of particles (N), energy (E), or chemical potential. In this study, all MD simulations were performed using either the NVT ensemble (where N, V, and T were all maintained constant) or the NPT ensemble (where N, P, and T are all held constant). Since these ensembles accurately represent experimental conditions, they are often used in MD simulations. For some situations, NVE ensemble has also been used.

3.5 Measurement of Physical Quantities

3.5.1 Energy

In MD simulations kinetic energy is denoted as

$$E_k = \frac{1}{2}\sum_{i=1}^{N} m_i v_i^2 \tag{3.8}$$

Potential energy of the system is force field, described in potential file, dependent and denoted by -

$$E_p = \sum_{i=1}^{N}\sum_{j>i}^{N} U(r_i, r_j) \tag{3.9}$$

3.5.2 Pressure

There are several techniques for calculating the system's pressure. Typically, the pressure for an N-body system with volume V and particle density ρ = N/V is derived using the virial equation.

$$P = \rho k_B T + \frac{1}{dV} < \sum_{j>i} F_{ij}.r_{ij} > \tag{3.10}$$

here d is the dimension number, force exerted on i from j is denoted by F_{ij}. For this particular expression, we assume canonical ensemble. For other micro-canonical ensemble the equation is not the same.

3.5.3 Temperature

According to thermodynamics, thermal energy can be written mathematically as

$$E_k = \frac{f}{2} N k_b T \tag{3.11}$$

Assuming that particles are points, we only evaluate their translational degrees of freedom and disregard their rotational degrees. Since Newtonian motion is assumed, the total kinetic energy of the system may be expressed as equation 3.8.

By equating these, instantaneous temperature can be found

$$T = \frac{< m_i v_i^2 >}{f k_b} \tag{3.12}$$

Thus, we may estimate the instantaneous temperature using the atomic velocities. Consequently, it is common practice to take an average over a period of time to smooth out the value's fluctuations around the true number. In many circumstances it is desirable to adjust the temperature of the system, e.g. when utilizing the canonical ensemble (NVT). Methods for doing this are termed thermostats.

3.6 Thermostats

Changing the virtual environment's temperature is a typical simulation activity. This is done by modifying the velocity in the equation (3.12). The instruments used for this purpose are thermostats. There are several types of thermostats, each with its own benefits and drawbacks, for example, Berendsen and Andersen thermostats. These thermostats are an excellent option for systems that need to be returned to equilibrium. However, direct velocity rescaling has the potential to generate simulation inconsistencies [1,86].

3.6.1 Nose-Hoover Thermostat

The most common thermostat model is the Nosé-Hoover. Consistent dynamics and a temperature that resembles the real world are the outcomes. This thermostat differs from its Berendsen and Andersen equivalents in that it does not account for atomic velocity variations. However, it modifies the Hamiltonian of the system by adding a fictitious frictional force. Changing the equation for motion to

$$F_i = -\nabla U_i(r^N) - \xi m v_i \tag{3.13}$$

Here, the force, F_i works on the masses, Potential energy is U, r^N denotes position of the masses, strength of the thermostat is regulated through a dynamic variable ξ, m and v_i are mass and velocity of the particles respectively. By preventing the re-scaling of particle velocities, this function of the thermostat guarantees precise dynamics and stable temperature settings.

3.7 Integration Timestep

The timestep utilized for numerical integration is of the utmost significance since it influences the accuracy and convergence of MD simulations. With a lower timestep, simulations become more accurate, but at a larger computational expense. When the timestep is raised, additional sampling of the conformational space comes at the expense of simulation instability. Consequently, choosing the appropriate timestep is crucial for obtaining accurate findings and a smooth simulation run. It is vital for numerical integrators to have a timestep that is sufficiently small in proportion to the quickest portion of the motion [87]. For this simulation, I have taken a timestep of 1fs considering a balance between simulation time and computational performance.

3.8 Minimization

Even after the first structures have been generated through experimental studies, certain residues may lack atoms. Therefore, if the missing atoms are added during the creation of the initial structure, energy reduction of the original coordinates is required to avoid any potential steric conflicts between atoms. Prior to using MD simulations, it is often used steepest descents and conjugate gradient approaches in this study.

Chapter 4

Mechanical Properties: Tensile Test

Mechanical property of any material generally indicates its ability to hold up to external loading or how well it can tackle various external loads. A material specific property, Young's modulus, is evidently indicator of the mechanical strength of a material. In this chapter, a discussion on the evaluation of mechanical property of selected Platinum-Graphene nanocomposite through tensile testing using MD simulation will be introduced.

4.1 Theoretical Background

To evaluate a material's mechanical properties, the most common test is the tensile test. The results in a tensile test are used for (a) application based material selection (b) ensuring quality (c) predicting material behavior under loading apart from tensile load [88]. In general, this test consists of a strip or cylinder of the selected material of length, L and cross-sectional area, A which is fixed at one end and is subjected to a load, P on the other end. With the increment of the load, the axial deflection δ at the end where load is applied increases, refer to the Fig. 4.1.

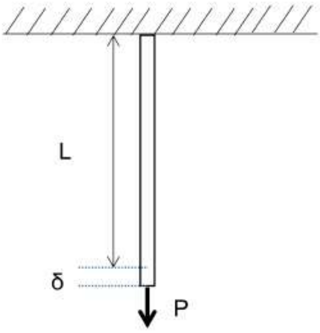

Figure 4.1: Tensile test basic setup

According to Robert Hooke, the load P and deformation δ due to this has a linear relation for sufficiently smaller loads. The relation, named Hooke's law, can be depicted as follows:

$$P = k\delta \tag{4.1}$$

Where k is a constant called stiffness of the material. To make this constant more material specific, after normalizing load by cross sectional area and taking deformation per unit length the equation becomes

$$\sigma = E\epsilon \tag{4.2}$$

Here the constant term, E is called Young's modulus which is one of a material's most significant mechanical characteristics [89].

In general, every material has its internal energy arising from the bond energy at atomic scale. During a tensile test, with the increment of stress, strain increases and so happens the stretching of the bonds. Therefore, stretching experienced by any material specimen due to a small load is controlled through the tightness of the bonds between the atoms. These chemical bonds are governed by the electrostatic attraction between charges of different polarity. A pair of atoms' likelihood of remaining linked in the face of energy perturbations is indicated by their bond energy, which serves as an indicator of the strength of a chemical bond. It can also be interpreted as a measurement of the stability that results from the bonding of two atoms as opposed to their free or unbound states [90]. Generally, the bond energy, and so the modulus of elasticity E, has a relation with the curvature of bond energy function.

4.2 Simulation Methodology: Tensile Test

In this paper, the Molecular Dynamics (MD) simulation of tensile test begins with the material design. A Graphene reinforced metal matrix, Platinum (Pt), has been chosen for the study. The nanocomposites were designed using ATOMSK [48] software package. Firstly, several layers of Pt were created (Fig. 4.2).

Then the system of Pt atoms were merged with single sheet Graphene layer (Fig. 4.3). The nanocomposite system was completed by sandwiching Graphene layer inside Pt layers (Fig. 4.4). By increasing number of Graphene layers, different sets of nanocomposite were designed. For this study, one to five Graphene layered nanaocomposites were designed.
For this investigation, we used LAMMPS [91] for simulating the system. As a boundary condition for the simulation system, we have emplyed P-S-S boundary conditions. Here, the style P indicates that the box is periodic, so that particles can interact across the boundary

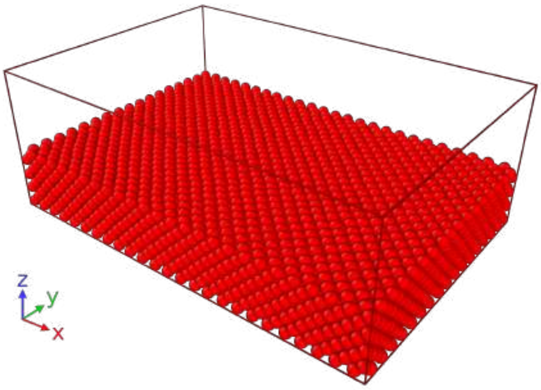

Figure 4.2: Layer of Metal Matrix (Pt)

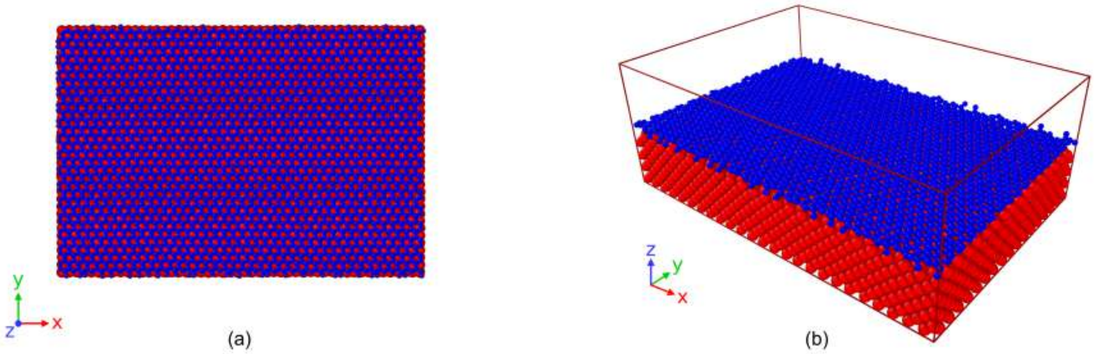

(a)

(b)

Figure 4.3: Graphene layer merged with Pt (a) Top view (b) Perspective view

and enter and depart the box at either end. The shrink-wrapped style S indicates that the box is non-periodic, meaning particles do not interact across the boundary or travel from one side to the other. For style S, the position of the face is set to surround the atoms in that dimension regardless of how far they move (shrinkwrapping) [91]. Note that when the difference between the current box dimensions and the shrink-wrap box size is substantial, executing in parallel can result in lost atoms at the beginning of a run. This is owing to the fact that the big shift in the (global) box dimensions also caused considerable changes in the subdomain sizes. Atoms will be lost if these changes are further away than the communication cutoff.

The whole system was relaxed using conjugate gradient method, initially. Every timestep

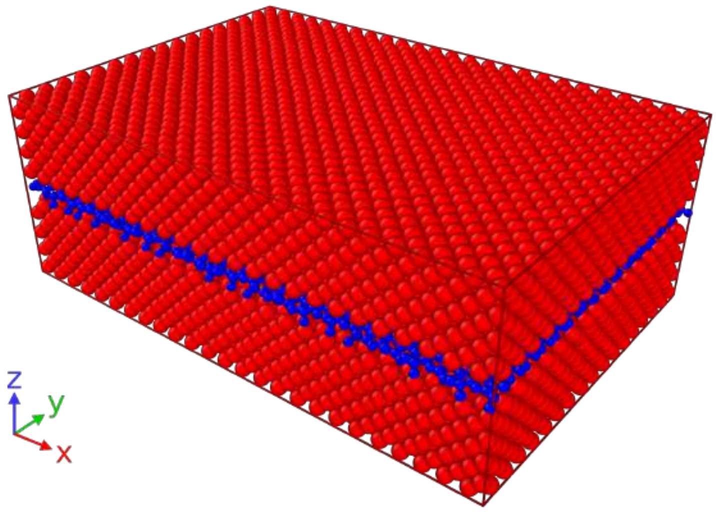

Figure 4.4: Single Graphene layered Pt-Graphene Nanocomposite

for the simulation was taken to be 1 fs which comply with better computing resource management. After the relaxation, equilibration of the system was done at 300K temperature using NVT (Number of Molecules, Volume, Temperature) ensemble for 1 ns. The nanocomposite was equilibrated so that the simulated material worked as real life material. When the nanocomposite had stabilized, a continuous strain rate was applied along its x axis on both sides. The strain rate for the simulation was taken to be $10^9\ \frac{1}{s}$ which is a fair choice in terms of balance between computing time and output result's usability.

Several methods, such as the virial stress method and the energy method for the derivation of Young's modulus, have been developed to extract the mechanical characteristics of NWs (such as Young's modulus, Poisson's ratio, and elastic constants) from MD simulation results as proposed by Diao, et al [92]. Using linear regression, the conventional method, Young's modulus will be evaluated directly from the stress-strain curve in this study. The stress at which plastic deformation first occurs, i.e., when partial dislocations are first emitted, is known as the yield strength in continuum mechanics and atomic configurations during simulation. In this paper, we make use of the engineering strain, which is hereby defined as:

$$\epsilon = \frac{(L - L_0)}{L_0} \tag{4.3}$$

Here, L is the instantaneous length and L_0 is the initial length of the NW after the energy minimization.

4.3 Parametric Study

For this study, the desired model of nanocomposite (NC) will be subjected to a constant strain rate of $10^9 \ \frac{1}{s}$ for a long enough time, almost 20-25 ns, for each simulation. A dump file containing strain and its corresponding stress, obtained by simulation [91], will be used for our analysis. First of all, a plot of stress, σ, against strain, ϵ will be created as shown in the Fig. 4.5.

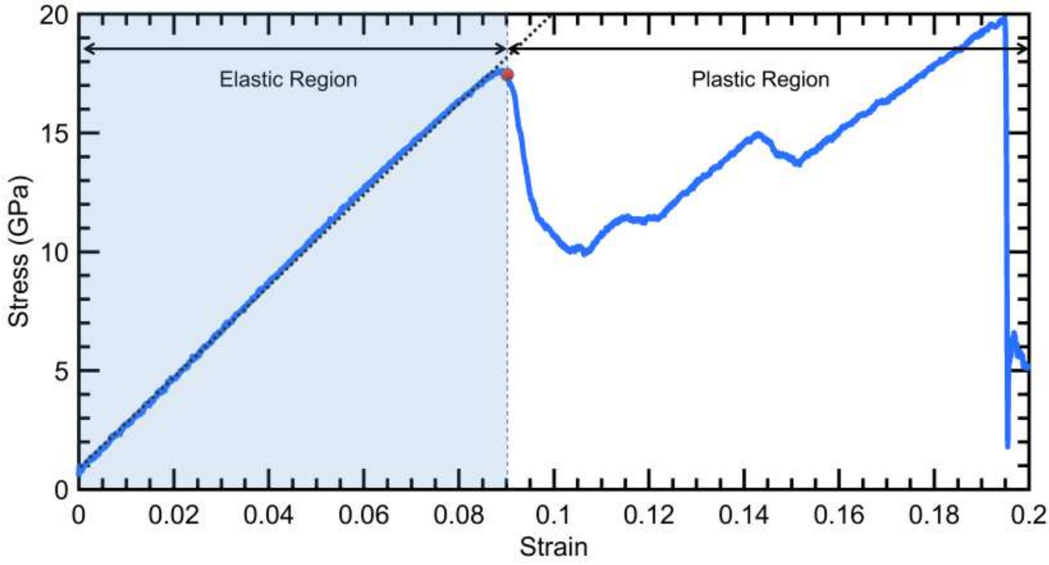

Figure 4.5: Stress-Strain curve for single layered Pt-Graphene NC

Many materials generally follow Hooke's law in the early (low strain) portion of the curve, leading stress to be proportional to strain with the modulus of elasticity or Young's modulus, written E, as the constant of proportionality:

$$\sigma = E\epsilon$$

From the stress-strain curve the modulus of elasticity is found by calculating the slope of the curve upto the proportional limit. From the curve (Fig. 4.5) it can be seen that at a strain of 0.09 the curve starts to descend. This point is regarded as yield point and the maximum stress, yield stress, is calculated at this point. After this point, the region is regarded as plastic region where nonlinear behavior of the curve is evident. This nonlinearity is typically linked to ”plastic” flow caused by stress in the material. Atoms are being relocated to new equilibrium places while the material is experiencing this rearrangement of its internal molecular or microscopic structure. This plasticity necessitates a mechanism for molecular mobility, which in crystalline materials can result from dislocation motion [93].

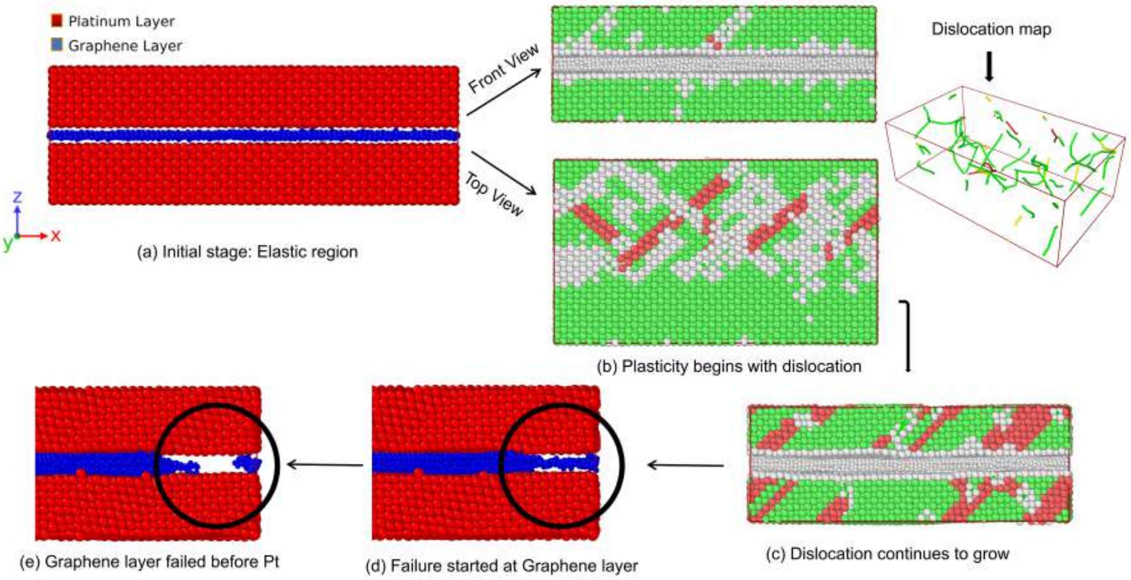

Figure 4.6: Evolution of single layer Pt-Gr NC under uniaxial tension

Overall, in line with findings from earlier studies [92], the nucleation and propagation of partial dislocations dominate the tensile deformation of the NC (i.e., a slip-dominated deformation process).

4.3.1 Initial stress

Prior studies have indicated the occurrence of an initial stress or strain in NCs, as seen in Fig. 4.5. Surface tension is thought to be the primary instigator of this kind of early stress. For NCs without periodic boundary conditions, it is clear that following energy minimization or relaxing, the NC would be free of stress (getting an equilibrium configuration). However, a NC with P-S-S BCs is an exception to this rule. The periodic BC is easily pictured as a sequence of copies or image NCs extending infinitely along the axis from the original NC sample [94]. In particular, the replicas will always interact with the NC's two ends, putting the original NC under a stress that is greater than zero even in the absence of any external force. Diao, et al [95] hypothesized that the initial axial stress σ_{xx} can be estimated by:

$$\sigma_{xx} = \frac{4\tau_0 h}{A} = \frac{4\tau_0}{h} \tag{4.4}$$

where τ_0 = initial surface stress, h = cross-sectional size, and letting the cross-sectional area = h^2.

4.3.2 Improvement in Mechanical Properties

In general, a composite material, for our case a NC, comprised of a matrix material reinforced by a fiber material. Since reinforcement is done, it is expected to have improvement in its mechanical properties than its pristine matrix counterpart [7]. For our case Platinum (Pt) is selected as a metal matrix whereas Graphene is chosen to be the reinforced fiber. Let us consider, a single layered Pt-Graphene NC contained with a volume fraction V_f of Graphene fiber which is subjected to stress, σ in the zigzag direction. For a region of unit dimension, the matrix volume fraction will then be, $V_m = 1 - V_f$ (Refer to Fig. 4.7.)

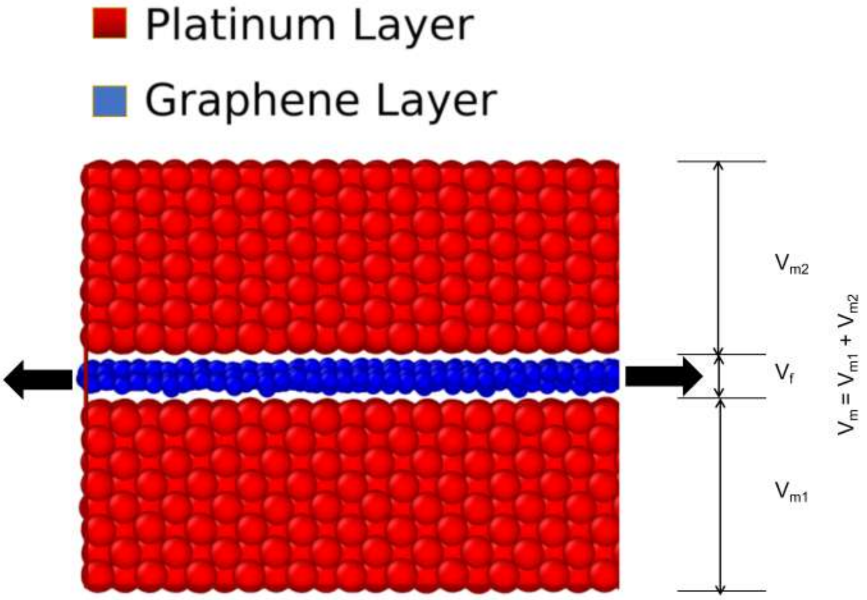

Figure 4.7: Single layered Pt-Graphene NC's volume fractions

Fig. 4.8 indicates that, stress is acting in the zigzag direction of the fiber, Graphene, and both the fiber and matrix are in parallel for supporting the load. The strain should be same in each phase for these parallel connections, which can be written as: $\epsilon = \epsilon_f = \epsilon_m$. Now the overall load on the material must be equal to the sum of the forces acting throughout each phase. Since forces on both fiber and matrix is stress times area (numerically area = volume fraction) we may have

$$\sigma = \sigma_f V_f + \sigma_m V_m$$

So, the overall modulus of elasticity for the NC should be [96]:

$$E = \frac{\sigma}{\epsilon} = E_f V_f + E_m V_m \tag{4.5}$$

It will be checking whether this simulated system comply with Eq. 4.5. Firstly, Young's

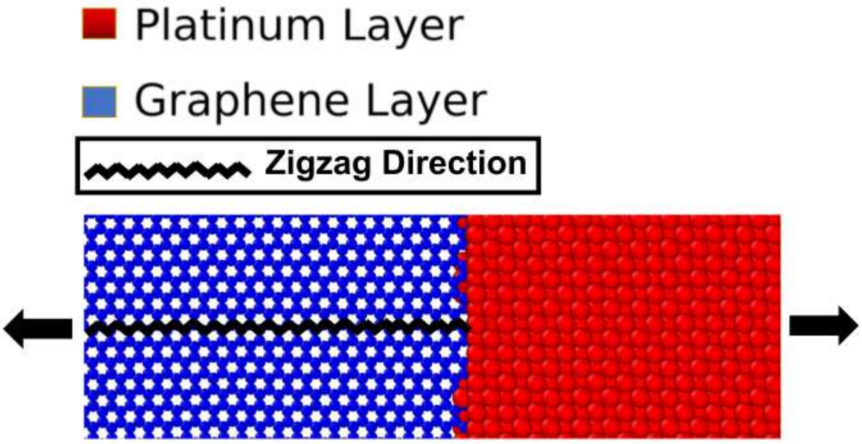

Figure 4.8: Pt-Graphene NC subjected to stress in the zigzag direction

modulus of both Pt and Graphene will be calculated using their corresponding stress-strain curve. Afterwards, inputting these values into Eq. 4.5 will give us an overall modulus of elasticity for our simulated system which will then be compared with simulation result.

The stress-strain curve in Fig. 4.9 is obtained from a MD simulation of a Graphene nanosheet using Stillinger-Weber potential. Calculated Young's modulus is found to be 911 GPa or 0.911 TPa which is well matched with previous research [9]. Also simulated results of a pristine Pt NW as shown in Fig. 4.10) has shown that the Young's modulus of Pt NW for 300K to be 128.98 GPa.

Table 4.1: Validation of Pt-Graphene NC simulated result

Young's modulus Pristine Pt	**Young's modulus** Graphene sheet	**Volume fraction** Platinum	**Volume fraction** Graphene
E_{pt}	E_{gr}	V_m	V_f
128.98 GPa	0.911 TPa	0.905	0.095

If we input the data from Table 4.1 into the Eq. 4.5, then we get theoretical value for single Graphene layered Pt-Gr NC as, E_{th} = 203.2756 GPa. Now, the stress-strain curve through MD simulation has given the value for Young's modulus of a single layered NC = 199.3007 GPa. The value gained from MD simulation agrees pretty well with the Eq. 4.5.

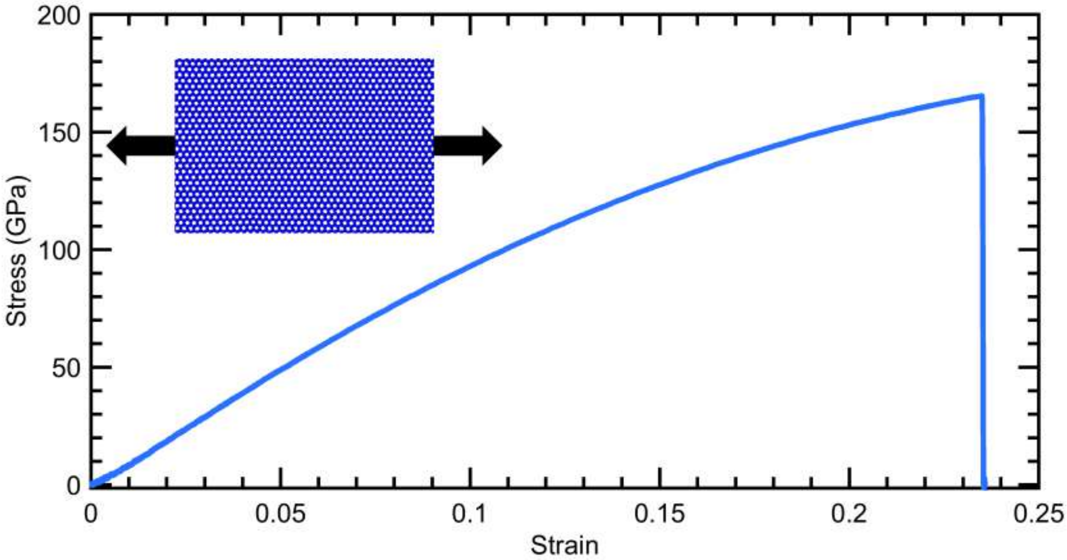

Figure 4.9: Stress-Strain curve for Graphene Nanosheet

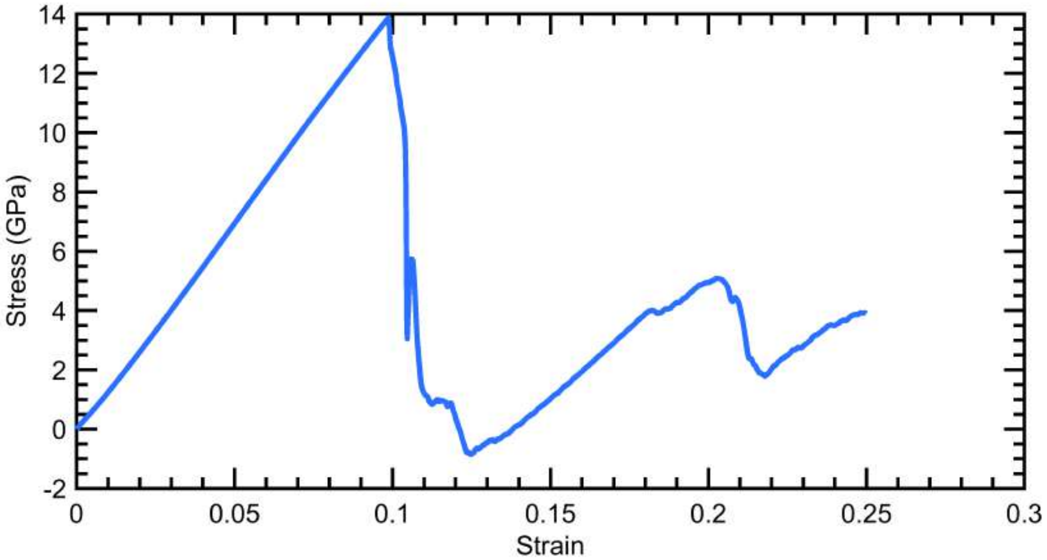

Figure 4.10: Stress-Strain diagram for Pristine Pt NW

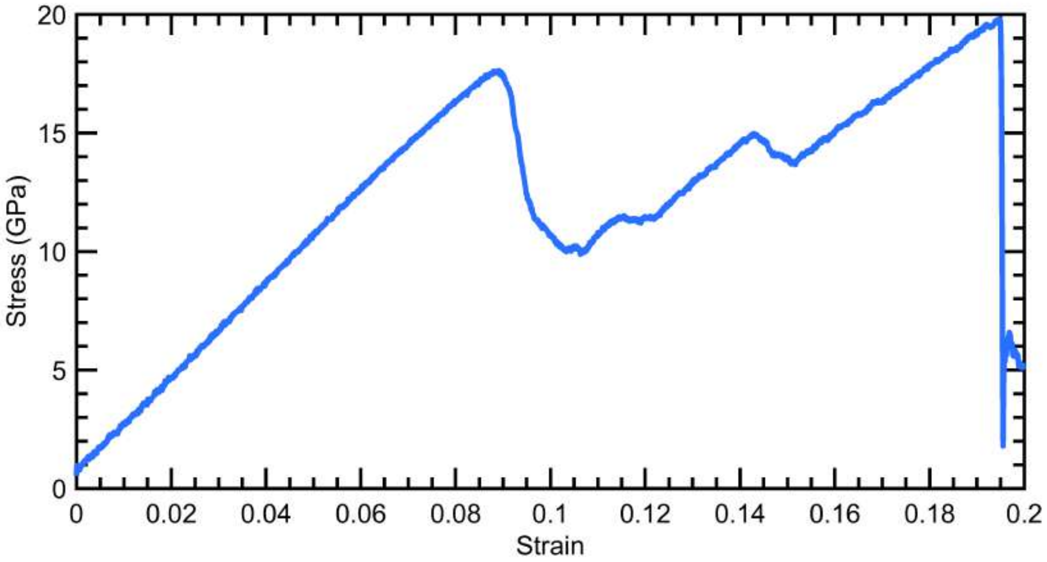

Figure 4.11: Stress-Strain curve for single Graphene layered Pt-Graphene NC

4.3.3 Mechanical properties of NC for different number of Graphene (fiber) layers

As mentioned in the previous section, the nanocomposite chosen for the study has shown a profound impact on the mechanical properties validated by tensile testing. According to Eq. (4.5), with the increment of the volume fraction of the Graphene layer, and Graphene having superior mechanical properties, the Young's modulus of the NC should be increased. Therefore, a simulation on the NC with different Graphene layers, ranging from one to five, is done in this study.

Fig. 4.12 - 4.15 show the stress-strain curves of Pt-Graphene NC for different layers of Graphene sheet. The curves show that the behavior of the NC in the plastic region changes when graphene layers are included, showing a strengthening effect with the addition of graphene layers.

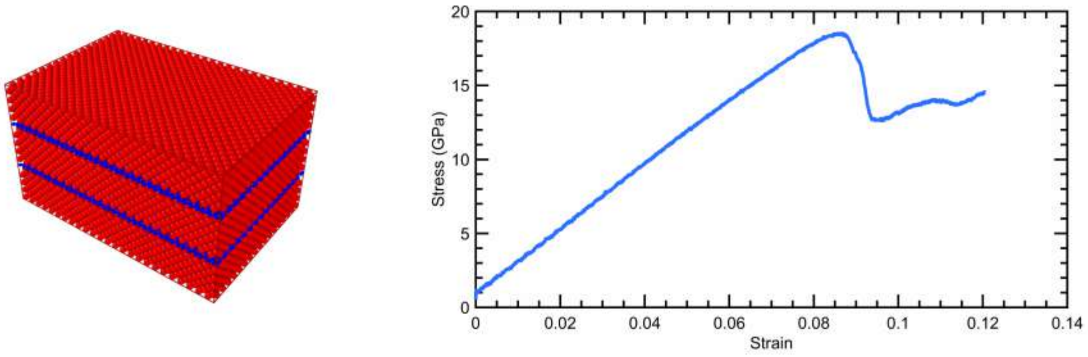

Figure 4.12: Stress-strain curve for two layered Graphene NC

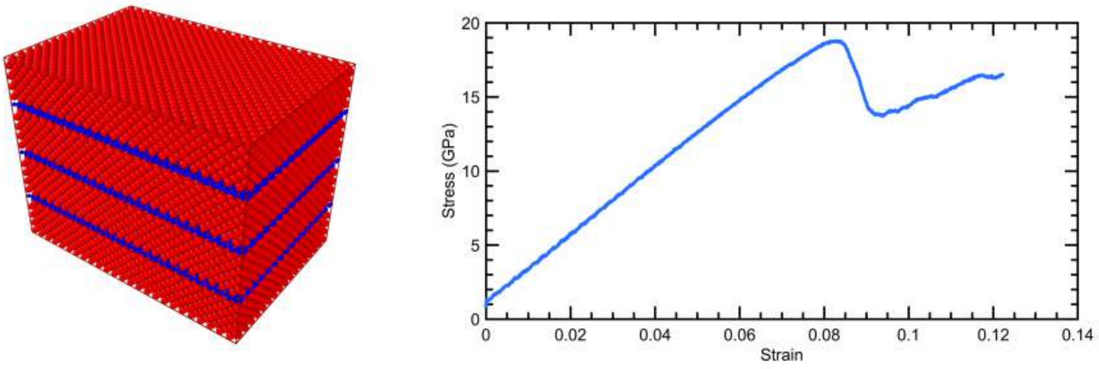

Figure 4.13: Stress-strain curve for three layered Graphene NC

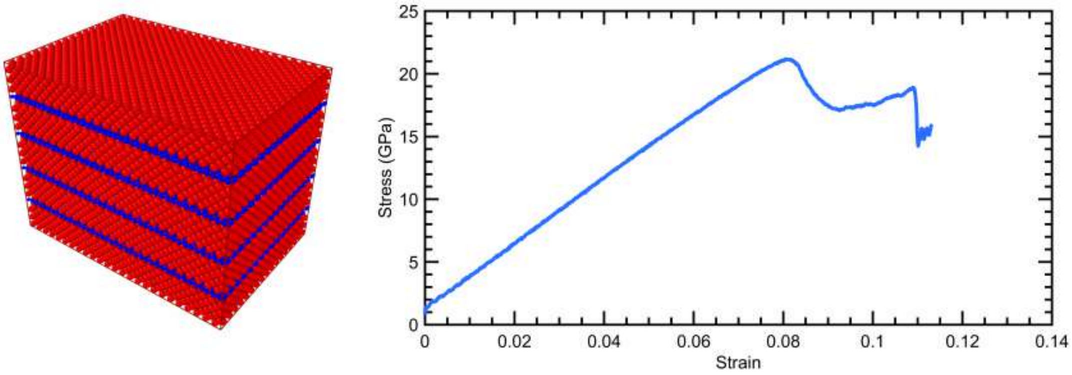

Figure 4.14: Stress-strain curve for four layered Graphene NC

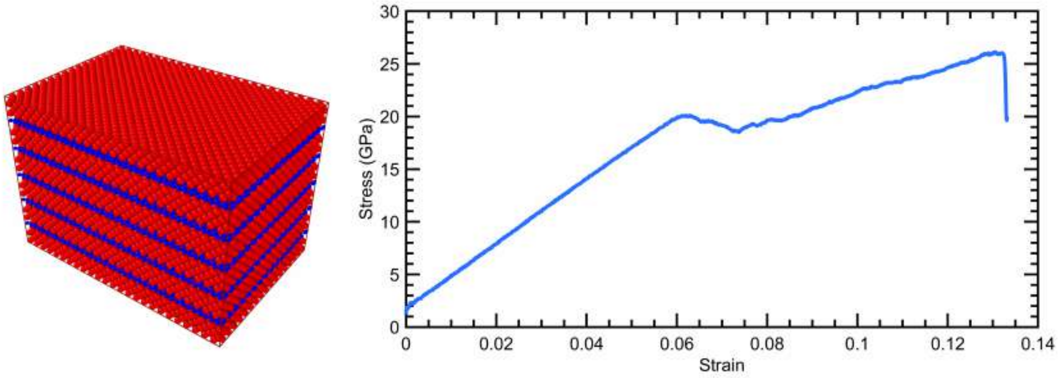

Figure 4.15: Stress-strain curve for five layered Graphene NC

As previously shown, Pt-Gr NC has better mechanical strength than its pristine Pt counterpart, almost a 26% increment occurs with the inclusion of a single layer of Gr into the Pt system. Moreover, this characteristic receives an additional 10.67% increase when a single- to a double-layer addition of Gr is considered. This may be comprehended by examining the progression of dislocation shown in Fig. 4.17 (as the figures show dislocations at different stress levels marked in Fig. 4.16), which reveals that the two Gr sheets effectively constrained the dislocations that originated from the central Pt layer (Fig. 4.17 (a)(b)), resulting in the strengthening effect. The specific coordinates of the Gr relative to the locations of high stress concentrations may have served as nucleation sources for dislocations [97], dislocations emerged and rapidly filled the upper and lower regions (Fig. 4.17 (c)(d)), causing the sharp stress drop at B and the subsequent lower flow stress between B and C (Fig. 4.16).At point C, Gr-1 fragmented (fig: 4.17 (e)), resulting in a further decrease in stress. After point C, dislocations were able to spread via the spaces between the shattered Gr fragment, resulting in the weakest strengthening effect. Therefore, it shows that fragmented Gr fragments no longer functioned as efficient barriers against the transmission of dislocations. The Gr layer had a length same as the Pt matrix, indicating that Gr underwent a very substantial in-plane strain by deforming with the Pt matrix as a result of PBC. Similar types of mechanism for nucleation and propagation of dislocation can be found with the increment of graphene layers. As an example Fig. 4.18 depicts the similarity in mechanism for a 3 graphene layered Pt-Gr NC with the previously discussed 2 layer of graphene in Pt-Gr NC.

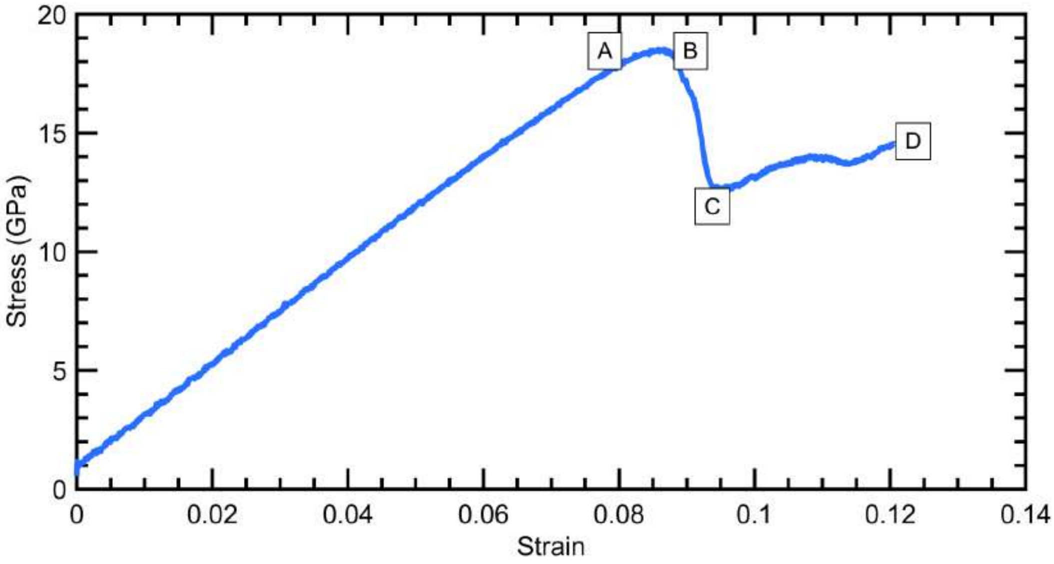

Figure 4.16: Stress-Strain curve of a double Gr layered NC

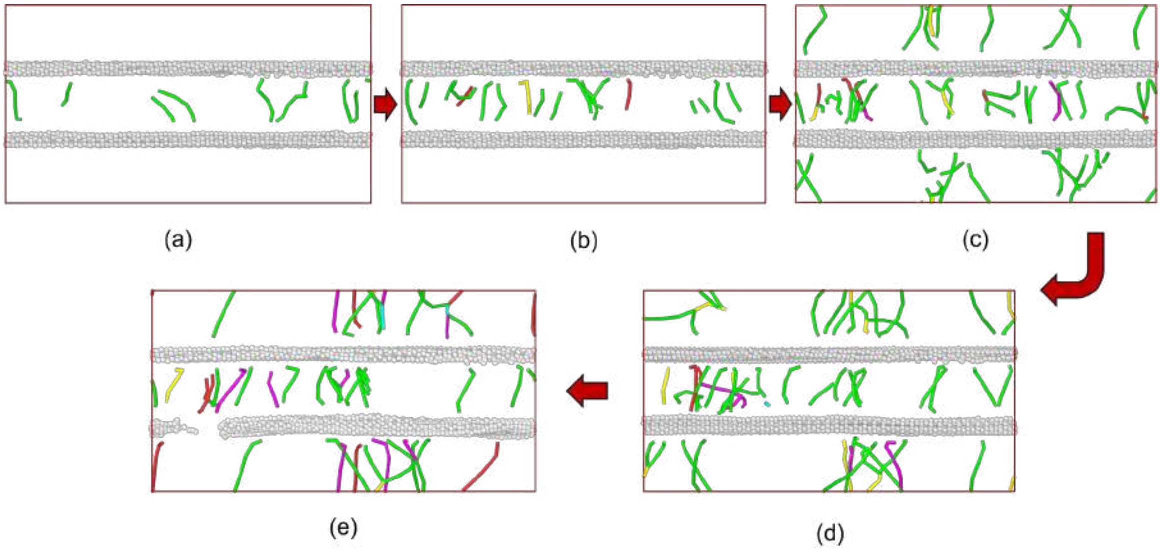

Figure 4.17: Evolution of Nucleation and propagation of dislocations for double layered graphene NC

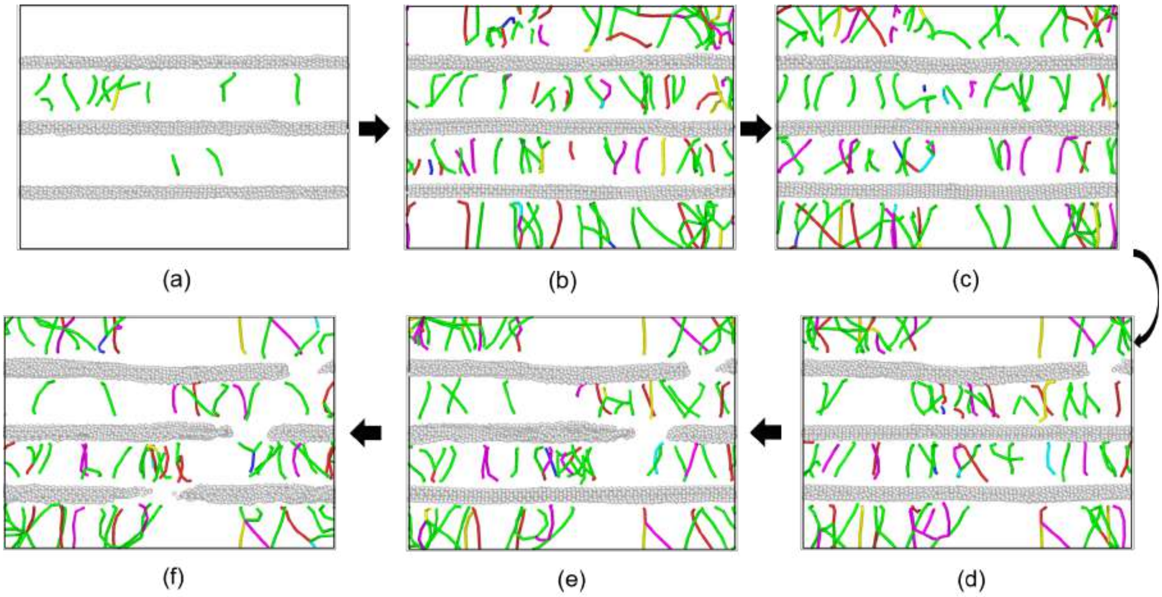

Figure 4.18: Nucleation and propagation of dislocation for tripple layered graphene NC

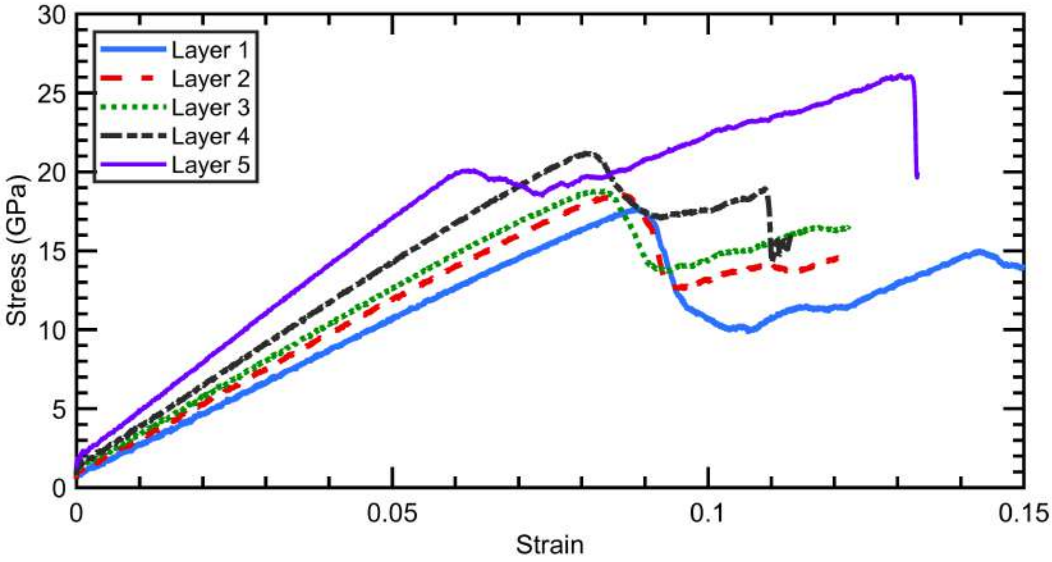

Figure 4.19: Stress-strain curve for different layered Graphene NC

Table 4.2: Young's modulus and Yield strength for different layers of Graphene

Number of Graphene layers	**Young's Modulus (GPa)**	**Yield strength (GPa)**	**Ultimate strength (GPa)**
One	199.3007	17.5174	17.6327
Two	220.5475	18.1812	18.5332
Three	230.8059	18.6726	18.8000
Four	261.0321	20.9068	21.1783
Five	305.8554	19.7520	22.3929

With the addition of Graphene layers, the material's mechanical properties are on the rise, as shown by the table 4.2. It shows that there is an upward trend in the material's mechanical properties with the inclusion of Graphene layers. This type of behavior is anticipated because the fiber material, Graphene sheet, is mechanically stronger.The modulus of elasticity as well as yield strength increase with the addition of Graphene layers. The spiralling line of progression is very close to being linear, as can be seen in Fig. 4.20 and Fig. 4.21. Perfect linearity could have been achieved if the dimensions of Pt layers were consistent throughout each model. Due to the fact that increasing the number of atoms in a material requires more computational time and power, it was not feasible to achieve dimensional continuity in the Pt layer for different layered NC.

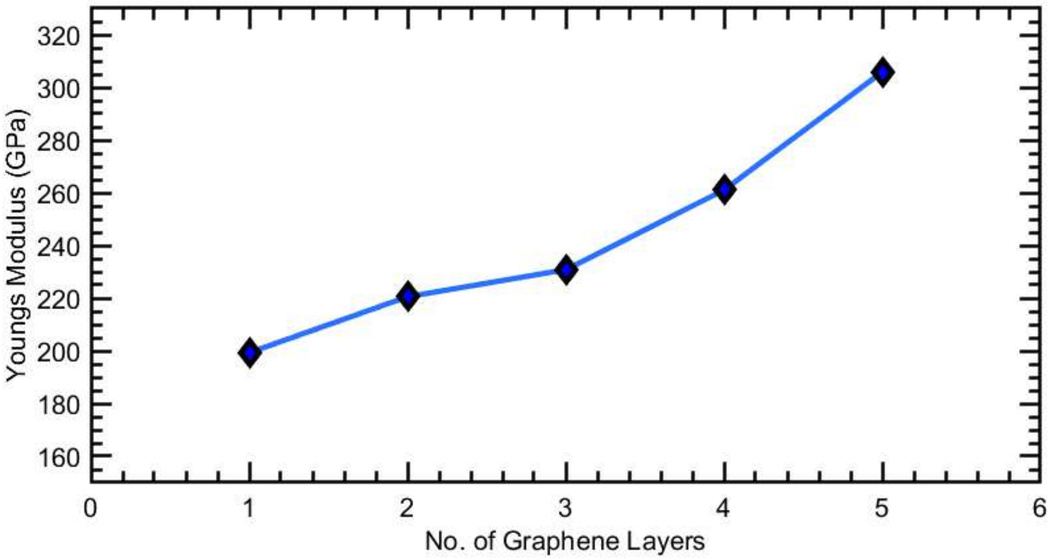

Figure 4.20: Young’s modulus vs different layers of Graphene NC

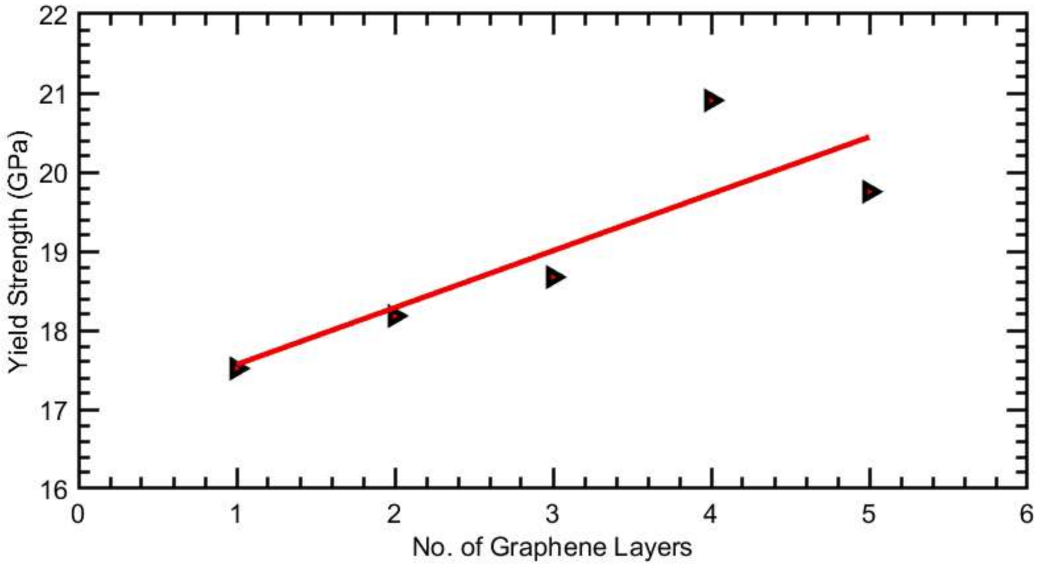

Figure 4.21: Yield strength vs different layered Graphene NC

4.3.4 Temperature effect on mechanical properties of Pt-Graphene NC

In this section, the impact of temperature on the mechanical properties of the NC samples from 300 K to 700 K is investigated. Figures from Fig. 4.22 to Fig. 4.26 depict the stress-strain curve for double graphene layered NC at various temperatures.

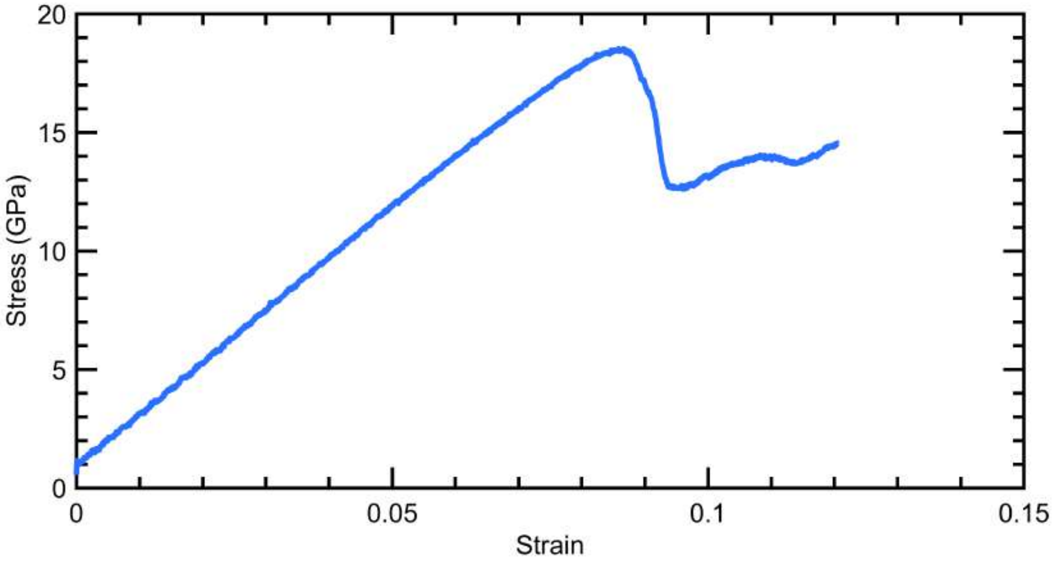

Figure 4.22: Stress-strain curve at 300K

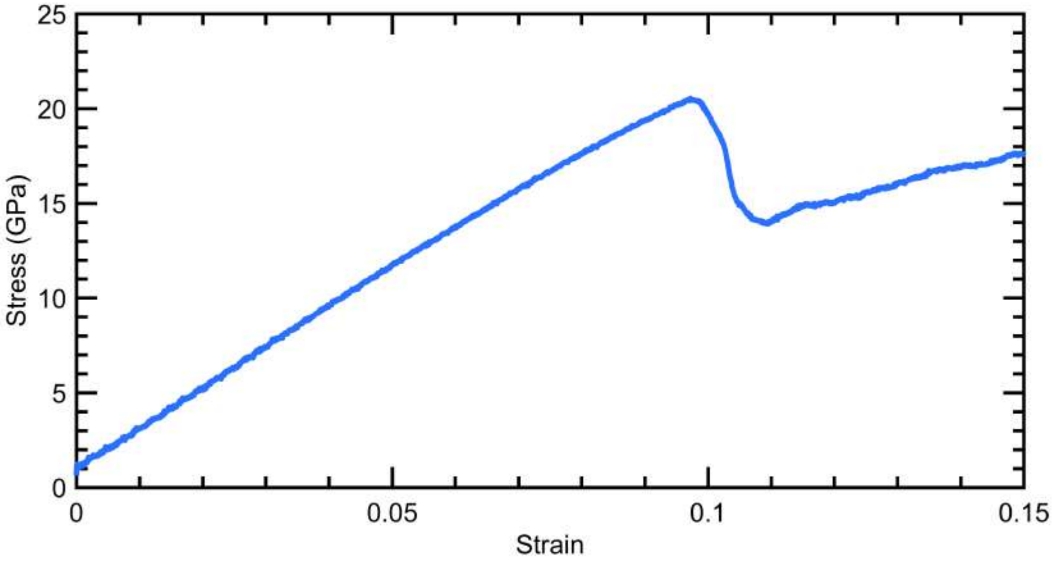

Figure 4.23: Stress-strain curve at 400K

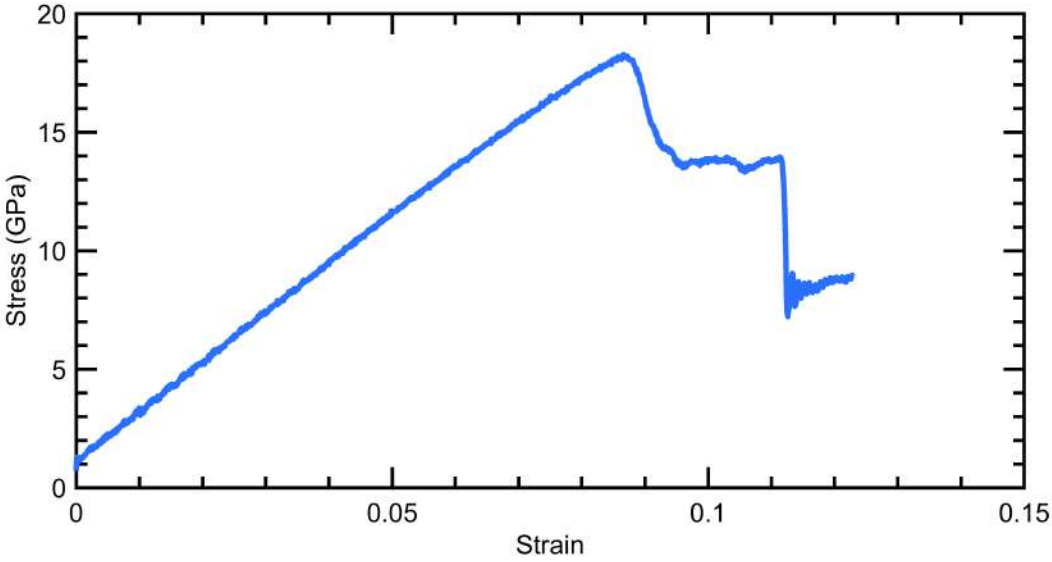

Figure 4.24: Stress-strain curve at 500K

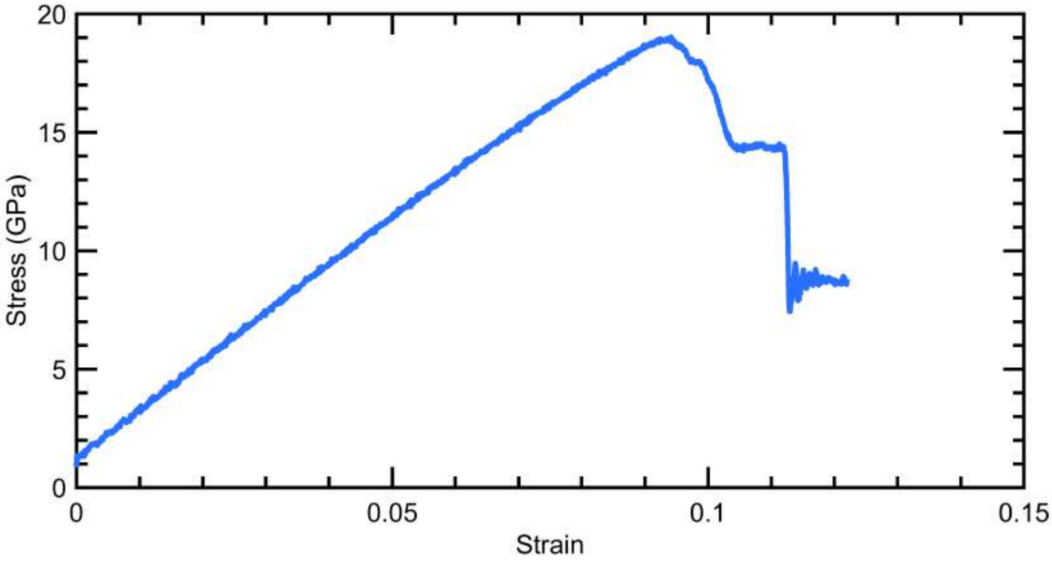

Figure 4.25: Stress-strain curve at 600K

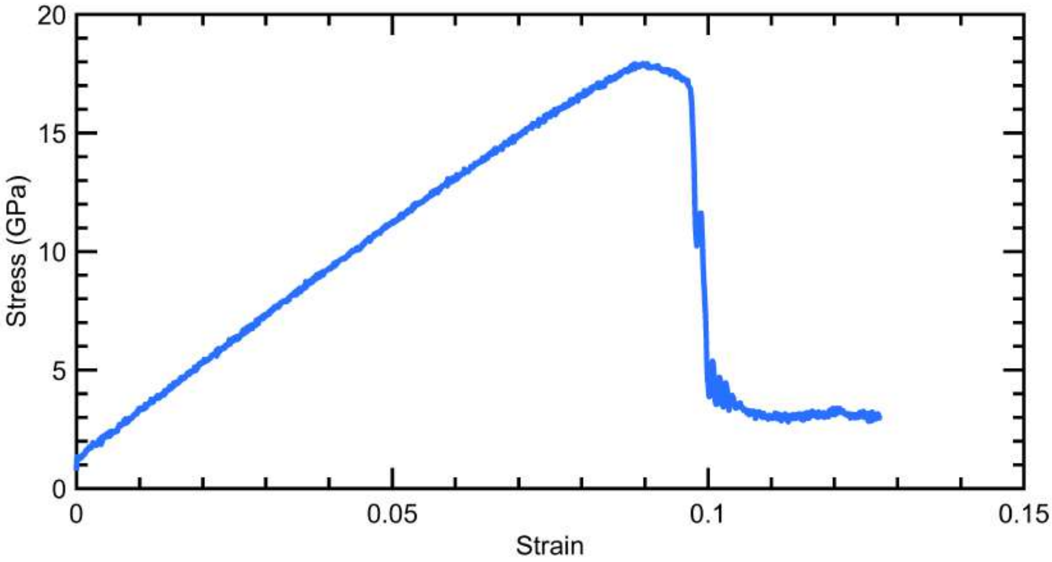

Figure 4.26: Stress-strain curve at 700K

The stress-strain curve for double-layered Pt-Gr NC at different temperatures is shown in Fig. 4.27. The graph reveals a linear-elastic region after which yielding occurs and stress reduces. As temperature increases, from 300 K to 700 K, the Young modulus of the NC falls. Young's modulus decreases by almost 2.23% for every 100 K rise in temperature, from 217.3914 GPa at 300 K to 212.5472 GPa at 400 K. The relevant data is listed in Table 4.3 and the trend can be seen from Fig: 4.28. This decreasing pattern continues as the temperature rises. This softening behavior is observed in NC. High temperatures increase the atomic energy level, hence lowering their elasticity. Additionally, heating decreases the needed tension for plastic deformation to start and proceed. High temperatures diminish the elasticity and plasticity of materials because they enhance the energy levels of the atoms, hence facilitating atomic displacement. Fig. 4.29 further demonstrates that the yield strength is decreasing by temperature variations.

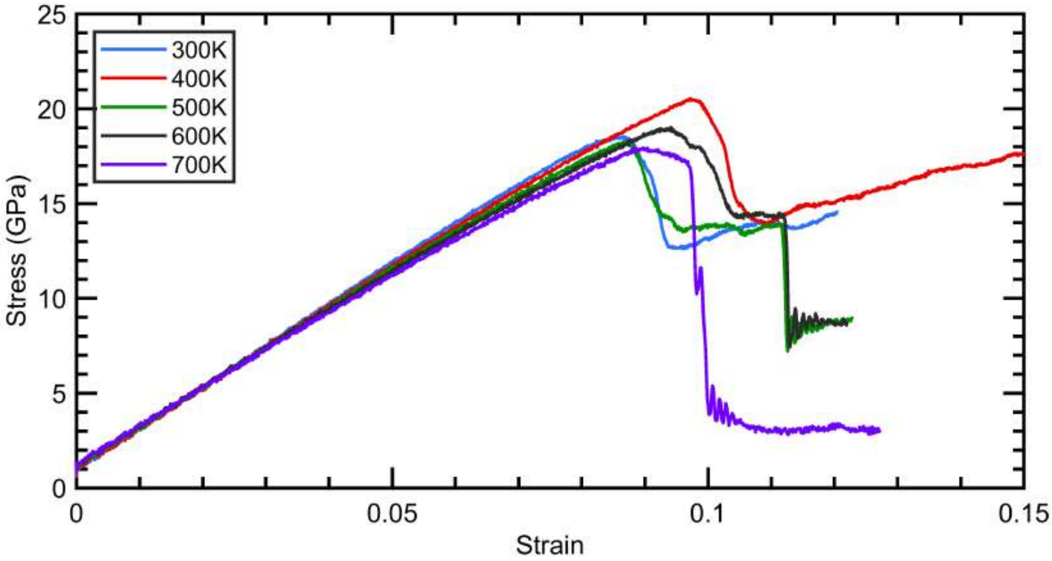

Figure 4.27: Stress-strain diagram of Pt-Graphene NC for different temperatures

Table 4.3: Young's modulus and Yield strength for different temperatures

Temperature (K)	**Young's Modulus (GPa)**	**Yield strength (GPa)**	**Ultimate strength (GPa)**
300 K	220.5475	18.18117	18.5332
400 K	215.7699	19.16936	20.5496
500 K	209.6517	18.18453	18.2787
600 K	206.2417	18.54517	19.0285
700 K	200.2166	17.93656	17.9366

For a comparison of how the mechanical properties have increased for Pt-Gr NCs than its pristine Pt counterparts, a series of simulations were also done on the pristine Pt for a temperature range of 300K to 700K. An interesting pattern for the values of yield strength and ultimate strength was found for Pt-Gr NCs than pristine Pt. With the increment of temperature an decrement trend was found for these values for pristine Pt which is expected in general. But in case of Pt-Gr NCs, these values were remained almost similar throughout the temperature range of selection. This phenomena denotes an excellent improvement of mechanical properties due to the inclusion of graphene sheet into Pt which might be applied to high temperature applications where no significant change in mechanical properties are expected.

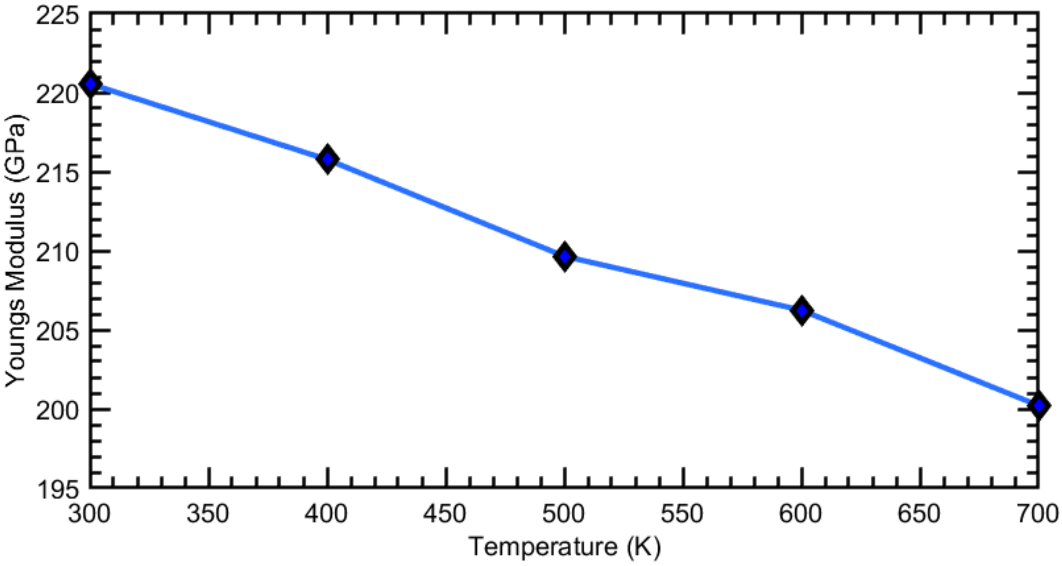

Figure 4.28: Young’s modulus vs Temperature

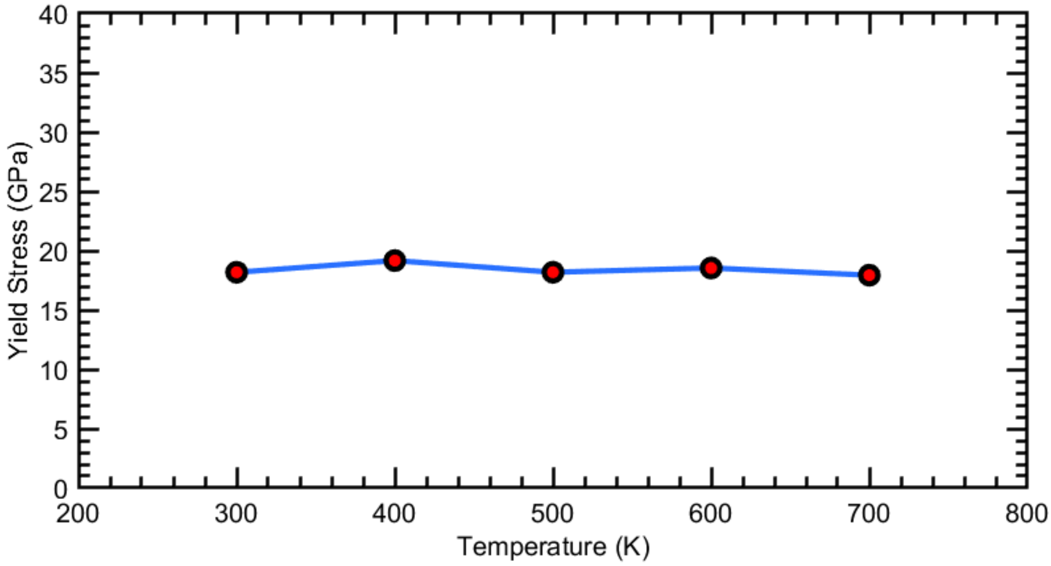

Figure 4.29: Yield strength vs Temperature for Pt-Gr NC

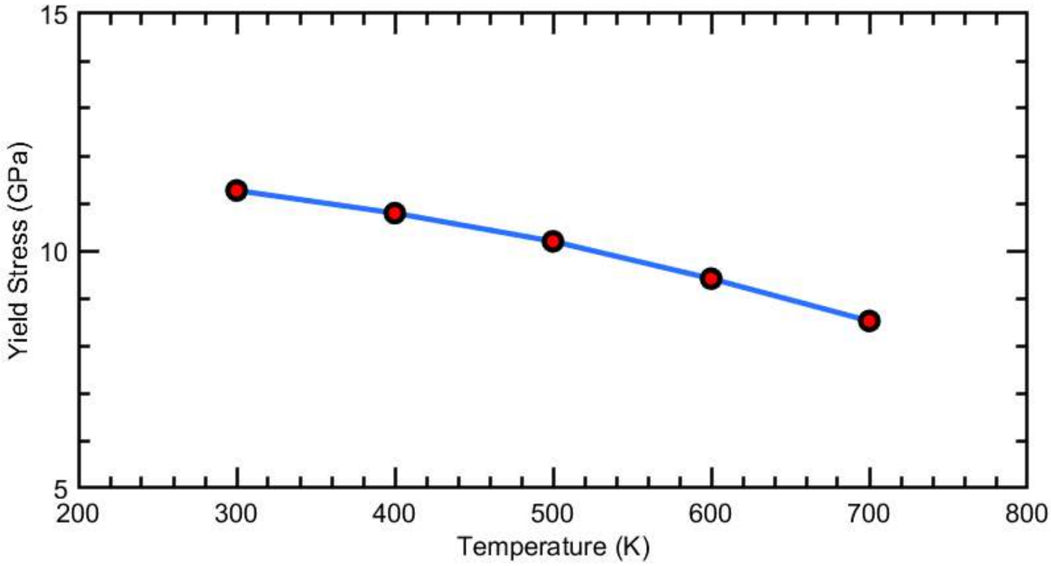

Figure 4.30: Yield strength vs temperature for Pristine Pt

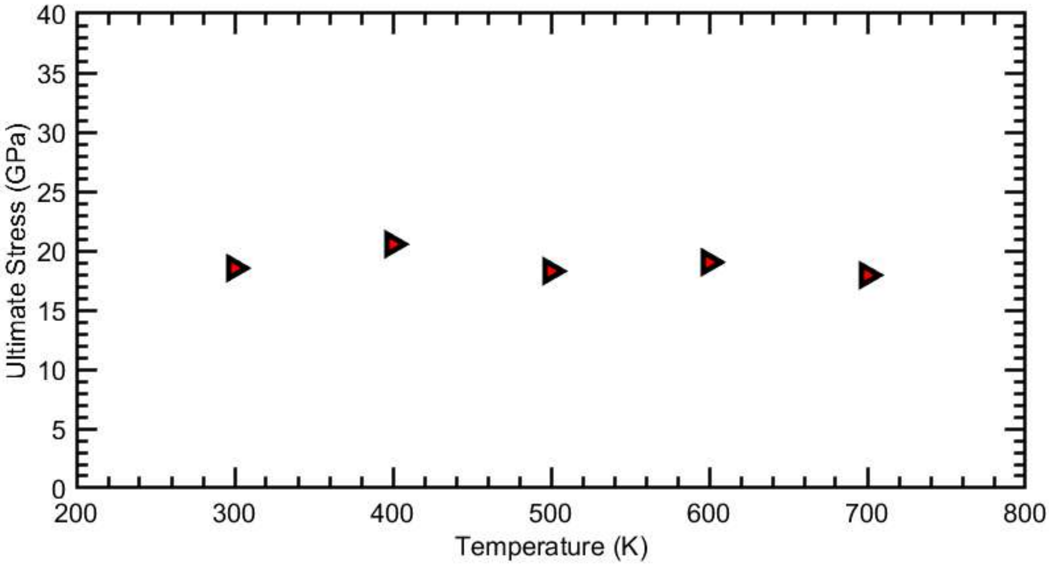

Figure 4.31: Ultimate strength vs temperature for Pt-Gr NC

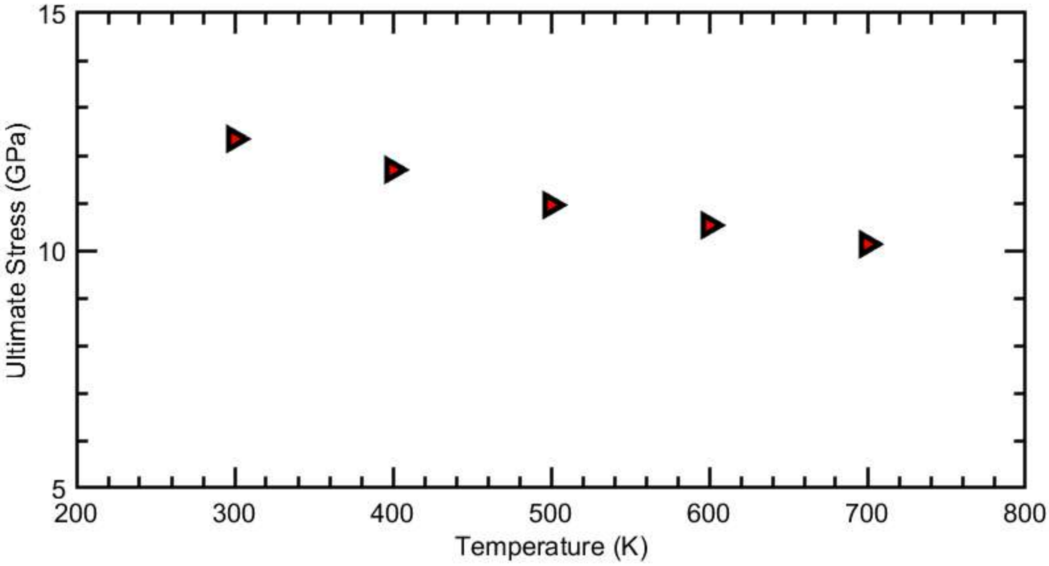

Figure 4.32: Ultimate strength vs temperature for Pristine Pt

4.4 Section Summary

A tension testing model is established for the Pt-Gr NCs, which is verified by a series of parametric studies. Major conclusions from this chapter are summarized below:

- Primary phenomena responsible for the tensile deformation of a Pt- Gr NC are the nucleation and propagation of partial dislocations.
- In the case of NCs that have periodic BC in the axial direction, initial stresses or strains that are not zero will be seen.
- The addition of Gr layers results in an enhancement in the mechanical characteristics of the Pt-Gr NC, according to the formulae for composite materials which is verified through stress-strain curve obtained by MD simulations.
- Temperature exerts a significant influence on Young's modulus which is with the increment of temperature Young's modulus decreases.
- Although increment in temperature has an impact on the yield strength and ultimate strength of the pristine Pt, Pt-Gr NC has shown very insignificant variation of these properties.

Chapter 5

Mechanical Properties: Bending Test

It took many years to obtain an understanding of the stresses created in beams by bending. Galileo worked on this topic, but today's theory is mostly due to the famous Swiss mathematician Leonard Euler (1707–1783). As will be explained in further detail below, beams create normal stresses in the longitudinal direction that range from maximum tension at one surface to zero at the beam's midplane to maximum compression at the other surface. When the length-to-height ratio of the beam is considerable, shear stresses are also generated, although they are typically insignificant in compared to normal stresses. In this chapter, a discussion on the effect of bending load is studied on the Pt-Gr NC.

5.1 Theoretical Background

A beam subjected to a positive bending moment will tend to develop a concave upward curvature. At the transition between the compressive and tensile regions, the stress becomes zero. If the material is strong in tension but weak in compression, it will fail at the top compressive surface. This might be observed in a piece of wood by a compressive buckling of the outer fibers.

5.1.1 Stresses in Beam

Flexural load in a beam creates internal stresses which are represented by shear force and bending moment. Normal forces in the cross section of the beam generate a bending moment or stress. For a situation of pure bending, the shear force inside the beam must be zero.

Consider that a beam is composed of sets of fibers. When it goes through bending stress, its upper fiber gets shorter due to compression, and its lower fiber under tension gets longer.

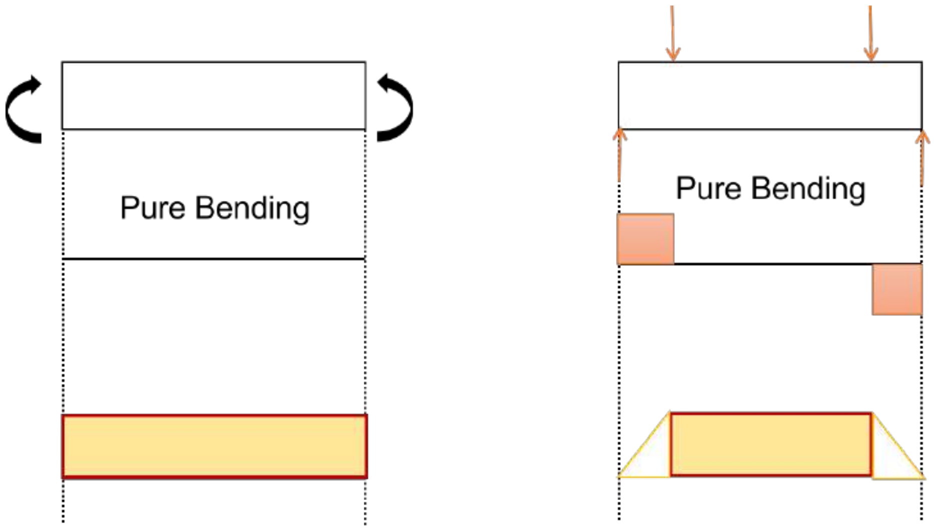

Figure 5.1: Conditions of pure bending.

There exists, somewhere between these fibers, a neutral axis whose form does not change. Let a beam, depicted in the Fig. 5.2, has a neutral axis (NA) AB and another fiber is in the y distance from the NA, CD. If the beam goes under pure bending, then the NA remains the same as before deformation. Fiber CD goes under deformation.

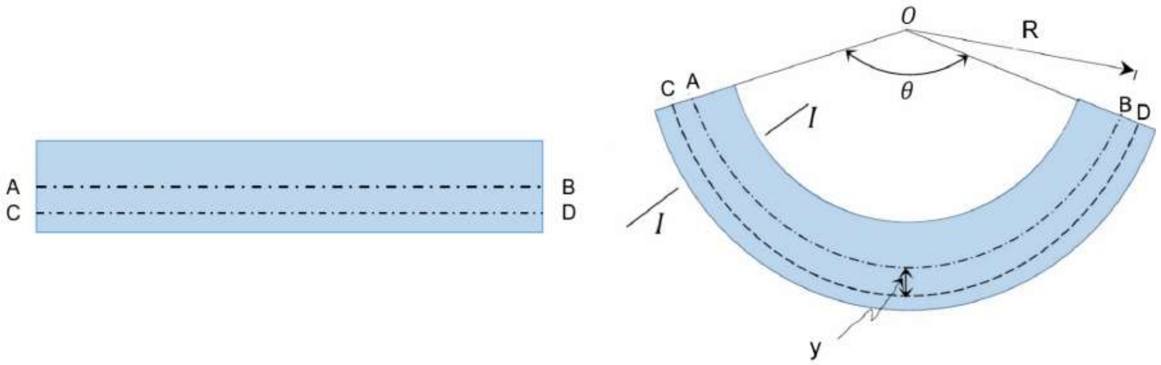

Figure 5.2: Elastic curve of a beam.

From the Fig. 5.2, let O be the beam's center and R its radius of curvature. At O, the beam subtends an angle θ. The lengths of the neutral axis of the beam AB and the fiber CD may be calculated as follows:

$$AB = R\theta \tag{5.1}$$

$$CD = (R + y)\theta \tag{5.2}$$

As we know, strain is the ratio of change in any dimension over that dimension at initial condition. We may calculate strain, CD is elongated as in tension, at the beam due to bending as follows:

$$\epsilon = \frac{\delta L}{L_o} = \frac{CD - AB}{AB} = \frac{(R+y)\theta - R\theta}{R\theta} = \frac{y}{R} \tag{5.3}$$

According to Hooke's law, the strain (deformation) of an elastic object or material is proportional to the stress applied to it [98]. Therefore, normal stress in the beam can be written as -

$$\sigma = E\epsilon = E\frac{y}{R} \tag{5.4}$$

If a differential area δA at a distance y from the NA of the beam is under a bending stress σ, then the differential force on this area may be written as:

$$\delta F = \sigma \delta A \tag{5.5}$$

So, total load can be obtained through integration,

$$F = \int \sigma \delta A \tag{5.6}$$

The external moment M in the beam is balanced by the moments around the neutral axis of the internal forces created at a portion of the beam when static equilibrium is considered. Therefore,

$$M = \int (\sigma \delta A) y$$

$$M = \int (E\frac{y}{R}\delta A) y = \frac{E}{R}\int_A y^2 \delta A \tag{5.7}$$

Here, $\int_A y^2 \delta A$ is the area moment of inertia, I, which is the resistance of a cross section to bending due to its shape. Therefore,

$$M = \frac{E}{R} I = \frac{\sigma}{y} I \tag{5.8}$$

The stress changes linearly from zero at the neutral axis to a maximum at the outer surface, it varies inversely with the cross section's moment of inertia, and it is independent of the material's characteristics.

According to differential calculus, the curvature of a curve, which is defined as quantifica-

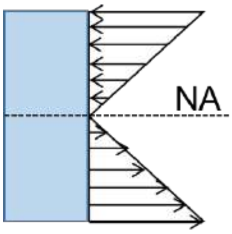

Figure 5.3: Stress distribution of the beam.

tion of the change of direction of a curve, can be expressed as,

$$\frac{1}{R} = \frac{\frac{d^2y}{dx^2}}{\left[1 + (\frac{dy}{dx})^2\right]^{3/2}} \tag{5.9}$$

Since the beam in Fig. 7.1 is assumed to be homogeneous and behaves in a linear elastic manner, its deflection under bending is small.

Since the beam is considered to be linear elastic and homogeneous, its deflection due to bending should be small. Therefore,

$$\frac{1}{R} = \frac{d^2y}{dx^2} \tag{5.10}$$

Replacing this value into Eq. 5.8 gives the differential equation of the elastic curve of a beam,

$$EI\frac{d^2y}{dx^2} = M \tag{5.11}$$

5.1.2 Different Beam Theories

A beam deforms and develops internal stresses when subjected to a transverse load. In the quasi-static scenario, it is assumed that the amount of bending deflection and stresses that occur do not vary with time. In a horizontal beam supported at both ends and loaded downward in the center, the material on the upper side is crushed while the material on the lower side is stretched (refer to Fig. 5.4)

Using a technique developed from continuum beam theory, the effective Young's modulus of nanowires resulting from bending simulations may be computed. For tiny deflections generated by a concentrated load, the strain energy δU of a beam may be calculated as follows:

$$\delta U = \int_0^L \frac{EI}{2}(\frac{d^2v}{dx^2})^2dx \tag{5.12}$$

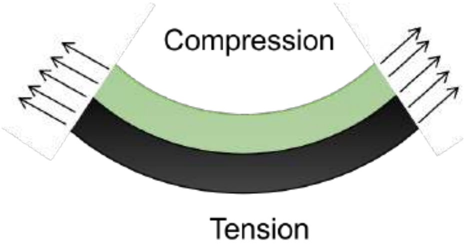

Figure 5.4: Portion of a beam going under bending load, where the upper portion is going through compression and the lower portion is having tension.

where L represents the length, E represents Young's modulus, I represents the moment of inertia, v represents the beam deflection, and x represents the axial coordinate [99].

If a beam is long enough ($\frac{L}{t}$ >8, where t is height), just the effects of the bending moment on the strain energy are examined, then the energy resulting from shear deformation may be disregarded [99].

From continuum theory, the deflection v of a doubly clamped beam with a concentrated load P at the middle is given by,

$$v = -\frac{Fx}{12EI}(\frac{3L^2}{4} - x^2) = -\frac{48\delta x}{12L^3}(\frac{3L^2}{4} - x^2) \tag{5.13}$$

where δ is the maximum deflection at the free end of the beam. The second derivative, which is known as the curvature, of Eq. 5.13 is,

$$\frac{d^2v}{dx^2} = \frac{24\delta}{L^3}(1 - 4\frac{x}{L}) \tag{5.14}$$

At each bending increment, Young's modulus E is computed for each nanowire by putting the determined curvature into the strain energy Eq. 5.12, integrating with respect to x, and then solving for Young's modulus E. This approach enables the determination of Young's modulus using just strain energy, deflection, and geometric characteristics; forces or stresses are not explicitly employed [100].

Utilizing continuum equations, the moment of inertia (I) is computed. The moment of inertia is sensitive to the specification of cross-sectional area at the atomic level. Computation of the area is done as a continuous object with boundary dimensions specified as the distance between the atomic points. While this analysis alters the magnitude of the predicted modulus, it has no effect on the observed trends. Pertaining to rectangular cross sections,

$$I = \frac{bh^3}{12} \tag{5.15}$$

where h is the height and b is width of the relaxed cross section.

Under investigation, Diao et al. [95] developed an energy-based continuum-mechanical approach for determining Young's modulus for nanowires in tension. At each increment of tensile loading, the axial stress inside the nanowire is balanced by the externally provided quasi-static force at its tip. Consequently, the change in potential energy in the nanowire during loading is equivalent to the work performed by the externally applied load,

$$\delta U = \int_0^{\Delta L} F d(\Delta L) = \int_0^{\epsilon} V \sigma d\epsilon \tag{5.16}$$

The Euler–Bernoulli beam theory (also known as engineer's beam theory or classical beam theory) is a simplification of the linear theory of elasticity that allows for the calculation of the load-carrying and deflection properties of beams. It addresses the situation of modest deflections of a beam subjected exclusively to lateral stresses. Thus, it is a Timoshenko beam [101] theory special case. According to the traditional Euler-Bernoulli beam theory, the governing equation of the double clamped narrow beam under pure bending is [102]:

$$(EI)w^4 = 0 \tag{5.17}$$

Here, E is Young's modulus, w is the beam deflection, and I is the moment of inertia. Eq. 5.17 is solved using the usual clamped boundary conditions at both ends, with a constant load F applied at the midpoint x = L/2 of the NW, i.e., the transverse displacement and slope are zeros at x = 0, and the slope at x = L/2 is also zero because of symmetry. The force equilibrium's at x = 0 is, $-(EI)w^3 = \frac{F}{2}$. The relationship between the applied load F and the resulting displacement d can be deduced as,

$$F = \frac{192(EI)}{L^3} d \tag{5.18}$$

The yield strength σ_y is then estimated from the yield force F_y in the F-d curve before the onset of plastic deformation according to [103]

$$\sigma_y = \frac{3F_y L}{4h^3} \tag{5.19}$$

Experimental (Heidelberg et al., 2006) and numerical simulation (MD) findings indicate that the axial extension has a significant impact on the beam behaviors. Taking into consideration the axial extension effect, the following solution is obtained [100]:

$$F = \frac{192(EI)}{L^3} f(k) d \tag{5.20}$$

$$f(k) = \frac{k}{48 - 192 tanh(\sqrt{k}/4)/\sqrt{k}} \tag{5.21}$$

k is exactly proportional to the axial tension. Likewise, k is known as an axial extension effect factor [100]. Following is a transcendental equation relating the axial extension impact factor to the maximum displacement d,

$$\frac{k cosh^2(\sqrt{k}/4)}{2 + cosh(\sqrt{k}/2) - 6 sinh(\sqrt{k}/2)/\sqrt{k}} (1 - 4\frac{tanh(\sqrt{k}/4)}{\sqrt{k}}) = d^2 \frac{EA}{EI} \tag{5.22}$$

Obviously, Eq. 5.22 is complex in nature and a numerical solution is required. Thus, the following asymptotic solution is constructed,

$$k = \frac{6s(140 + s)}{350 + 3s} \tag{5.23}$$

$$s = d^2 \frac{A}{I} \tag{5.24}$$

5.2 Simulation Methodology: Bending Test

The Fig. (5.5) shows a three-point bending model for a double clamped NC according to the Atomic Force Microscopy (AFM) bending method. It has been observed that prior works directly use forces or displacement. The load was applied using a virtual nanoindenter to simulate the actual AFM bending scenario. Only the X- and Y-axes were subject to periodic boundary conditions, and the Z-direction was subject to shrink-wrapped boundary conditions. At the midpoint of the double-clamped NC beam, a cylindrical virtual indenter is used to exert force on the NC and simulate the effect of bending. The virtual tip is made rigid for the simulation. In each simulation, the tip had a 1.0 nm radius which was consistent with previous works and was cylindrical. A constant loading rate of 10 m/s was applied on the tip for every simulation.

The mobile and boundary regions make up the two divisions of the NC. Atoms at both ends of the boundary regions were held in place throughout the entire incremental loading process by a boundary condition with zero force. A 300 k temperature was maintained. The NC underwent energy minimization using the conjugate gradient method before the application of bending deformation; this energy minimization causes atoms close to free

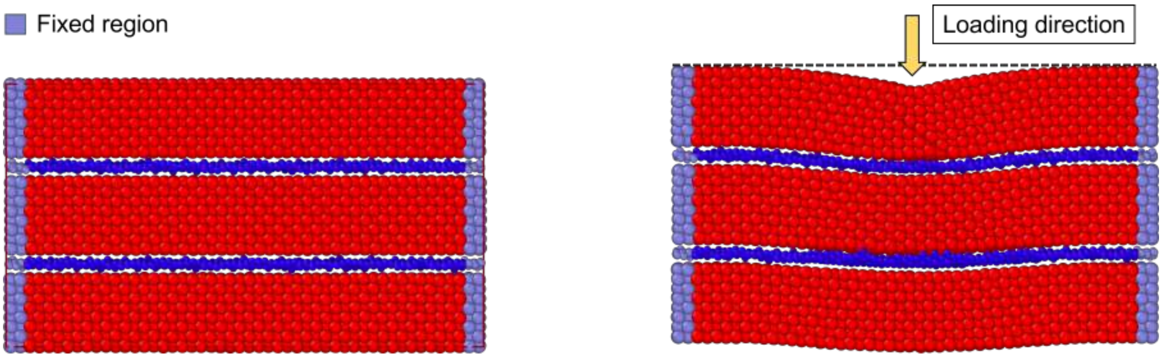

Figure 5.5: Setup for Bending simulation for a double layered Pt-Gr NC.

surfaces to contract. The loading process then began, and various mechanical parameters were evaluated using the force-deflection curve that was produced.

The bending deformation of NWs is further revealed by the virial atomic stress tensor, which is defined as:

$$\sigma_{\alpha\beta} = -\sum_{i} m_i v_i^{\alpha} v_i^{\beta} + \frac{1}{2}\sum_{i}\sum_{j\neq i} F_{ij}^{\alpha} F_{ij}^{\beta} \tag{5.25}$$

where r_{ij} is the distance between atoms i and j, m_i and v_i are the mass and velocity of atom i, F_{ij} is the force between atom i and j, and the indices α and β signify the Cartesian components.

5.3 Parametric Study

5.3.1 Validation with Tensile Test Result

The Young's modulus, also known as the modulus of elasticity, E, is a property that is unique to each material. Different materials possess different values of Young's modulus for an obvious reason. It is reasonable to anticipate that the Young's modulus will remain unaffected by the loading conditions when dealing with isotropic materials. Therefore, the value of E should be nearly equal for both axial (tension) and transverse (bending) loadings. Zhan et al. hypothesized that, as analysis techniques improved over time, the E value caused by these two loading conditions would be comparable [104]. Other research has suggested that the Youngs modulus resulting from a bending test is significantly higher than that resulting from a tensile test [92]. To verify these different opinions, both tensile and bending tests have been conducted on a Pristine Pt sample at a temperature of 300 K.

From the previous chapter (Ch. 4), the Youngs modulus due to tensile test is found to be 142.35 GPa (Refer to Table 4.1), whereas bending test gives a value of 374.74 GPa according to Modified-Euler equation. These results confirms the claim made by Diao, et

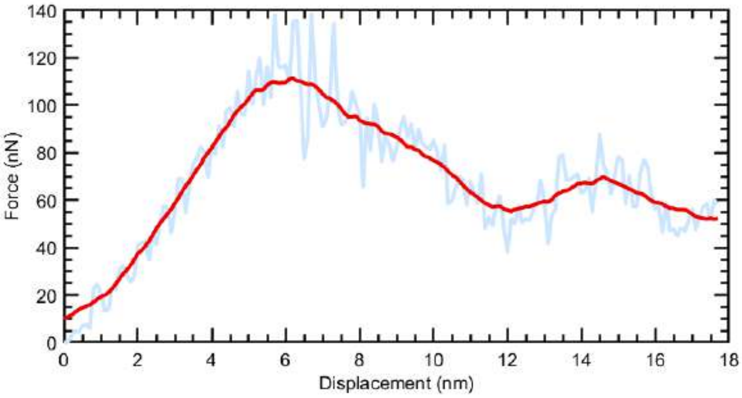

Figure 5.6: Force-deflection curve for Pristine Pt

el. [92].

Afterwards the verification these different opinions is done on Pt-Gr NC. Both tensile and bending tests have been conducted on a Pt-Gr NC sample with a double layers of graphene at a temperature of 300 K.

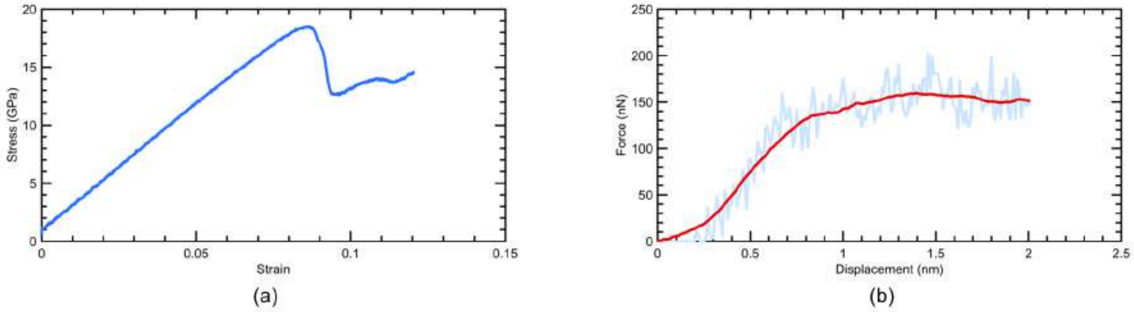

Figure 5.7: (a) Strain-stress curve due to tensile loading (b) Force-deflection curve under bending.

From the Fig. (5.7) calculated Young's modulus for both the tensile test and bending test is given in the table below:

Table 5.1: Comparison of the values of Young's modulus for both tensile and bending test

Young's Modulus	**Young's Modulus**	**Young's Modulus**
Tensile Test (GPa)	Bending Test (GPa) *Euler equation*	Bending Test *Modified-Euler equation*
217.3914	11.5906	21.5422

Results from both the tensile and bending tests reveal a significant discrepancy in the calculated Young's modulus for Pt-Gr NC. Previous research on copper nanowire has shown that the Young's modulus for both tests is very similar [100]. Therefore, to find out the possible reasons or reasons behind the anomaly in the Young's modulus for our present study on Pt-Gr NC, a thorough analysis has been conducted on the failure mechanism under bending load, which is presented in the following subsection.

5.3.2 Failure Mechanism

In this simulation process, a virtual indenter is used to perform the work of loading at the model beam's center. This indenter is shaped like a cylinder to induce a uniform plane load across a portion of the beam [105, 106]. The tip radius is 1.0 nm. During nanoindentation, the virtual tip resembles the spherical indenter tip used by previous researchers, but has no actual shape. Specifically, the virtual tip will exert a force of repulsion between the tip and the NW, which is expressed as $F(r) = -k(r - R)^2$ here, k is the prescribed force constant, r equals to the distance between the atom and the tip's center, and R is the tip's radius.

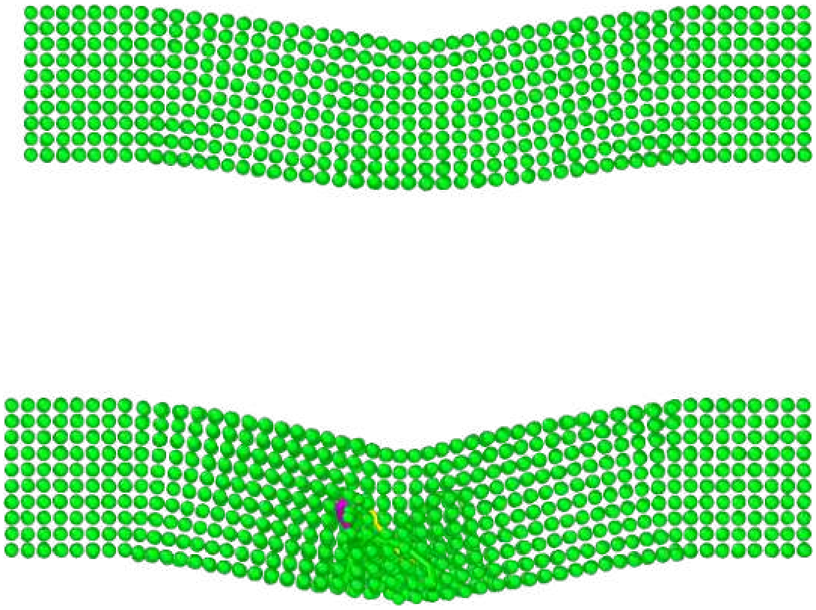

Figure 5.8: Failure mechanism for Pristine Pt under lateral loading

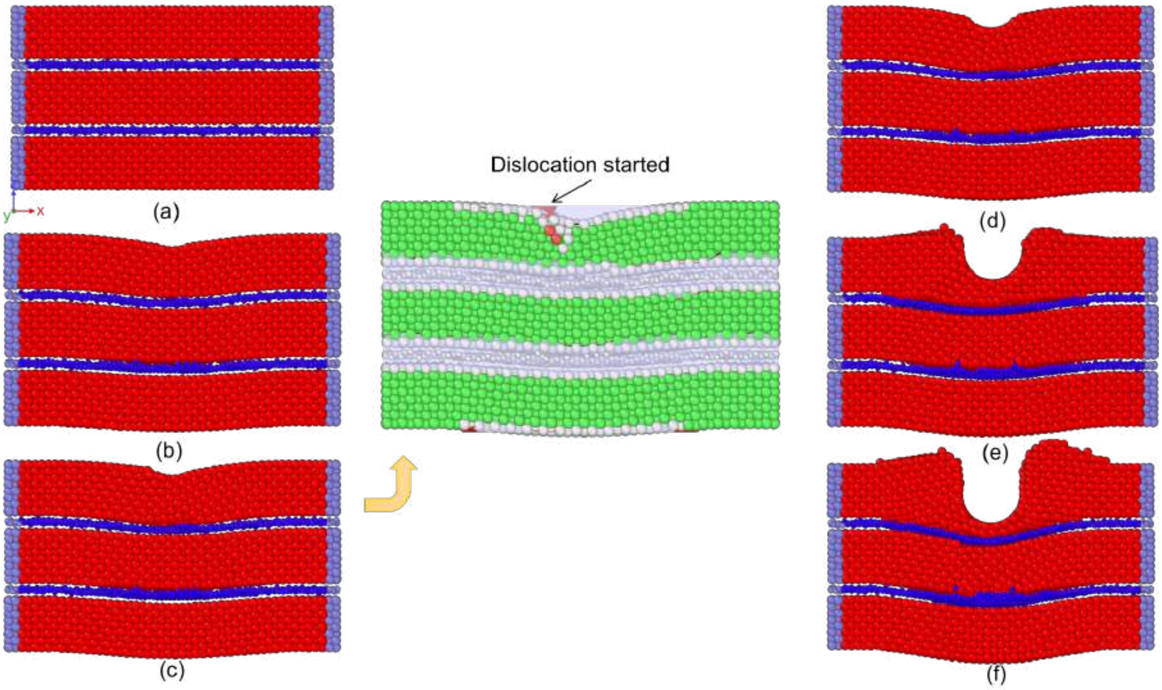

Figure 5.9: Steps of Pt-Gr NC material failure under bending loads.

Atomic configuration of NC under bending at (Fig. 5.9 (a-c)) indicates that, dislocation started much earlier than expected at a deflection of 4.34 Åon the outer Pt layer. Further loading leads the test sample towards the plastic failure of the upper Pt layer, whereas the following graphene layer and also the other layers, followed by the graphene layer, do not show any sign of plastic deformation (Fig. 5.9 (d-f)).

At the nanoscale, it is well known that the impact of surface to volume ratio is visible. When bending stresses are applied to the NC, the graphene layer produces a greater surface-to-volume ratio than the platinum layer. According to prior research, when the surface-to-volume ratio rises, the characteristics of materials improve. Due to this event, it is possible to assume that the upper Pt layer broke prematurely because it failed to convey the bending action to the Gr layer, which has better strength.

To further investigate the surface-to-volume ratio effect, another NC has been modeled with a single layer graphene having more surface-to-volume ratio of Pt than previous models (refer to Fig. 5.10).

Decreasing the number of atoms and so is increasing the surface-to-volume ratio for Pt layers do not change the failure mechanism of the NC, which can be seen from Fig. 5.11. Another way of explaining this disparity might also be explained by the length of inter-atomic bonds. The distance between carbon atoms in a graphene sheet is almost 1.42 Å, and this number for platinum atoms is 3.9239 Å. A longer bond distance for Pt may result in the possibility of stretching more than graphene. As a result, during bending, the Pt

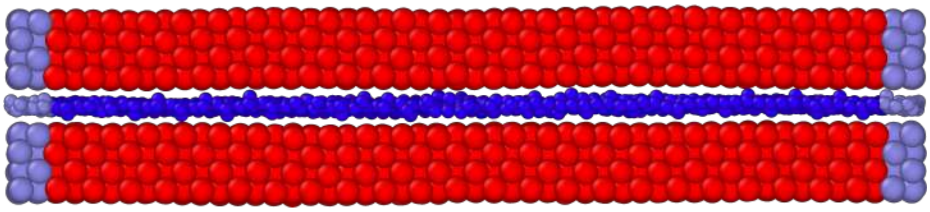

Figure 5.10: NC with more surface-to-volume ratio for platinum layers.

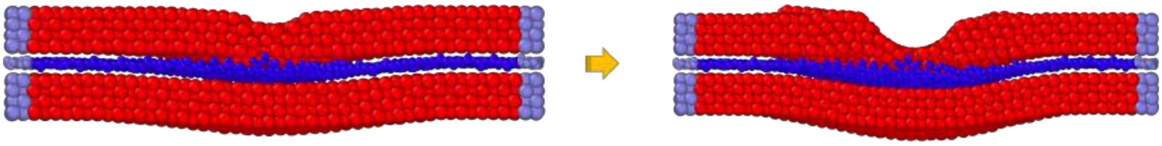

Figure 5.11: Failure of Pt-Gr NC where Pt has higher surface-to-volume ratio than previous models.

layer stretches more than the Gr layer, causing the upper Pt layer to fail before any significant mark is made on the graphene layer. Also, Gr has superior mechanical properties than Pt which also supports the possibility of failure of the Pt layer beforehand. In the next subsection, I will describe briefly about the effect of increment of Gr layers.

5.3.3 Effect of Number of Graphene Layers

Different bending load simulation has been done in this study to investigate the effects on mechanical properties due to the number of Gr layers in the NC. Simulations were done on NC having Gr layers from one to five. A graph (Fig. 5.12) containing force-deflection curves of different layered Pt-Gr NC is shown below.

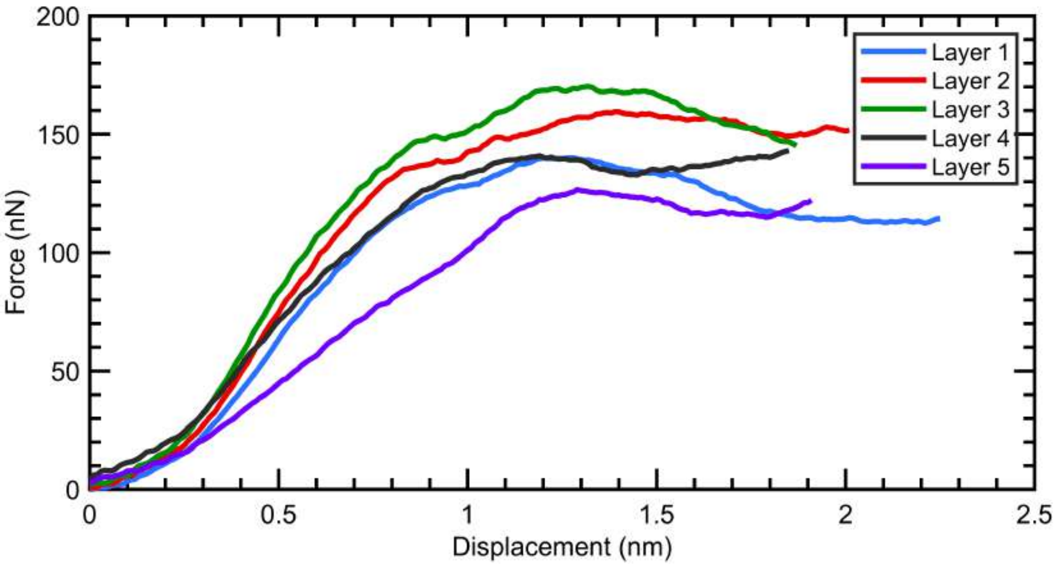

Figure 5.12: Force-deflection curve of different Gr layers NC.

The F-d curves show a nonlinear trend here. In general, for short NWs, a linear-elastic F–d curve is often created, but a nonlinear-elastic F–d curve is generated for long NWs. The nonlinearity grows as the length of NW increases [105].

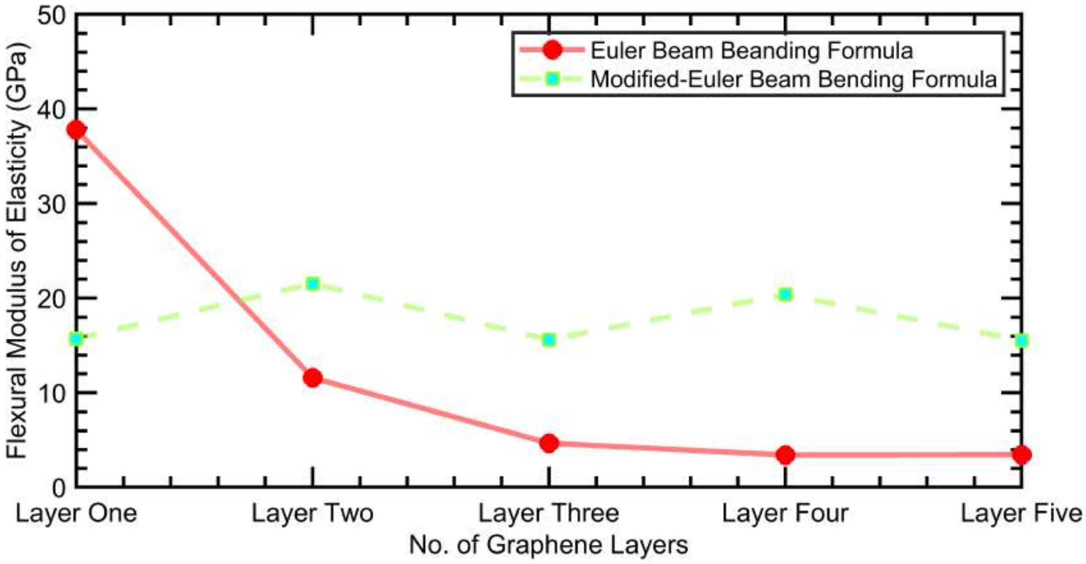

Figure 5.13: Comparison of E values of the NC under bending load.

Fig. 5.13 plots the possible estimation of E by both Euler beam bending formula (Eq. 5.18) and Modified-Euler beam benging formula (Eq. 5.20). Accordingly, the modulus values in Eq. (5.20) seem to be less than those in Eq. (5.18). This conclusion is acceptable given that the force of stretching increases its stiffness [102]. Therefore, using Eq. (5.20) to match the MD data would result in a reduced Young's modulus. Also, a parabolic decrement trend is observed using Eq. 5.18 whereas Eq. 5.20 yields almost equal value of E for different layers of Gr which is more preferable as failure mechanism due to bending is almost similar for any no. of layers of Gr.

5.4 Section Summary

Accordingly, an MD bending simulation model was developed, informed by the AFM-bending tests, that can adequately represent the mechanical characteristics of NCs in an clamped-clamped beam setting. We analyze and compare the MD findings with those from the traditional Euler-Bernoulli beam theory, both with and without the axial effect. Estimates of the Young's modulus from bending and tensile deformation are compared. Summary of key findings:

- Young's modulus of a NC due to tensile and bending test should be almost similar. But in this study, Pt-Gr NC shows some discrepancy by having a smaller value of E due to bending.
- Surface-to-volume ratio plays an insignificant role for flexural strength of this selected NC.
- Interatomic bond length could be the reason for difference in stretchability of different layers in Pt-Gr NC. Having lower bond length might lead towards more resistant in bond stretching that makes more easily stretchable bonds of Pt to fail earlier.
- Mechanical strength of NCs for any no. of Gr layers remains almost similar which is verified by Modified-Euler beam bending formula. On the other hand, Euler's beam bending formula gives a parabolic decrement pattern of E.

Chapter 6

Tribological Properties: Friction

The pencil was an essential instrument for learning and expression when we were young. The graphite lead of the pencil let the graphite atoms stick to the paper, by which we could express our writing or drawing on a sheet of paper. Friction between the paper and graphite lead is thought to be the cause underlying this phenomenon. This kind of simple tribological phenomenon has been an integral part of our lives from a very early age. The Greek word 'tribos' means rubbing. In spite of the fact that "the science of rubbing" is what tribology really means, in the Jost Report, Adoption of a lengthier, slightly less satisfactory definition: "The science and technology of interacting surfaces in relative motion and of associated subjects and practices" [3].

Frictional forces, which work in opposition to motion, are created at the points where two materials come into touch with one another during motion. Evaluation of frictional force and its effect on any material is of great importance. In this chapter, I will discuss about the studies I have conducted on the Pt-Gr NC for frictional force.

6.1 Theoretical Background

6.1.1 Historical Overview

The history of humankind has been considerate about friction and its effect. From the first fire, rubbing stones, to modern day construction, friction is everywhere. Though the effect of friction has been known to people for a while, the first attempt to document it was made by Leonardo da Vinci through some experimentation. From his records, remarks can be found as follows [1, 107]:

- The friction force between two sliding surfaces is proportional to the applied load used to press the surfaces.

- The friction force has no dependence on the apparent contact area between the surfaces.

The first two rules were rediscovered by Amontons which are known as Amontons' laws of friction, and they were initially published in 1699 in the Proceedings of the French Royal Academy of Sciences by Guillaume Amontons (1663-1705) [108].

Table 6.1: Three Laws of Friction

First law of friction	The friction force is proportional to the normal load.
Second law of friction	The friction force is independent of the apparent area of contact.
Third law of friction	Kinetic friction is independent of sliding velocity.

Eighty years later, Coulomb (1736-1806) established the third law, sometimes known as Coulomb's law of friction, which states that kinetic friction has a weak dependency on velocity. Although Leonardo da Vinci stated the first two laws for friction even before Amontons, these are regarded as Amontons law as he was the first to publish [3].

6.1.2 Macroscopic Considerations

Amontons, like many friction researchers, saw that the surfaces he dealt with were not perfectly smooth, and he assumed that roughness was perhaps accountable for friction. He presented two methods: (1) For stiff asperities, friction was caused by the force required to lift the weight up the surface roughness' slopes. (2) For deformable asperities, the asperities behave as flexible springs that are deformed during sliding, causing friction to rise according to the degree of deflection.

6.1.2.1 Static Friction and Steady Sliding

Consider a scenario in which a block with a spring connected is pushed at a constant velocity with no change in normal force. Beginning the procedure, the block remains stationary until the maximum static friction force is reached. Typically, we consider static friction to be a constant number, but in reality, the friction force increases linearly as the spring is loaded. This behavior is seen in Fig. 6.1, where the friction force reaches its maximum value before decreasing somewhat and settling into a continuous sliding motion [2, 3].

6.1.2.2 Stick-Slip condition

During the transition from sticking to slipping, friction exhibits the behavior seen in Fig. 6.2, with consecutive halt in motion followed by a slide. This is the result of the static

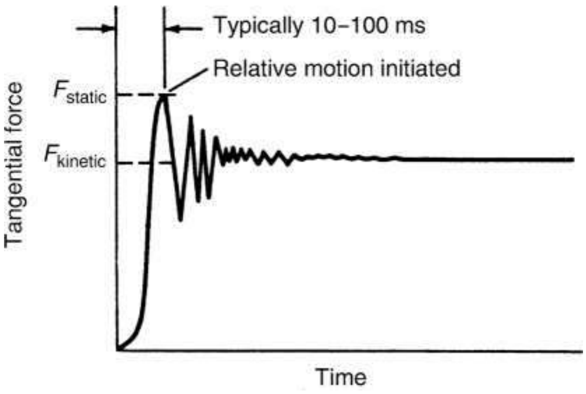

Figure 6.1: Tangential force is a function of time or displacement; F_{static} is the static friction force necessary to begin motion, and $F_{kinetic}$ is the kinetic friction force necessary to maintain motion [2].

friction being greater than the kinetic friction and the fact that the kinetic friction reduces as sliding speed increases (remember that the third law of friction is just a good approximation) [3]. For an atomistic explanation for the stick-slip phenomena, one can refer to the later section.

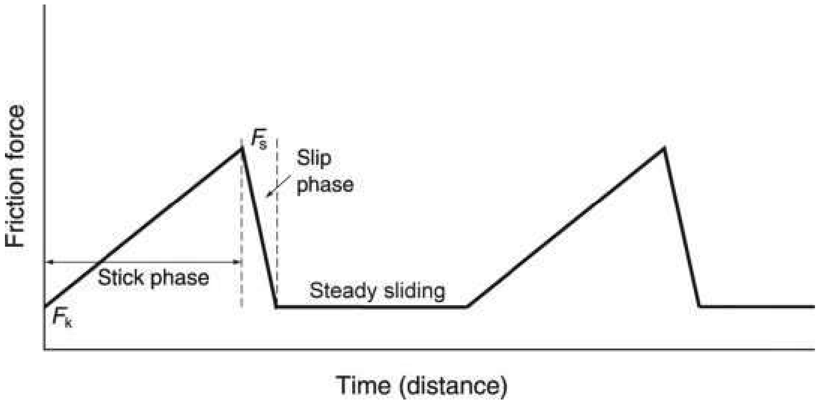

Figure 6.2: Stick-Slip condition [2].

During the stick-slip, for the identical block described before, the block remains stationary until the static friction force is reached, at which point it begins to move. After crossing the equilibrium position of the spring, the velocity gradually decreases until it abruptly stops. The combination of the spring's draw velocity and spring stiffness dictates whether the motion will be of a steady or stick-slip character (if these values are sufficiently high, the steady motion will occur) [2, 3].

6.1.3 Atomistic Origin of Friction

When Amontons first suggested his friction laws in 1699, many, including Amontons himself, believed that friction resulted from the interlocking roughness of opposing surfaces.

With the middle of the twentieth century, however, this roughness mechanism had been ruled out and replaced by the belief that the two most important factors to friction are surface roughness and surface lubrication. These initial ideas of friction give rise to two mechanisms [3]:

1. Adhesion force, the attraction between objects with different shapes or textures.
2. Plowing force, need to plow through the abrasions of the tougher surface with the softer surface.

6.1.3.1 Adhesion and Plowing force in friction

Adhesion Friction

When two surfaces come into contact, the contacting asperities undergo elastic and plastic deformation. At the site of contact, a tiny contact area A_i is created where surface atoms are in close proximity, hence creating attractive and repulsive interatomic interactions. Shear stress is produced when tangential force is applied to cause objects to slide across one another. Atoms begin to slide over one another when the applied force acting on them surpasses the total of all the interatomic forces attempting to retain them in their places, which happens at a certain shear stress [3]. The required force needed to shear the contact is, $F_i = A_i s$, where s is the shear stress.

If we assume all the contacting area has the same shearing stress, then the adhesive force is, $F_{adh} = A_r s$, where $A_r = \sum A_i$.

When interactions across the sliding interface are relatively weak, causing the contact pressure from the externally supplied load to be equivalent to the internal pressure from adhesive forces, a notable linear dependency of shear strength with contact pressure is generally seen. Despite the constant contact area, Amontons' rule that friction is proportional to load seems to hold true in these circumstances [109, 110].

Plowing Friction

Plowing friction, F_{plow}, is the contribution to friction force made by hard asperities plowing through a softer surface [3]. Multiplying the total projected area A_o in the direction of motion of the contacting asperities by the pressure required to initiate plastic flow in the softer material yields a straightforward calculation of F_{plow} (approximately, its hardness H): $F_{plow} \approx A_o H$.

6.1.3.2 Atomistic model for Static Friction: Tomlinson model

Prandtl (Prandtl 1928) and Tomlinson (1929) devised a considerably simpler and primitive model for friction that is often known as the Tomlinson model or the independent oscillator model. In Fig. 6.3, a one-dimensional Tomlinson model is shown.

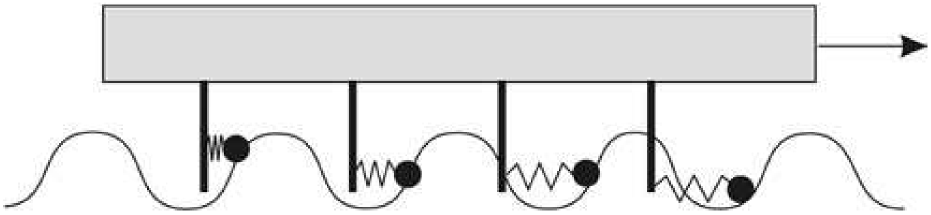

Figure 6.3: One dimensional Tomlinson model in which atoms are linked to one other by overdamped springs and experience a periodic potential as they slide over a substrate surface [3].

The initial setup of the system is one with the least potential energy. When the slider begins to move, the system shows static friction until sufficient elastic stress is generated in the springs to overcome potential barriers, at which time the atoms swiftly make transition to their next stable state. During these pops or slides, elastic energy is transformed into kinetic energy, which is then released as heat (this dissipation process is incorporated into the model as the damping constant for the spring-atom oscillators).

If the height of the potential barrier is decreased below the slip threshold, the atoms pass smoothly across the potential. If, in this situation of smooth sliding, these atoms are likewise disproportional to the substrate, the lateral forces acting on the individual atoms will cancel out, resulting in little net friction.

6.1.3.3 Atomistic model for Kinetic Friction

Static friction refers to the force required to overcome the potential energy barriers between atoms, initiating sliding, whereas kinetic friction refers to the dissipative energy processes when atoms slide over each other [3]. When the surface is smooth enough, just a tiny amount of force is required to initiate the sliding. We may safely assume that the force F acting counter to motion is completely viscous.

$$F = m\eta_m v \tag{6.1}$$

where v is the sliding velocity, m is the molecular mass, and η_m is the viscosity of the interface between the two moving bodies. Generally speaking, phonon excitations (sliding-induced atomic vibrations) are the principal cause of the viscous damping, and these excitations are ultimately turned into heat. In analytical models of noble gas adsorptive sliding on surfaces, the atom-substrate interaction is described using a periodic potential with corrugation U_0. The following correlation characterizes η_m:

$$\eta_m = \eta_{subs} + cU_0^2 \tag{6.2}$$

where η_{subs} is the dissipation of energy other than phonons (such as electronic excitations) and c is a constant that varies with both temperature and lattice spacing. Keeping in mind once again that the adsorbed layers encounter only viscous friction while sliding (Eq. 6.1) and are therefore modelable in terms of a slip time,

$$t_{slip} = \frac{1}{\eta_m}, \tag{6.3}$$

where t_{slip} is the time it takes for the adsorbed layer's velocity to drop by 1/e, allowing driving force F to be removed, and η_m is the inverse of this constant [3].

6.2 Simulation Methodology: Friction

The system of simulation is comprised of two bodies, (a) Pt-Gr NC slab and, (b) a probe curved out of a diamond block. Both the bodies are merged together into a system after prepared separately by leaving a clearance of about 1.0 nm in between. The whole system was designed using atomsk [48]. The system interacted with each other using interatomic potentials. For Pt-Pt, uantum cqorrected Sutton-Chen potential [59] is used, Stillinger-Weber potential [52] is used for intercommunication between graphene molecules i.e. Carbon molecules and Morse potential is used for Pt-Gr interaction. All the simulations has been done in LAMMPS [91]. The following sections are consisted of in details simulation process with codes where required.

6.2.1 Slab Construction

The previously designed Pt-Gr NC system is used as the slab for this simulation. Double layered Pt-Gr NC is taken for all of the friction simulations. Since friction is a surface phenomenon, increasing Graphene layers does not have any significant impact on the results. Therefore, to keep the simulation simple, double layered NC was chosen .

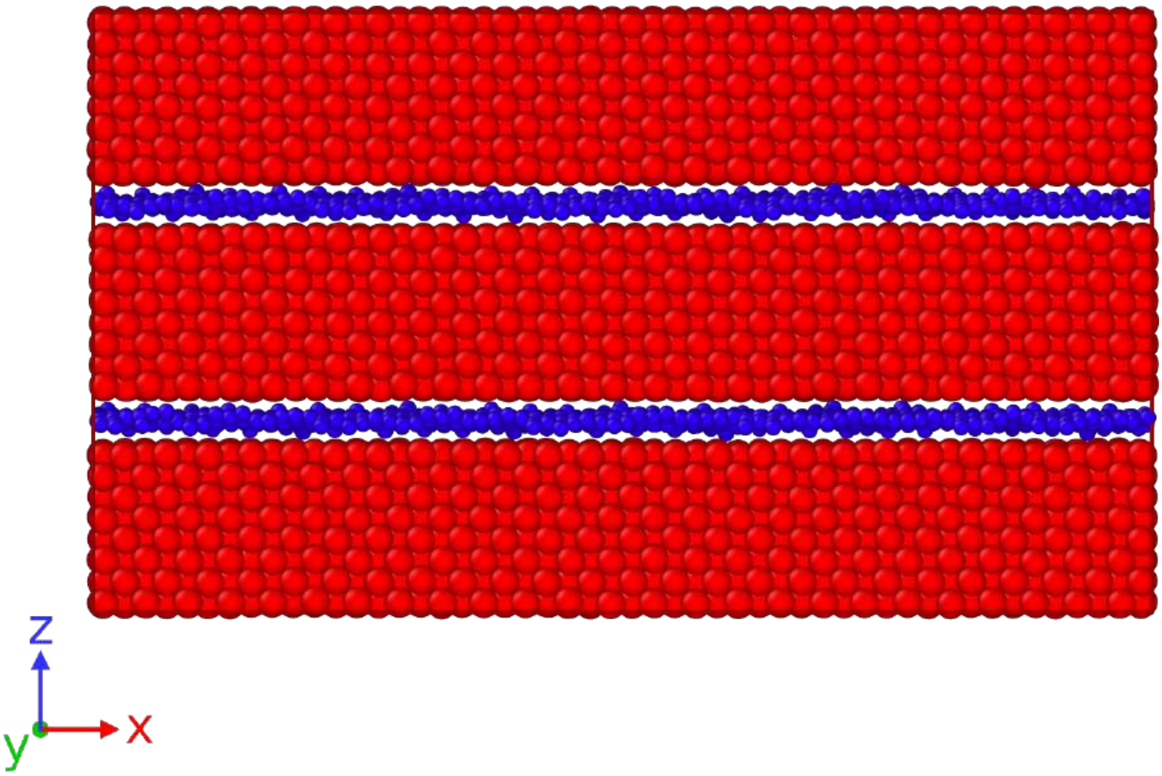

Figure 6.4: NC slab used for friction simulation

6.2.2 Probe Construction

A probe was used in this friction simulation to slide over the slab. Firstly, a diamond block was created using atomsk [48]. Afterwards a cube of 2.142 nm X 2.142 nm X 2.142 nm was curved out of the block which was merged with the slab to complete the system. The system was then converted into lmp file so that it can be used in LAMMPS

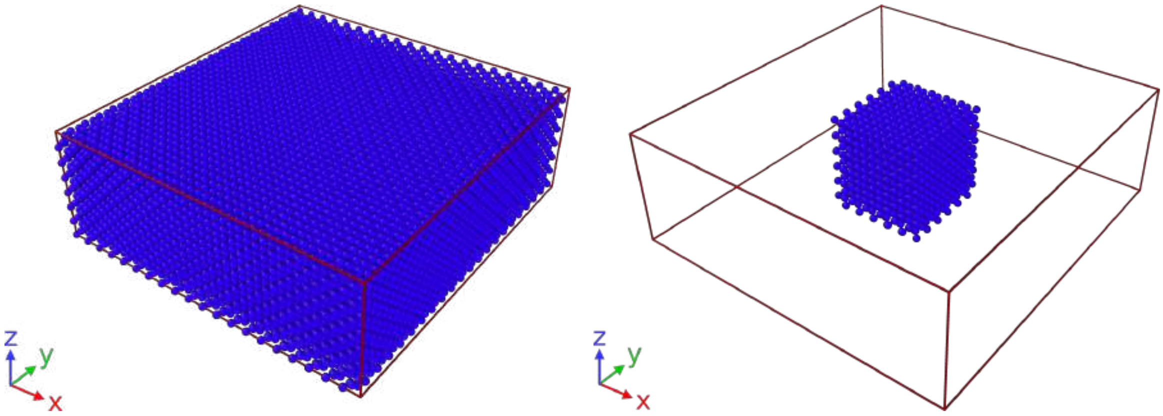

(a) Diamond block

(b) Diamond probe

Figure 6.5: Construction of Diamond probe curved out of a Diamond block

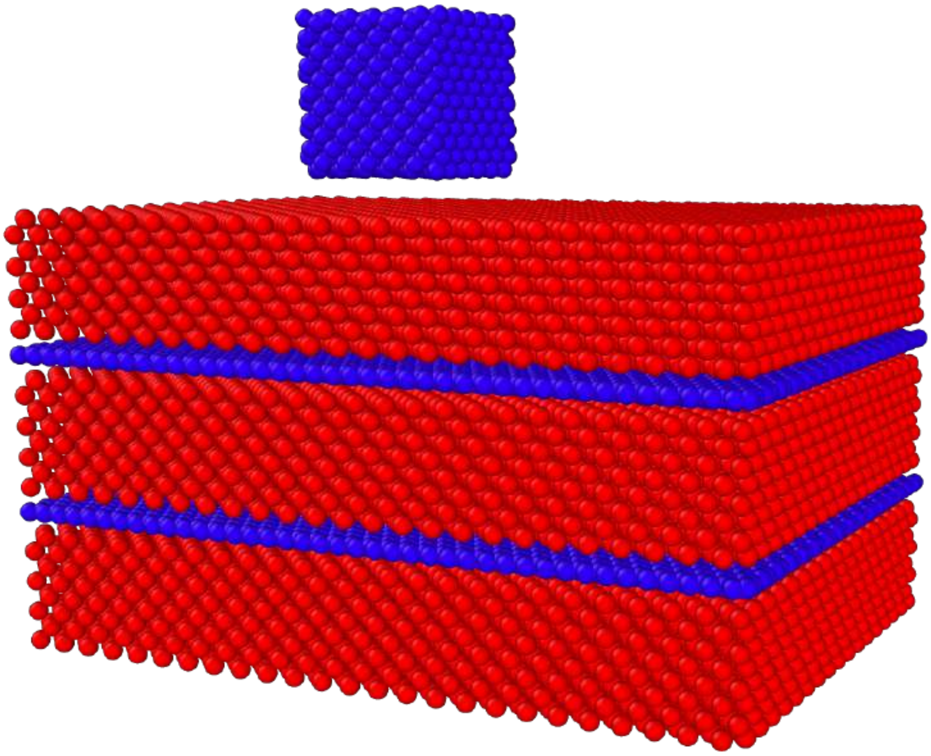

Figure 6.6: System of Slab-Probe for friction simulation

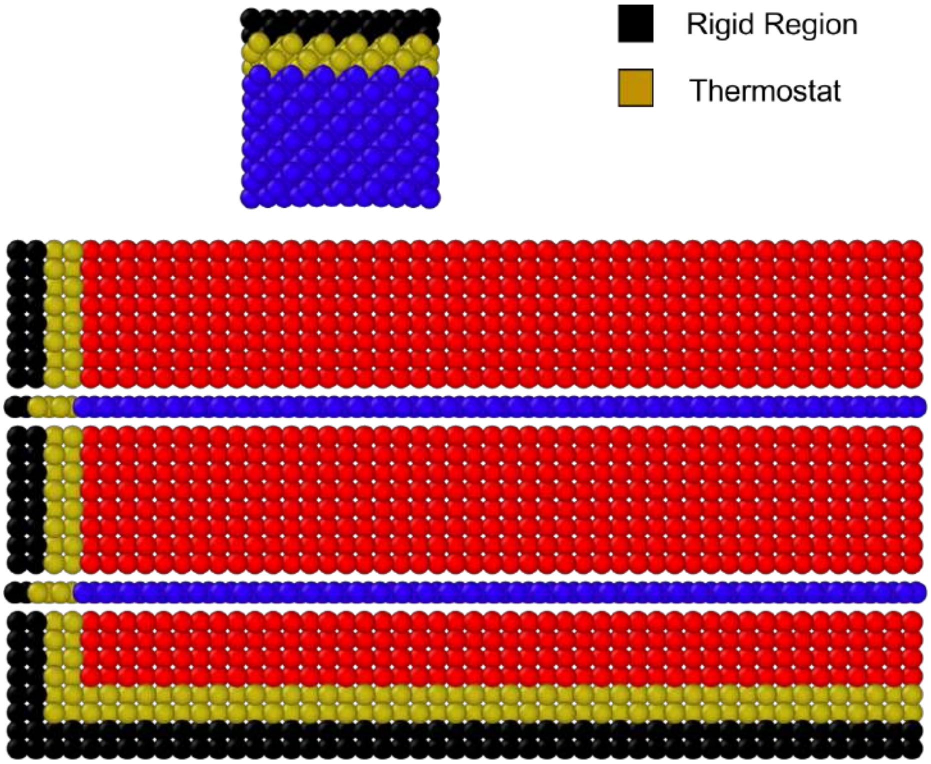

Figure 6.7: Simulated system with distinct regions.

6.2.3 Simulated System

The slab was divided into three distinct regions [4]:

1. Rigid layers - two layers at the bottom and far left regard as rigid layers which is used for energy dissipation.
2. Thermostat - two layers at the top and right of the rigid layers is regarded as thermostat. These layers are fulfilling the purpose of temperature controlling where temperature is controlled through NVT ensemble.
3. Simulated region - all the other regions except rigid layers and thermostat are the simulated region where NVE ensemble is employed.

The computational cost of the MD simulations was kept within realistic bounds by selecting the size of the periodic cell and the number of atomic planes in each of the aforementioned three layers, allowing for the tracking of the system's dynamics for up to 120 ps. The probe block has three different areas, much like a mirrored sample slab.

6.2.3.1 Temperature Control

In most cases, when MD simulations are used to study atomic friction, the thermostat is not applied in the contact region [111]. This is done to prevent any changes in the dynamics of the area that is being examined. Both the tip and the substrate have the thermostat placed in layers that are located far apart from the surfaces. This allows for efficient heat dissipation [4]. Because this experiment required a thermal bath for the system, we employed a Nose-Hoover thermostat with a friction factor of 0.5 ps to maintain a temperature of 150 kelvin throughout the NVT areas present in both the tip and the substrate.

The coupling to the NVT regions allowed us to carry out the MD simulations at 150 K, with the exception of a few tests that were performed at different temperatures to evaluate the influence of temperature on the simulations with varying surface coverage. These tests were performed in order to evaluate the influence of temperature on the simulations. At these low temperatures, the relaxation of the simulated diamond surfaces is severely hampered. Since there is no surface reconstruction taking place, the impact on friction of the various surface alterations that were investigated here should be greatly amplified [112]. After deducting the center-of-mass velocity of the group, the compute temp/com command was executed in order to compute the temperature of all of the dynamic atoms on the system (the fixed atoms were excluded from this calculation).

6.2.3.2 Application of Normal Load

The normal force in MD simulations of friction may be supplied to the superior atoms of the tip, which are often regarded as a rigid body, or it can be imposed by setting a fixed distance between the tip and the substrate [4]. Fig. 6.8 illustrates a uniform z-direction force is supplied to the probe's top hard layer of atoms (considered a better alternative than imposing a constant distance between the tip and substrate). A spring with various spring constant ranging from $k_z = 1eV\AA^{-2}$ to $k_z = 15eV\AA^{-2}$ was taken for various normal loads.

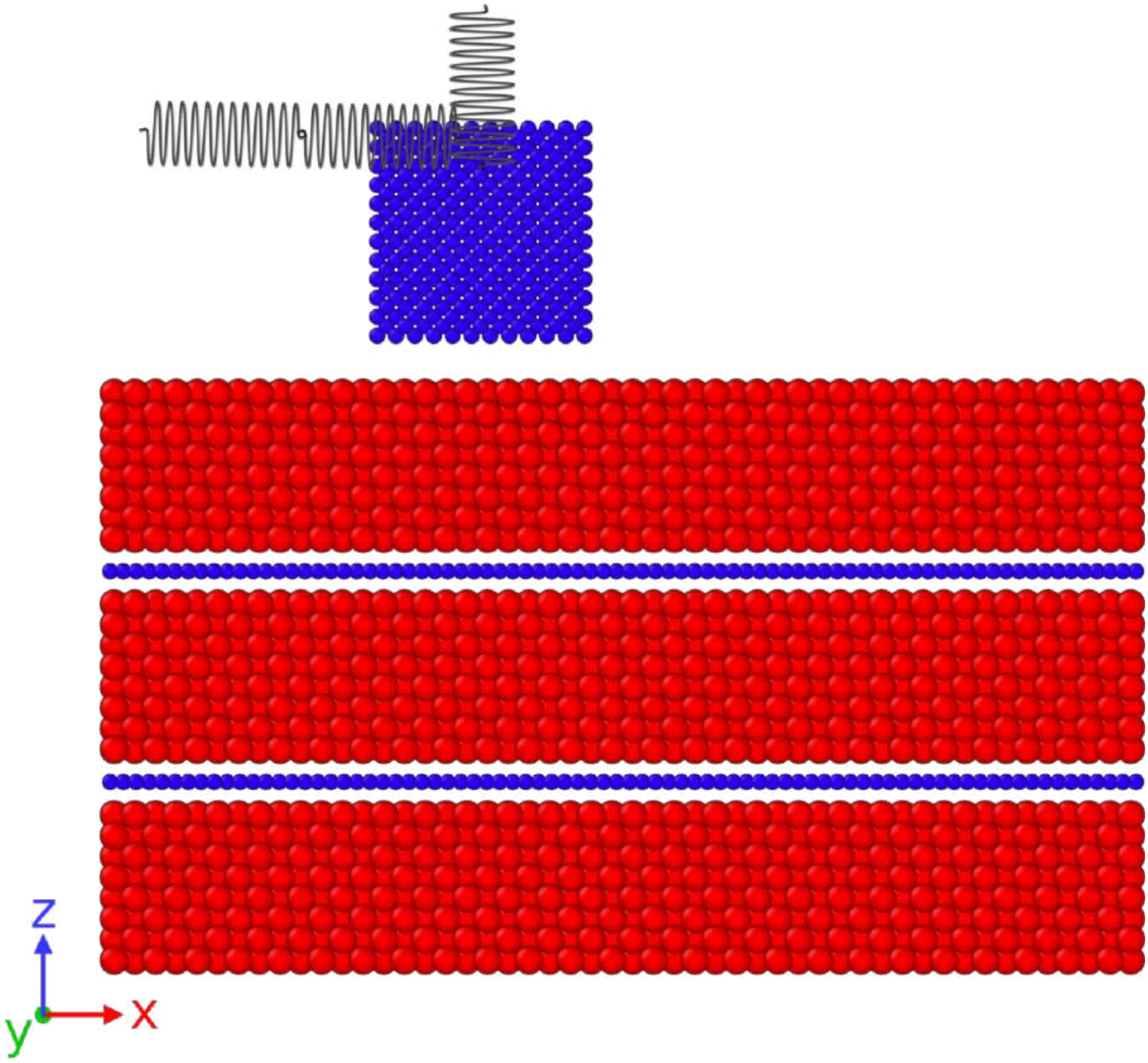

Figure 6.8: Schematic representation of the probe and slab. Two springs maintain the probe's connection to the anchor. (Left and top)

6.2.3.3 Lateral Force

Between the probe's mass-center and tether point, a massless spring with a force constant of $k_m = 3eV\AA^{-2}$ [112] was connected in the probe's stiff atoms. In this case, just the x-components of deformations of the spring produce a force (the spring is free to move without resistance on the yz-plane). The value of k_m may be defined in two ways: either by setting $k_m x$ to the same value as the cantilever, or by specifying the stiffness to be the same as the effective experimental stiffness, which is a more precise approach. One alternative is to directly adjust the spring's stiffness until the desired effective stiffness is reached [4]. As spring stiffness rises, the greatest lateral forces obtained drop in magnitude as the average value decreases [113]. An increase in the frequency of the instantaneous friction force oscillations was seen in experiments where a spring with a higher spring constant was connected to the probe. With increasing spring constants, the spacing between the potential energy's peaks coincides with the periodicity of the instantaneous friction force [112].

6.2.3.4 The Dynamics

Unlike the tensile testing, the system is kept at periodic boundary condition only in the X and Y directions, with the Z direction set as non-periodic shrink wrapped with a minimum value, m, condition. At the beginning of the MD simulation, the whole system was minimized using the conjugate gradient method by minimizing the energy. An absence of minimization will allow for the possibility of huge dynamic movements, which will result in an incorrect interpretation of the data. The relaxation was done while keeping the probe at a distance of 1.0 nm from the slab. Afterwards, the probe was permitted to reach towards the slab surface by applying a constant normal load to it, and the system was let to equilibrate for 100000 steps, with each step being 1 fs. Then, the rigid layer of the slab is given a value of 1 $\AA/ps^{-1}$ to move in the negative X direction. It is permitted for the system to spontaneously evolve until it reaches a steady state. When the system has reached its steady-state regime, the production phase will commence and will continue for some ps in order to collect data of at least four cycles of the friction force. In all, each simulation consisted of 120000 discrete time steps.

6.2.3.5 Data Analysis

All of the data is analyzed using Matlab and python. As will be shown in the next section, the instantaneous friction force demonstrates periodic oscillations, which may or may not be well characterized depending on the circumstances that are being simulated. As a consequence, the instantaneous lateral force was time-averaged across each cycle of force oscillation, and the overall friction force was acquired as the average of the set of averages that was computed for each entire cycle. The friction coefficient may be calculated by finding the slope of the straight line that best fits the data on the relationship between the friction force and the normal force.

6.3 Parametric Study

6.3.1 Steps of analysis

The MD simulations conducted here for the friction case generates various data to be analyzed for further results. The basic codes in the LAMMPS [91] input file for friction is presented below:

Listing 6.1: Input file for friction simulation

```
% THE UPPER REGION OF THE TIP IS RIGID

fix           rigidFix tipF rigid single force 1 on off on
              torque 1 off off off
fix           rigidForce tipF addforce 0.0 0.0 ${F_normal}

% APPLYING DIFFERENT THERMOSTATS FOR DIFFERENT REGIONS
fix           3 nveTip nve
fix           4 nveSlab nve
fix           5 nvtTip nvt temp ${T} ${T} 0.5
fix_modify    5 temp temp_dinamico
fix           6 nvtSlab nvt temp ${T} ${T} 0.5
fix_modify    6 temp temp_dinamico

% LOWER REGION OF SLAB IS KEPT UNDER ZERO LOADING
fix           lo_fix fixLo setforce 0.0 0.0 0.0
fix           7 fixLo nve

% LOWER REGION OF SLAB PERMITTED TO MOVE AT -X DIRECTION
velocity      fixLo set -1.0 0.0 0.0
```

From the obtained data, instantaneous friction force, force along the x-direction on the tip due to sliding, and its corresponding sliding distance is plotted to observe the friction nature of the NC. It is evident from the Fig. 6.9 that the Pt-Gr NC is exhibiting stick-slip behavior due to the friction that is acting upon it. During the first phase, known as the stick phase, the molecules of the slab and the tip adhere to one another until their potential energies are at their maximum. Following that, the point slipped a short distance before reattaching itself to the surface. The progression is depicted in the Fig. 6.10 that follows.

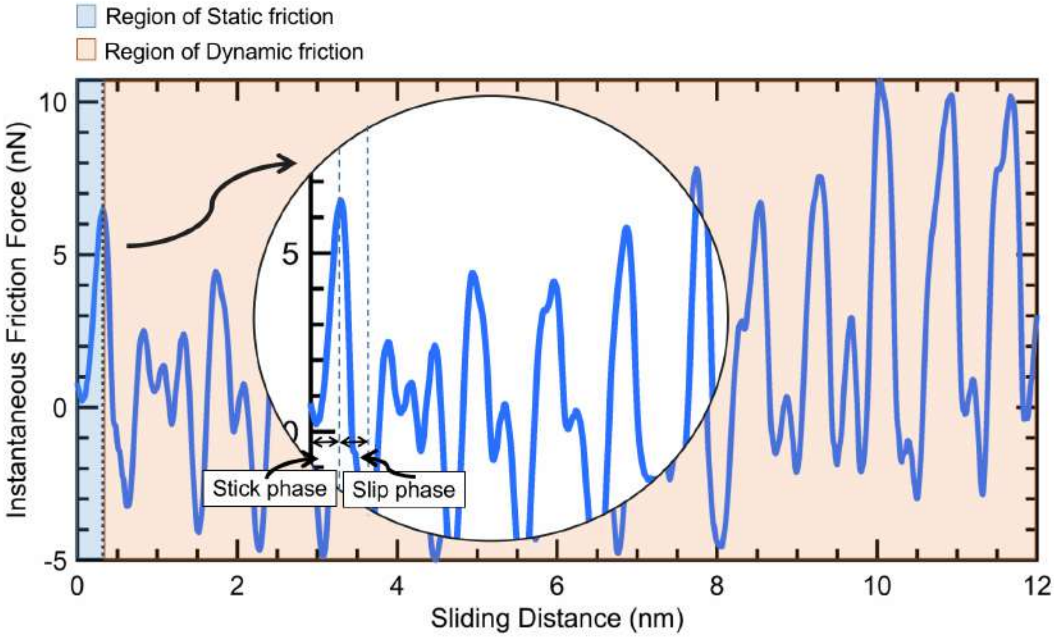

Figure 6.9: Stick-slip condition is verified from the MD simulations

Initially, for the selection of lateral or friction force, both the spring force and forces on the tip along the X-direction are plotted against the sliding distance. Referring to Fig. 6.11, it is evident that both values yield nearly the same result. Therefore, any of the forces may be chosen. For this analysis, the spring force has been chosen.

The MD simulation is carried out in steps that are sufficiently long to ensure that the system reaches a steady state. After the system has reached a point where it is sufficiently close to the steady state, at least four cycles of the stick-slip phase are chosen. Thereafter, each of the cycles is averaged, and finally, the friction force or lateral force is calculated by averaging all of the values that have been averaged for each cycle.

The normal or vertical load on the slab is calculated by averaging the vertical load on a slab over the sliding distance. Although a constant vertical load, mentioned in the sample input script by the F_normal variable, is applied on the tip, the slab experiences a fluctuation of vertical loading due to its movement in the sliding direction.

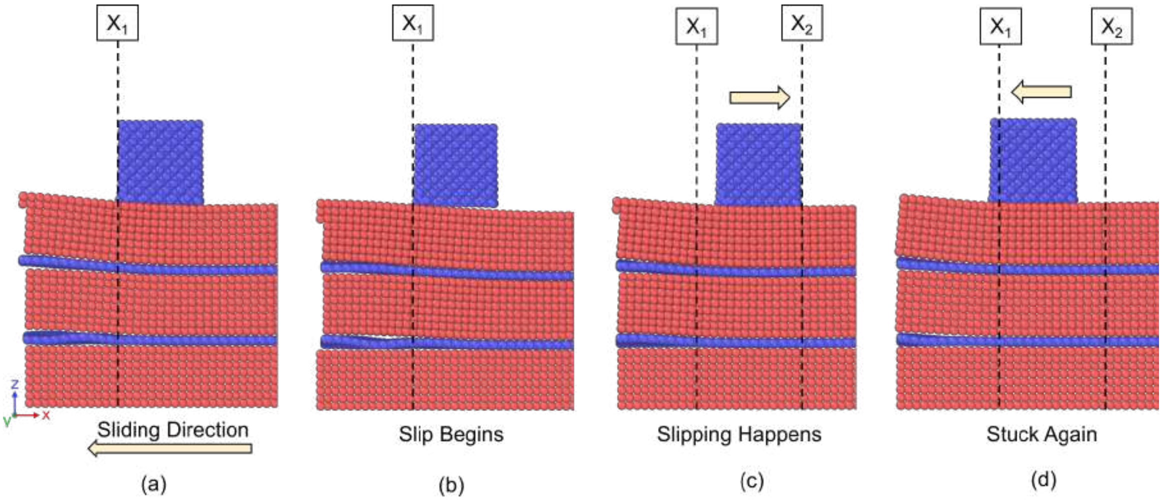

Figure 6.10: Evolution of stick-slip condition in Pt-Gr NC obtained from the MD simulation

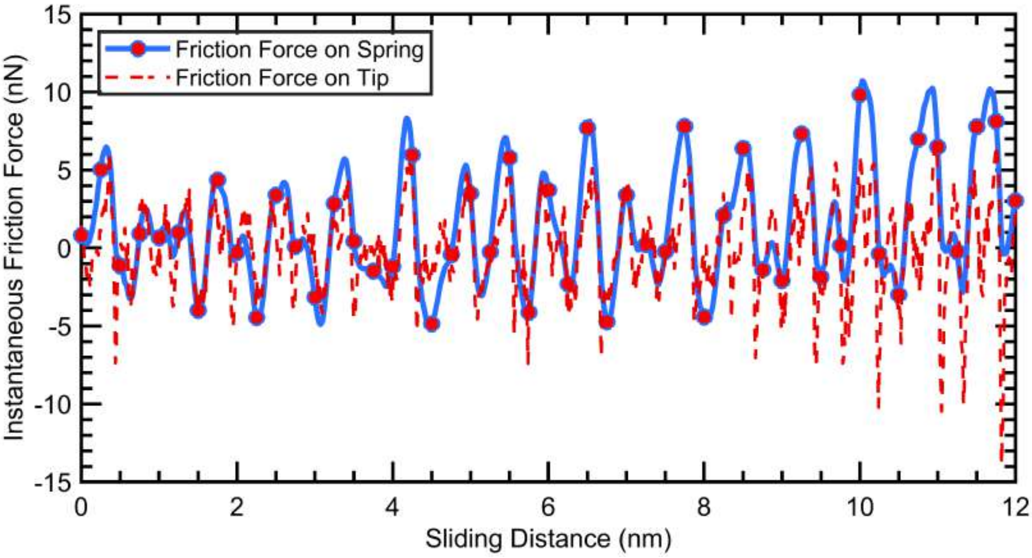

Figure 6.11: Instantaneous friction force vs Sliding ditance for NC at 150 K

Finally, these values, (a) lateral friction force and (b) normal or vertical fore are used to determine material's co-efficient of friction, μ. For this particular simulation of NC system at 150 K temperature, obtained friction force and normal force are 1.4274 nN and 9.6854 nN respectively. Therefore, $\mu = \frac{1.4274}{9.6854} = 0.14738$ for this Pt-Gr NC system at a temperature of 150 K.

A comparison between the COF for pristine Pt and Pt-Gr NC was also done for the same conditions of temperature, sliding velocity and vertical load of 150 K, 100 m/s and 10.5 MPa respectively. The obtained values are stored in the Table 6.2. By analyzing, it can be realized that the material of study, Pt-Gr NC, is more prone to hinder anything sliding over its surface than its pristine counterpart. This indicates that having a higher COF for Pt-Gr

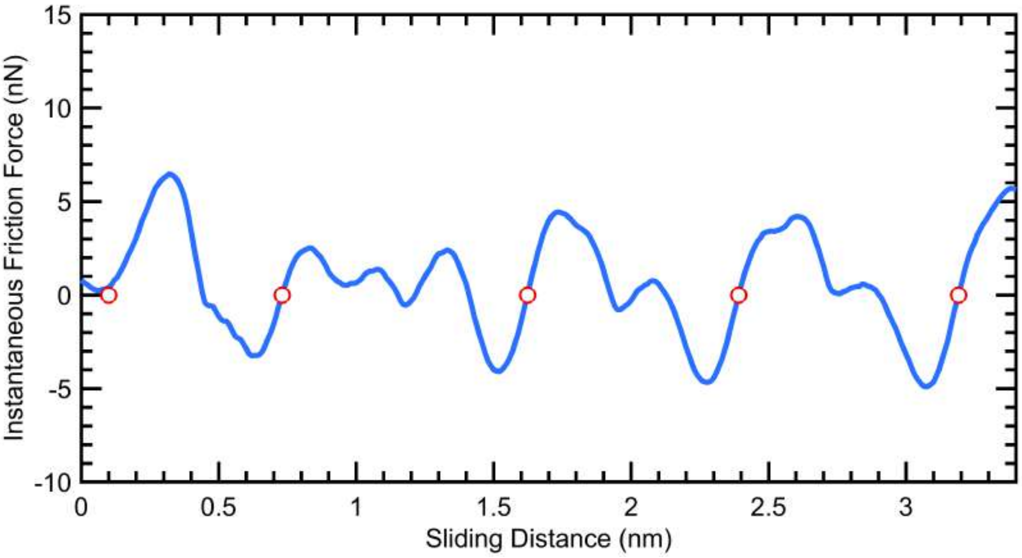

Figure 6.12: Four cylces chosen for analysis at 150 K

Table 6.2: Comparison of coefficient of friction between pristine Pt and Pt-Gr NC

COF for Pristine Pt	**COF for Pt-Gr NC**
$\frac{0.0475}{28.5621} = 0.0017$	$\frac{0.8976}{34} = 0.0264$

NC could be a better alternative in the application of Biosensors which requires sticking to the tissues in some cases.

6.3.2 Temperature Effect

The temperature, which reflects the thermal kinetic energy of constituent atoms, plays a crucial role in atomic friction. Recent developments in AFM capabilities have made it possible to measure friction at temperatures ranging from cryogenic to a few hundred Kelvin [4]. These recent experiments have revealed a number of intriguing patterns. The most widely acknowledged trend is that friction decreases as temperature increases [114–116].

To study the effect of temperature on the examined NC system, a series of simulations are done for different temperature. At a lower temperature of 10 K, the carbon molecules in the diamond tip goes through minimum surface reconstruction. [3] A simulation was done in this temperature. Apart from the base temperature of 150 K, some other temperature values of 10K, 300 K, 450 K, and 600 K were chosen to perform the study.

6.3.2.1 Temperature = 10 K

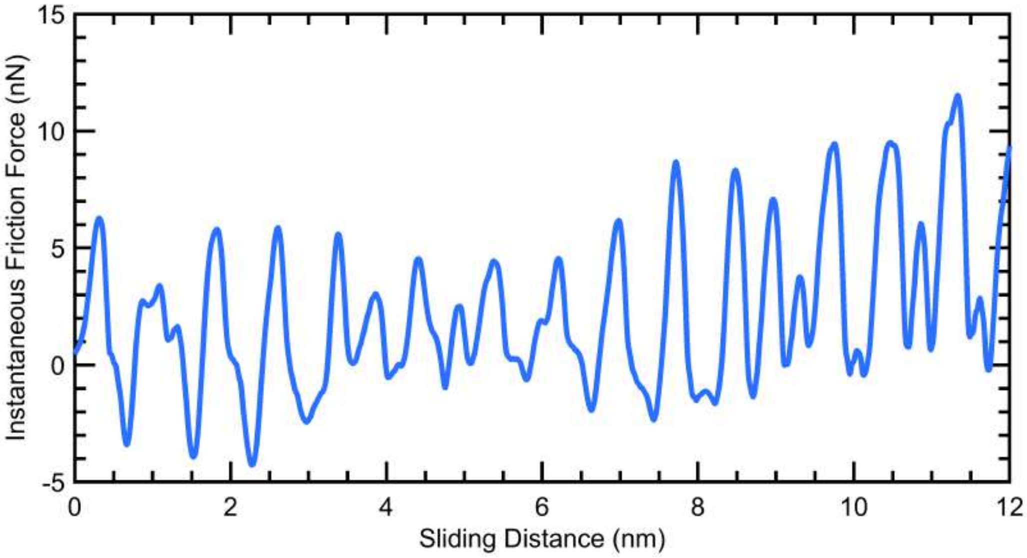

Figure 6.13: Instantaneous friction force vs. Sliding distance at 10 K

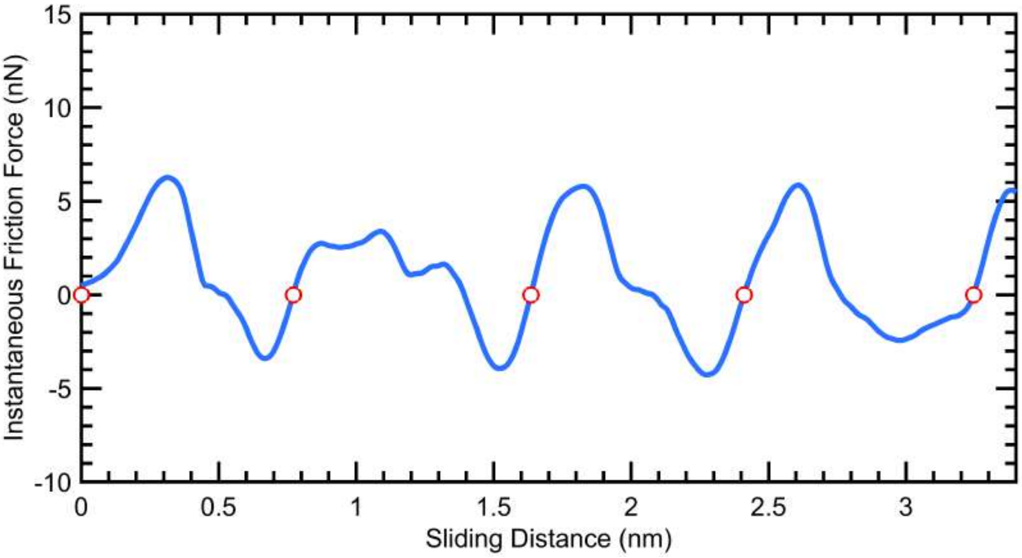

Figure 6.14: Four cylces chosen for analysis at 10 K

6.3.2.2 Temperature = 300 K

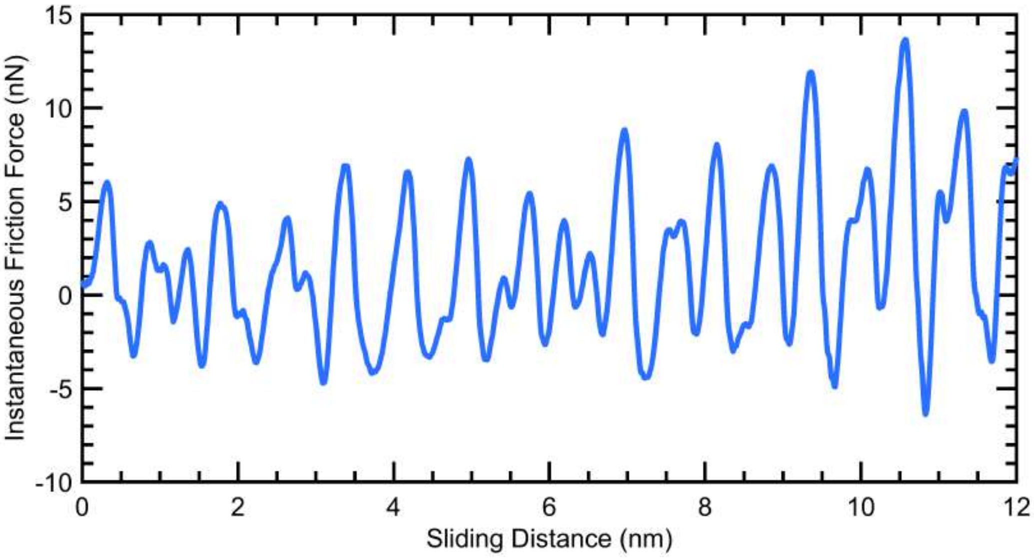

Figure 6.15: Instantaneous friction force vs. Sliding distance at 300 K

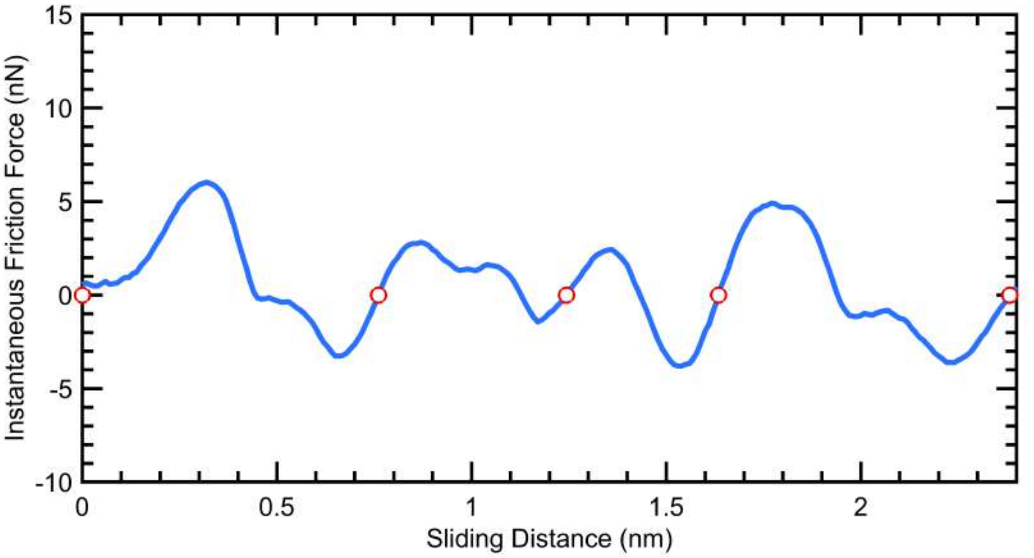

Figure 6.16: Four cylces chosen for analysis at 300 K

6.3.2.3 Temperature = 450 K

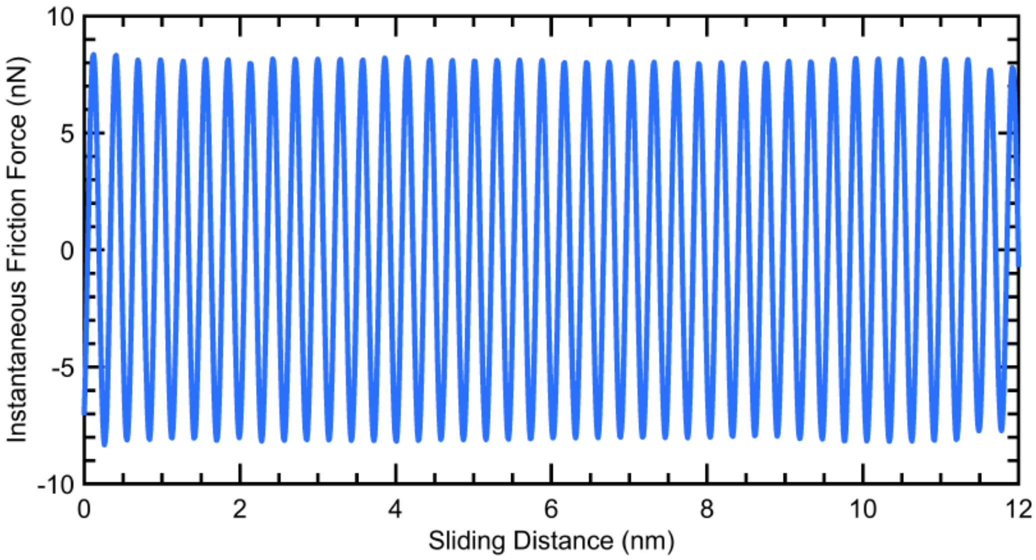

Figure 6.17: Instantaneous friction force vs. Sliding distance at 450 K

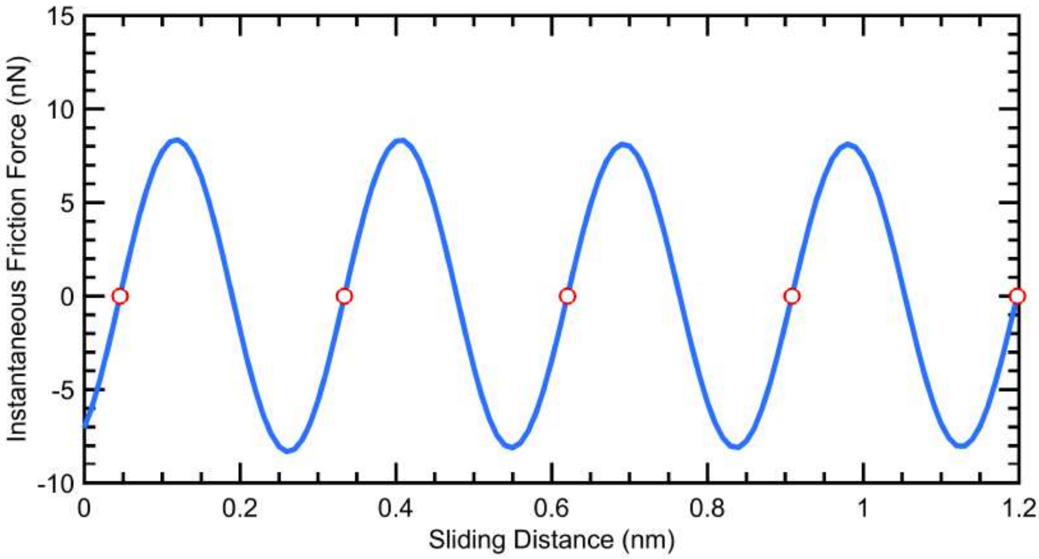

Figure 6.18: Four cylces chosen for analysis at 450 K

6.3.2.4 Temperature = 600 K

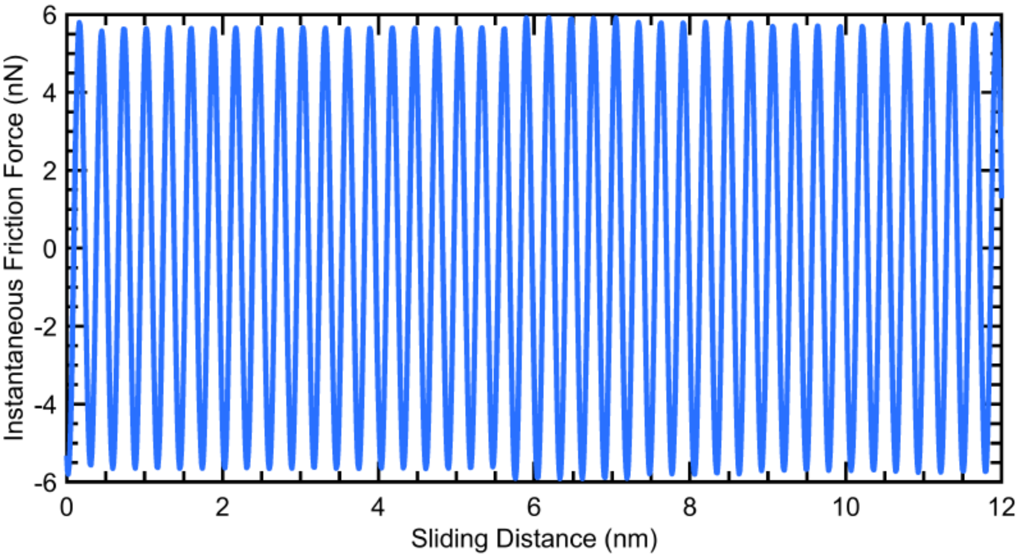

Figure 6.19: Instantaneous friction force vs. Sliding distance at 600 K

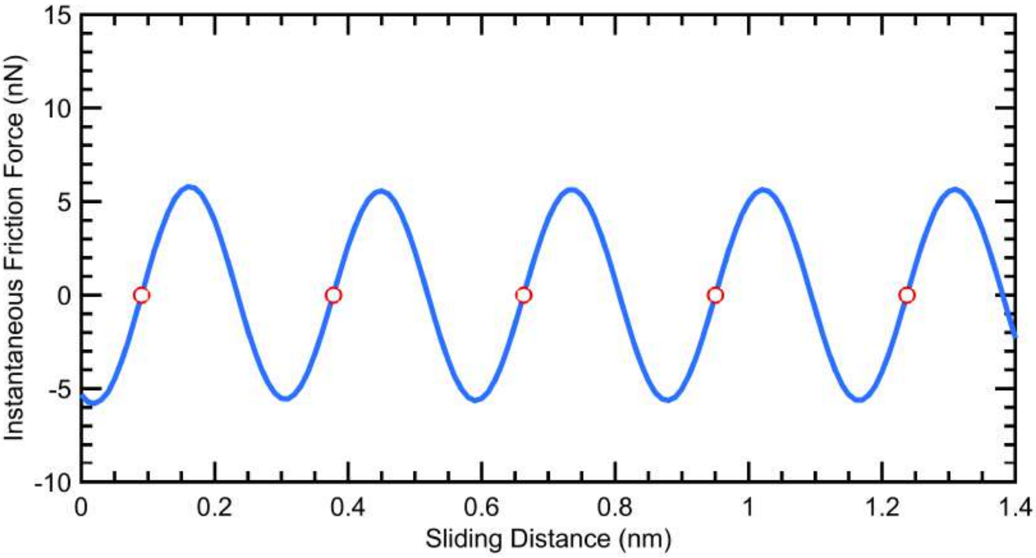

Figure 6.20: Four cylces chosen for analysis at 600 K

6.3.2.5 Temperature effect on friction coefficient

The results obtained from the simulations are put into a Table 6.3 after the analyses.

Table 6.3: Friction force and Normal force at different temperature for double layered Pt-Gr NC

Temperature (K)	Friction force, nN	Normal force, nN
10 K	0.8231	10.1953
150 K	0.4570	9.6854
300 K	0.5059	9.1827
450 K	0.2191	24.6206
600 K	0.1288	24.6329

To better comprehend the effect of temperature, the coefficient of friction is plotted against temperature. Fig. 6.21 reveals a downward trend, which is consistent with prior research [114–116].

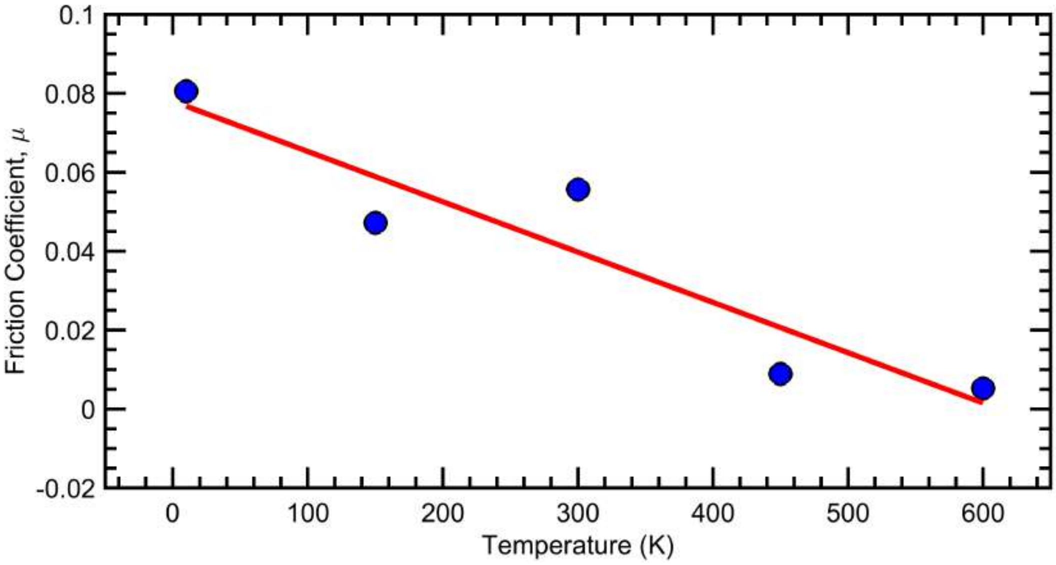

Figure 6.21: Coefficient of friction vs. Temperature

It is commonly believed that thermal activation decreases friction with increasing temperature [4]. Higher temperatures provide more thermal energy, allowing the tip to overcome energy barriers more quickly and reducing friction. In Prandlt-Tomlinson (PT) [117] model, the tip is viewed as a single atom ball dragged by a harmonic spring across a sinusoidal corrugation potential, which represents the interaction with the substrate, as depicted in Fig. 6.22. The system's total potential energy can then be expressed as:

$$V(x,t) = -\frac{U}{2}cos\left(\frac{2\pi x}{a}\right) + \frac{1}{2}k(vt-x)^2 \tag{6.4}$$

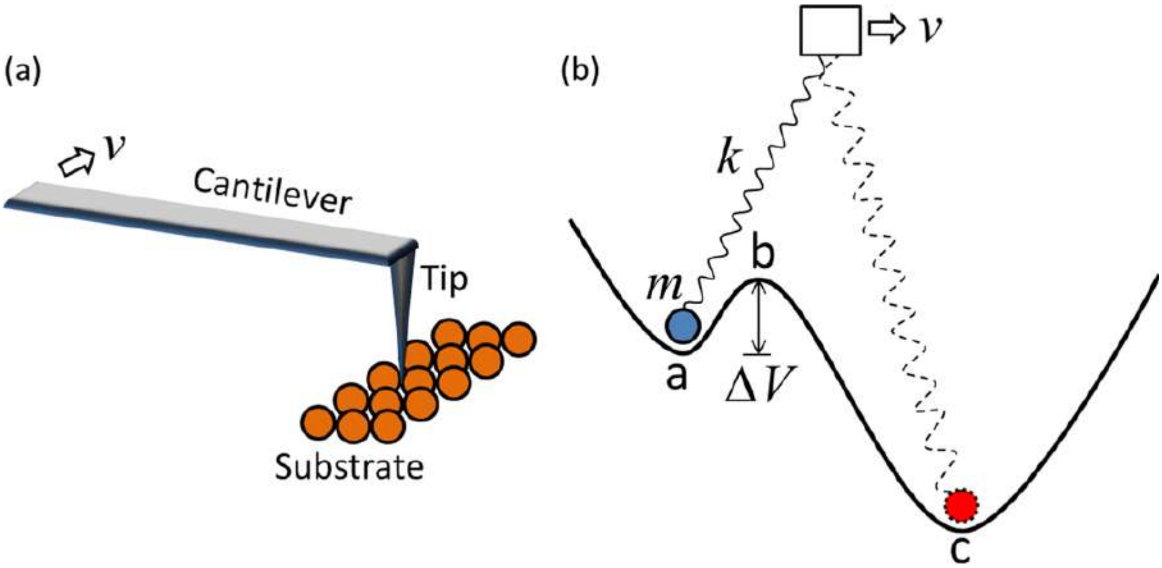

Figure 6.22: (a) a scanning probe microscope with a cantilevered probe head used to pull the tiptoe slide across a substrate, and (b) the corresponding PT model, in which the AFM system is reduced to a mass-spring system [4].

With the aid of thermal activation, the tip can cross the energy barrier between potential wells a and c more quickly, requiring less force (friction) to move forward.

In addition to thermal activation, additional mechanisms have been proposed to explain the various trends observed in AFM measurements. For instance, thermal activation theory does not account for the friction peak that arises in the low-temperature regime (around 50–200 K) [118–120]. To address this issue, it has been proposed that thermal activation not only aids in the rupture of bonds, but also in their formation; competition between the two causes the friction peak to occur at low temperatures. However, the notion of bond formation and rupture is still in its theoretical stage [120, 121].

6.3.3 Vertical Load Variation

According to classical contact mechanics, friction is proportional to the normal load through the contact region. As the load grows, so does the contact area [4]. The simulations carried out for the purpose of this research provide confirmation of this phenomenon. Fig. 6.23 displays a trendline depicting the relationship between normal load and friction force. The trendline is nearly linear, which is consistent with what was shown in the earlier research.

AFM measurements and MD simulations often reveal that friction rises with normal load. However, the precise nature of this growth remains contentious: Reportedly, friction increases linearly with load [122, 123], increases faster than linearly with load, and has a sublinear relationship.

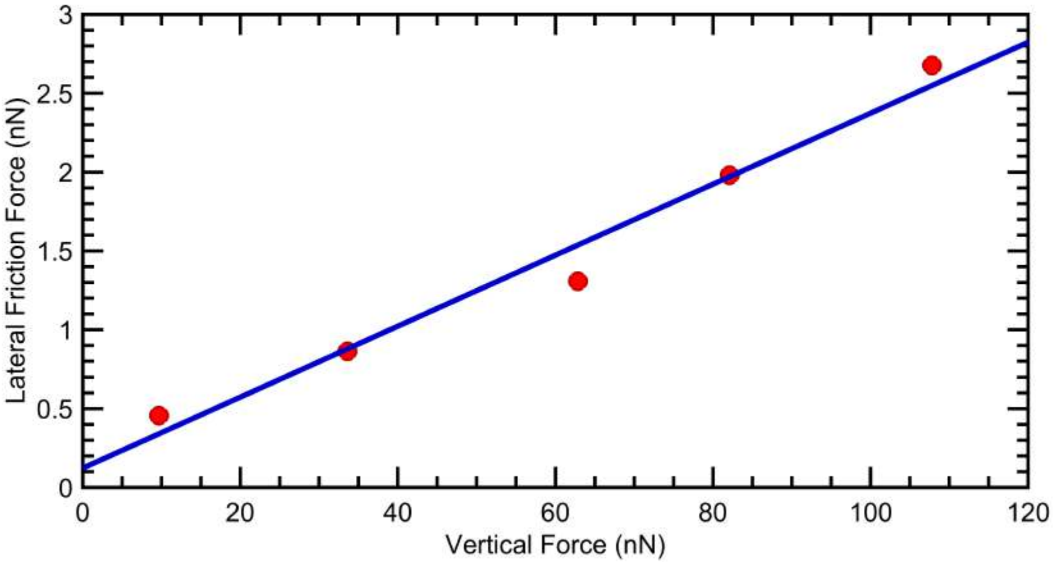

Figure 6.23: Friction force vs Vertical force curve for Pt-Gr NC

Additionally, Fig. 6.24 shows the relation between coefficient of friction and vertical force. A general trend of decrement of μ is found with the increase in vertical loading.

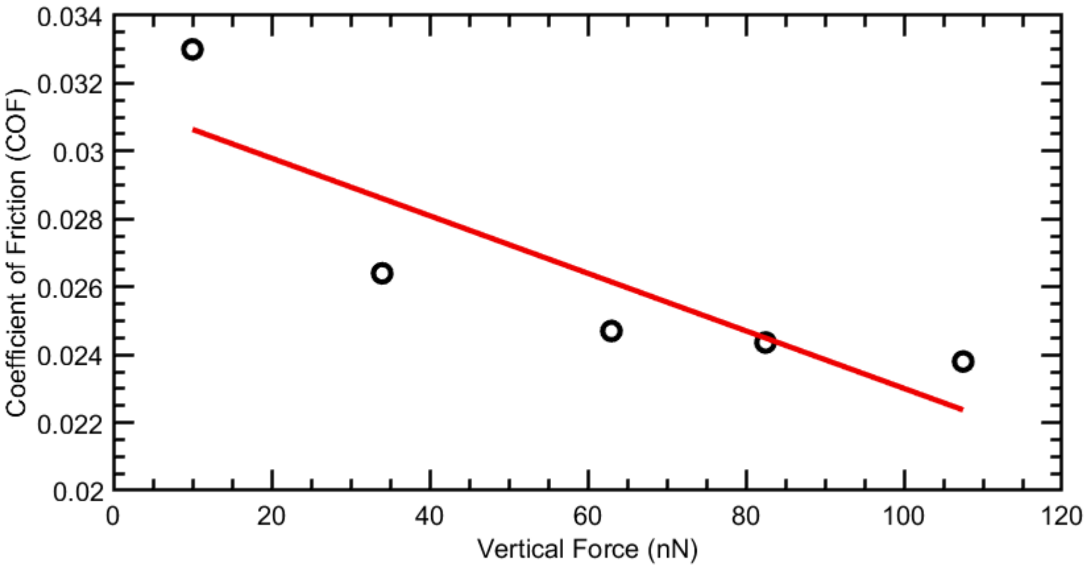

Figure 6.24: Friction Coefficinet vs. Vertical load

Table 6.4: Change in lateral and vertical force due to a change in sliding velocity in friction simulations

Velocity (m/s)	Lateral Force (nN)	Vertical Force (nN)
50	3.5075	1.0212
100	0.4570	9.6854
150	1.4274	9.6854
200	3.9059	0.9007

6.3.4 Variation in Sliding Velocity

All of the previous MD simulations are done with a sliding velocity of 100 m/s. That's why the effect of loading rate or sliding velocity is conducted here. Four different sets of sliding velocities are taken, 50 m/s,100 m/s,150 m/s,200 m/s, to examine their effect. Change in the values of friction force and normal force due to change in sliding velocity is given in the Table 6.4.

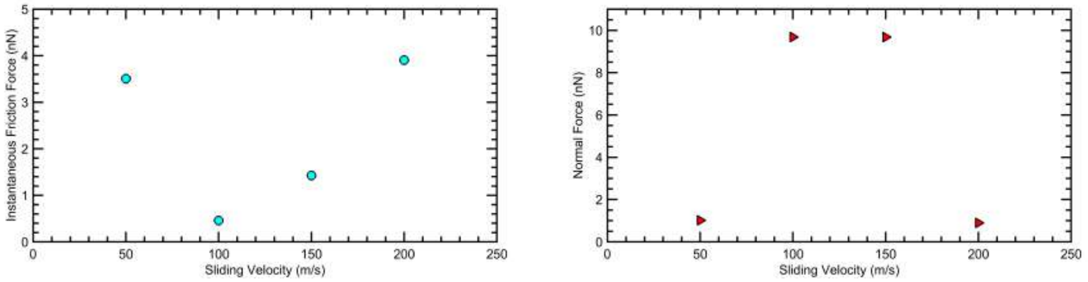

(a) Friction force vs. Sliding velocity

(b) Normal force vs. Sliding velocity

Figure 6.25: Effect of change in sliding velocity on Friction force and Normal force

Fig. 6.26 refers to the change in COF with respect to change in velocities. COF is higher in the lower sliding velocity region, whereas in the intermediate velocity range it is minimum. At higher sliding velocity, in the contact zone elastic behavior is prevalent which ensures lower friction force [124] [125]. Additionally, contact time is also shortened with increment in velocities, and may result in a lower COF. It is important to note that the test temperature has a significant impact on the friction force-sliding velocity relationship [126]. At temperatures close to the glass-transition point, the sliding velocity has a significant impact on friction, although at lower temperatures, the two variables are mostly independent of one another [127]. At 200 m/s sliding velocity, a sudden rise in COF is observed which may be incorporated with pre-wear characteristics where with more plastic deformation initiates more adhesion and so COF increases. A sliding velocity above 250 m/s gives rise to wear in the material, which is obtained from current study and can be visualized using Fig. 6.27

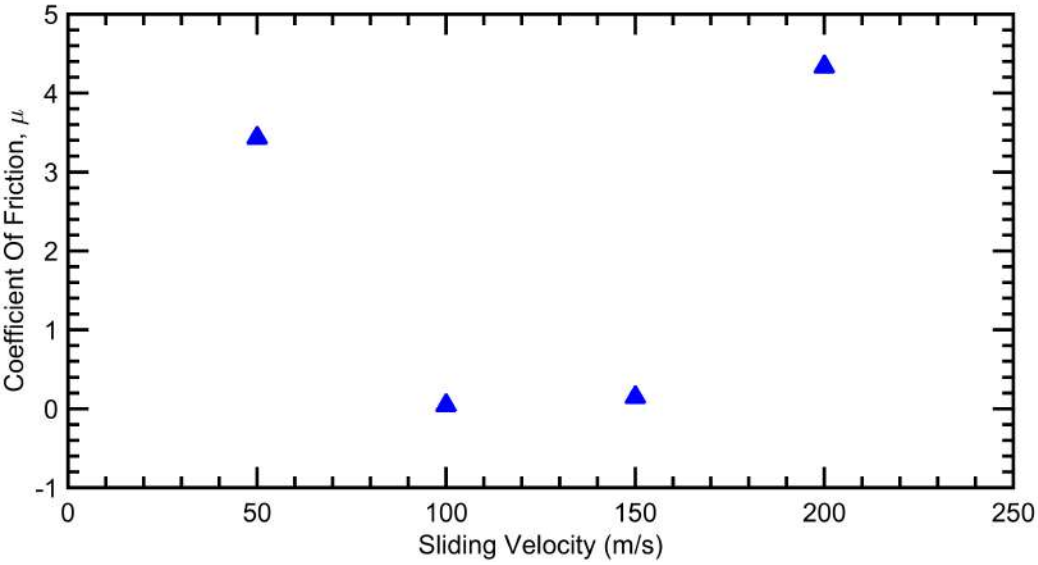

Figure 6.26: COF vs. Sliding velocity

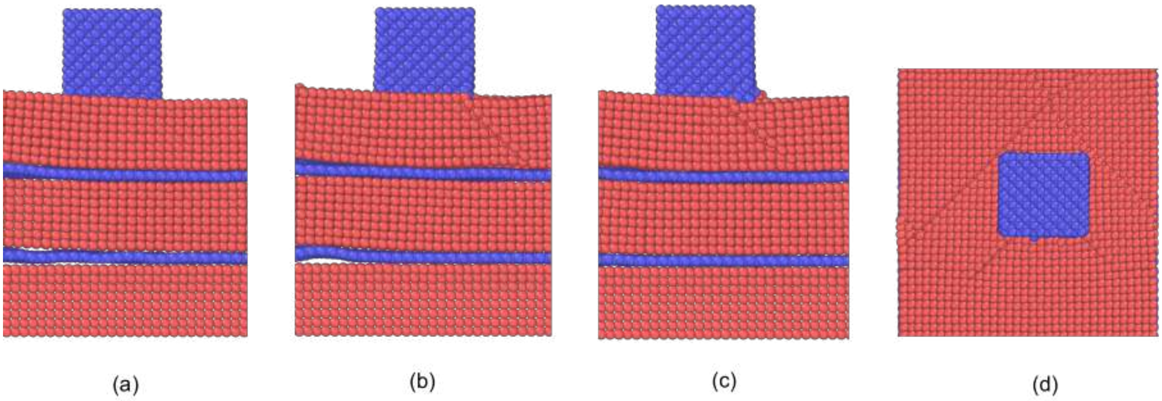

Figure 6.27: Initiation of wear with higher (250 m/s) sliding velocity; (a) No wear (b) Dislocation creation (c) Wear initiates (d) Top view of wear initiation

6.4 Section Summary

There are tribological properties that may be seen in every aspect of life, such as friction. Therefore, doing research into the impacts that friction has on any material of interest is of utmost significance if such research is to have any practical use in the real world. As a result, the focus of this chapter of my research was on the modeling of friction on NC and the influence that it has on NC as a result of changes to various parameters. The following is a synopsis of the results obtained in this chapter:

- Stick-slip condition of friction is evident in the simulations.
- Adhesion plays an important role in obtaining this stick-slip nature.
- For the same operating conditions, COF is higher for Pt-Gr NC than pristine Pt which makes it suitable for biosensor applications.
- Higher temperatures result in greater gains in thermal energy, which ultimately reduces friction by providing molecules with Adhesion plays a crucial part in achieving this stick-slip property.more energy to readily overcome potential obstacles. Consequently, the friction coefficient drops.
- A higher vertical load results in a larger contact area and, thus, a greater friction force but COF decreases.
- The friction between two materials is very sensitive to the sliding speed. Wear begins at a critical value of sliding velocity; in the case of the NC system under consideration, wear becomes visible at a sliding velocity of 250 m/s or higher.

Chapter 7

Tribological Properties: Wear

Wear occurs when one or both of two solid surfaces undergo damage or material removal as a result of a relative sliding, rolling, or impact action [2]. Wear is a complicated process, which makes it one of the most challenging aspects of tribology to study. From the previous chapter, (Ch. 6) a conclusion is drawn that, at a high sliding velocity Pt-Gr NC may go though wear. Therefore, from a practical point of view, one might expect to have data regarding any material's wear response before making use of it industrially. In this chapter, this study will span from designing a system of NC going through wear to evaluating wear rate, including theoretical aspects of wear and an attempt to compare the wear rate of NC with its pristine Pt counterpart.

7.1 Theoretical Background

Wear has been known to us for a long time and is one of the oldest manufacturing processes. Although it has some uses, its detrimental effects are increasingly evident in our day-to-day lives. Similar to friction, wear is not a characteristic of the material but rather a reaction of the system. Interface wear is affected by operating conditions. Assumptions about the wear rates of high-friction interfaces are often exaggerated [2].

There are times when the results of wear are disastrous. The plane carrying 88 people from Alaska Airlines went down in the Pacific Ocean on January 31, 2000, taking everyone's lives in the process. A jackscrew that had been improperly lubricated had experienced excessive wear, which ultimately resulted in the pilot losing control of the horizontal stabilizer of the plane [3].

This section will introduce brief overview of wear mechanisms throughout different scales, from macroscale to nanoscale.

7.1.1 Types of Wear Mechanisms

Wear can occur through various processes, of which mechanical processes and chemical reactions are the major types. There are mainly six types of wear mechanisms, and they are:

1. Adhesive wear
2. Abrasive wear
3. Fatigue wear
4. Impact by erosion
5. Chemical wear
6. Percussion

Fretting and fretting corrosion are two additional types of wear that are frequently experienced. These are not three separate mechanisms but rather combinations of the three different types of wear that can occur: adhesive, corrosive, and abrasive. Some estimates suggest that adhesive and abrasive wear mechanisms are responsible for two-thirds of the total wear that can be found in industrial settings. The gradual removal of material is how wear is caused by all mechanisms, with the exception of the fatigue mechanism [2].

7.1.2 Macroscale Wear Mechanisms

When two solid surfaces are brought together, the points of contact are those that have the greatest number of asperities. In most cases, the contact surfaces of each macroscopic asperity pair are not entirely flat. Instead, contact happens initially at smaller, microscopic asperities on these macro-asperities, and so on and so forth all the way down to the atomic or nanoscale [128]. The empirical Archard's law [129] is the most common law to describe wear at macroscale. This law can be interpreted mathematically as,

$$V = k\frac{Wx}{H} \tag{7.1}$$

Here, V is the wear volume, W indicates the applied normal load, x is the sliding distance, and the surface hardness is denoted by H. The following are common presumptions made in interpreting Archard's law: (1) the plastic deformation of surface asperities under stress, and (2) particles of wear are generated [128].

When it comes to wear processes that occur while sliding in AFM, the most relevant ones are adhesive and abrasive wear. The phenomenon known as adhesive wear takes place when two sliding surfaces that are subjected to a load join together via the solid-phase welding of asperities [2]. After then, the contacts are torn by sliding, which may lead to the separation of a fragment from one surface and its attachment to another surface at the same time. When compared to adhesive wear caused by comparable pairings, the wear caused by different pairs is often smaller.

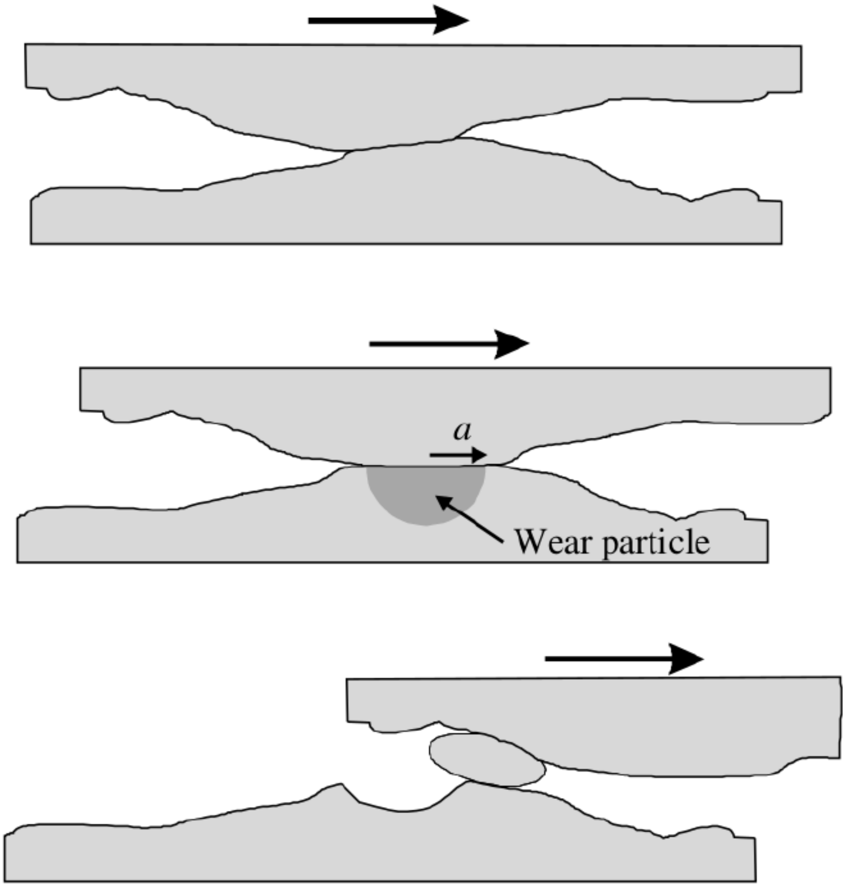

Figure 7.1: An illustration of the formation of a wear particle due to an asperity contact at the microscale [3].

Adhesive wear may be studied using Archard's simple wear model [129]. Higher adhesion forces in the contact zones, as predicted by this model, will increase the likelihood that a wear fragment will be pulled out. Because adhesive forces scale with surface energy, larger levels of surface energy should lead to higher levels of wear rates [3]. Because the surface energy is so dependent on the chemical composition of the surface, wear rates resulting from the adhesive mechanism should be extremely sensitive to the presence of contamination layers or lubricant films. This is because these factors have a significant impact on the adhesion that occurs at solid–solid contacts [3].

When asperities of a rough, hard surface or hard particles glide over a softer surface and cause plastic deformation or fracture, abrasive wear occurs. In the case of ductile materials

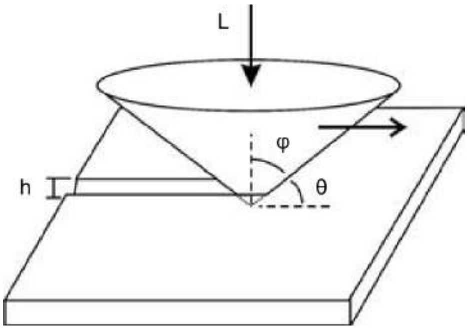

Figure 7.2: A cone shaped asperity plowing into a softer surface to generate an abrasive wear groove. [3]

with a high fracture toughness (e.g., metals and alloys), the plastic flow of the softer material is caused by hard asperities or hard particles [2]. There are three significant deformation modes in abrasive wear: ploughing, wedge formation, and cutting. Material is displaced to the sidewalls of the worn groove during plowing, resulting in the creation of a ridge without material removal. In wedge formation, material is shifted from the sides of a groove to the front. When the ratio of the shear strength of the interface to the shear strength of the bulk is large, wedge formation often occurs. Cutting is the removal of material from a surface in the form of discontinuous or ribbon-shaped fragments [130].

Consider a cone of hard material cutting a groove into a softer substance as a basic approach to mimic the abrasive wear of an asperity in a two-body process or the corner of a grit particle in a three-body process [3] as shown in the Fig. 7.2

For a groove depth of h and $tan\theta$ being the slope of cone, volume V is displaced during sliding of asperity a distance x is written by,

$$V = xh^2 tan\phi = xh^2 cot\theta \tag{7.2}$$

Here, the loading force L is supported by only the first half of the asperity over an area $\pi a^2/2$, yields

$$L = \frac{1}{2} H\pi a^2 = \frac{1}{2} H\pi h^2 cot^2\theta \tag{7.3}$$

Where, H equals to hardness of the soft surface. To omit h by combining equations 7.2 and 7.3, following equation for wear rate can be obtained:

$$W = \frac{V}{s} = \frac{2tan\theta}{\pi} \frac{L}{H_0} \tag{7.4}$$

This equation has same form as that of Archard's law (Eq. 7.1), where k = 2tanθ/π.

One issue with Eq. (7.4) is that it predicts significantly greater wear rates than actually experienced. The assumption that all displaced material is lost at the surface is an evident contributor to this overestimation. In fact, with each sliding pass, only a portion of the displaced material detaches, while the remainder accumulates around the groove's borders [3].

7.1.3 Nanoscale Wear Mechanisms

The nanoscale roughness of most, if not all, surfaces is widely recognized [131]; most mechanical contact takes place between the tiniest nanoscale asperities. Contacts at the nanoscale may be especially vulnerable to unwanted wear due to the high surface-to-volume ratio, which can significantly compromise the reliability and longevity of nanoscale electronics. Characterizing tribological phenomena at tiny sizes may be difficult using conventional approaches and models. That's why it takes research and simulations to learn about wear processes [132].

Some earlier research have shown, via both simulation and experimental methods, that nanoscale mechanical interactions may follow the predictions of continuum contact mechanics [128,133]. However, it is not always appropriate to extrapolate results from continuum models to the nanoscale. In reality, the vast majority of research has revealed that continuum contact models cannot be used to explain interactions at the nanoscale [134–136]. This suggests that nanoscale wear does not strictly adhere to continuum laws [130].

Some different nanoscale wear processes have been postulated. To begin, much as on a larger scale, nanoscale wear may happen by fracture or plastic deformation [130]. In crystalline materials, imperfections and defects in the crystal structure, known as dislocations, move and cause macroscale plastic deformation. However, the contribution of dislocations to the yield stress becomes insignificant when the size of the region undergoing plastic flow becomes much smaller than the typical distance between dislocations, and the yield stress is instead governed by the force required to slide one plane of atoms over another [3]. The theoretical shear stress necessary to move one plane of atoms over another, in a flawless crystal free of dislocations, is given by

$$\tau_c = \frac{G}{2\pi} \tag{7.5}$$

Due to the mechanical deformation, the local temperature at the contact may rise, which might further accelerate wear. Wear at the nanoscale may include the loss of a single atom from a surface, according to another finding from nanoscale studies of wear [131, 137]. During atom-by-atom removal, two surfaces come into contact in quasi-static equilibrium, and an uncoordinated atom from one surface may make bonds with one or more atoms from the opposing surface. The established connection may be broken by sliding, and the atom can move from one surface to another. Compressive or shear loads may assist this thermally triggered process [130]. Consequently, while a sliding surface may begin with a low density of flaws and defects, during the early stages of wear, plastic deformation caused by contacting asperities rapidly increases dislocation density in the near-surface layer, resulting in the formation of a fine grain or nearly amorphous structure [3]. Although analysis of wear has been done extensively at nanoscale previously, the complete mechanism is yet to be realized. Therefore, MD simulation could be a better solution to observe physics of materials going under wear for changes in different parameters.

7.2 Simulation Methodology: Wear

The simulated system consists of a double layered Pt-Gr NC and a half-spherical shaped Diamond indenter. Since wear is a surface phenomena and also the interatomic potentials used in this study having a cutoff value, the number of graphene layers should not account for any influence on the wear rate. Wear rate at a same operating conditions for single and double graphene layer(s) gives almost similar results given in the Table 7.1. That's why any number of layers of graphene can be chosen for this study irrespective of any significant variations. Diamond being a hard material is used as a indenter to simulate the wear process.

Table 7.1: Comparison of wear rate for single and double graphene layer(s) Pt-Gr NC

Wear Rate at 0.75 nm indentation depth	**Single graphene layer Pt-Gr NC**	115.6847/nm
	Double graphene layers Pt-Gr NC	117.2669/nm

7.2.1 Diamond Indenter

Atomsk [48] is used to design the initial setup of the system. Firstly, a Diamond block of 4.2804 nm X 4.2804 nm X 2.8536 nm is created using atomsk. Afterwards, a half-sphere of 2.5 nm radius is curved out of the Diamond block.

Listing 7.1: Diamond Indenter creation in atomsk

```
% CREATING THE DIAMOND BLOCK
atomsk −−create diamond 3.567 C −duplicate 12 12 8
DiaBlock.cfg
% CURVING OUT A SPHERE OUT OF THE BLOCK
atomsk −select out sphere 21.402 21.402 28.536 25
```

```
-rmatom select DiaSph.cfg
% LEAVING OUT SOME MOLECULES FROM
% THE TIP TO HAVE FLAT SURFACE
atomsk -cut below 5 z DiaInd.cfg
```

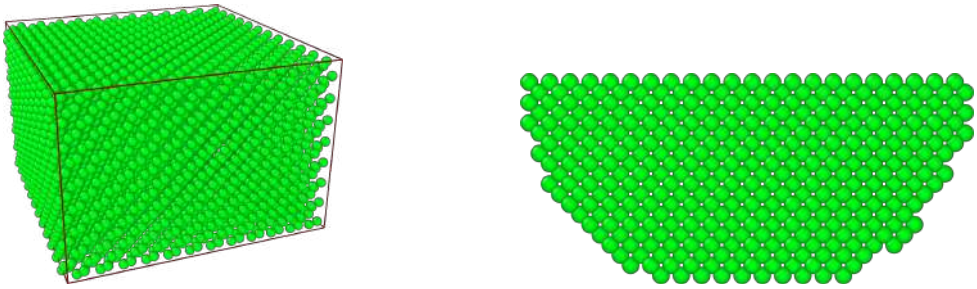

(a) Diamond block (b) Diamond sphere

Figure 7.3: Diamond indenter

7.2.2 System Construction

After constructing the indenter, it is merged with a double layered Pt-Gr NC model, previously made, leaving an initial gap of 1 nm between them. The whole system can be observed in the Fig. 7.4.

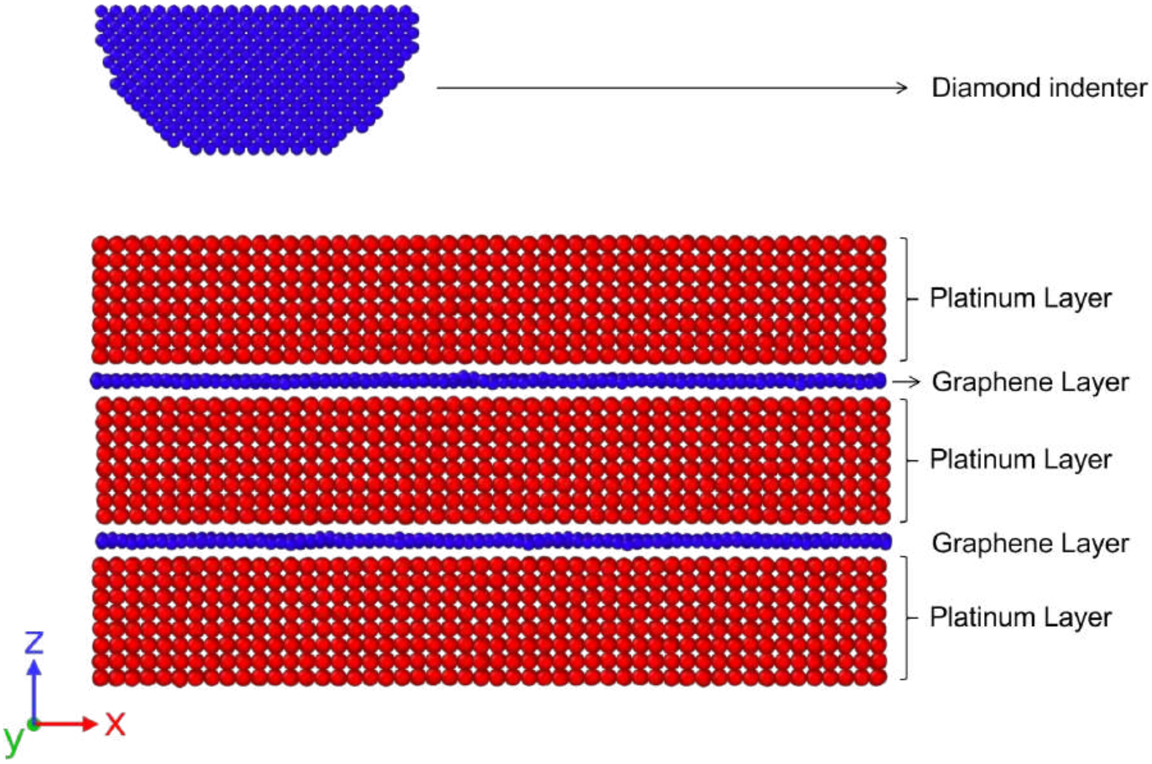

Figure 7.4: Complete system for wear simulation.

7.2.3 Boundary Conditions

The system is simulated with periodic boundary conditions on both X and Y directions. But on the Z direction, to capture the wear process, non-periodic and shrink-wrapped with a minimum value, m [91], boundary condition is applied. Boundary condition in the Z direction is made so that no molecules of the NC can reach out to the top of the box after being pressed by the indenter.

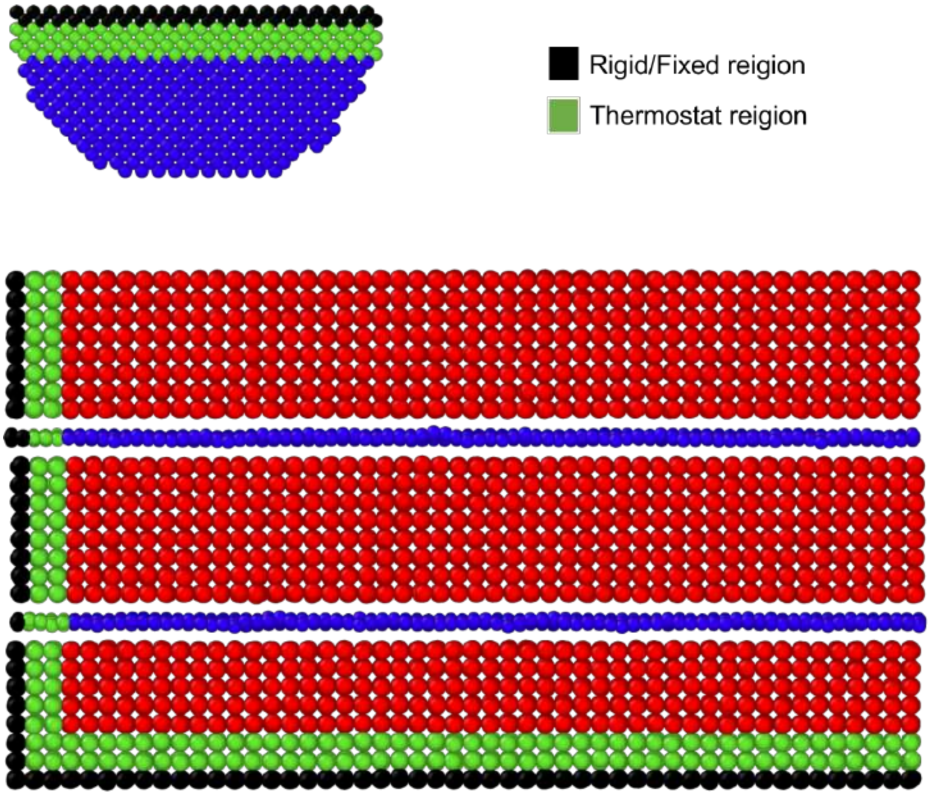

Figure 7.5: Boundary conditions on the wear system.

Just like the friction simulation, a single layer of molecules at bottom and left is taken to be rigid region, where the molecules are kept fixed by applying zero force to this region.

```
fix     lo_fix fixLo setforce 0.0 0.0 0.0
```

Two layers of molecules are kept as thermostat region can be seen from the Fig: 7.5. NVT emsemble is applied in this region to ensure heat release due to wear.

```
fix     6 nvtSlab nvt temp ${T} ${T} 0.5
```

For the Diamond indenter, the top layer is kept as rigid body where all the forces are applied. Below this layer, three layers of molecules are fixed with a NVT ensemble. All the other layers apart from these are fixed with NVE ensemble.

```
fix     rigidFix tipF rigid single force 1 on off on
```

```
                    torque 1 off off off
```

7.2.4 The Dynamics

At the beginning of the process, a force in the x-direction is applied to the indenter's rigid layer, causing it to advance a short distance and position itself in an appropriate location. After that, a velocity of 100 meters per second is imparted in a direction parallel to the z-axis and moving downward toward the stiff layer. This was done in order to determine the necessary force for the associated indentation depth. This was done so that the appropriate amounts of force could be applied and maintained throughout the simulation for a certain indentation depth. The last step in determining how wear occurs involves moving the indenter along the x-axis while simultaneously recording the number of atoms that are lost owing to wear. This information will be evaluated at a later time. The whole system is kept at a temperature of 300 K.

7.3 Parametric Study

7.3.1 Load for Different Indentation Depth

Within the context of the atomic sliding analysis, the notion of "indentation depth" has to be explained in more detail. The penetration depth of the asperity tip is used to calculate the indentation depth of a hard asperity in any typical research of sliding. This depth is measured from the surface of the soft material. However, on the atomic scale, there is no such thing as a definite surface since nuclei are surrounded by electron clouds [138]. Assuming that the surfaces of the diamond indenter and the NC slab are defined by the envelopes at the theoretical radii of their surface atoms, respectively, allows us to handle this issue in a manner that is both convenient and accurate. By doing it this way, the depth of the indentation will be brought into line with the traditional definition [138].

Wear can occur at different indentation depth. That's why in this study, wear effect at different indentation depth will be analyzed. Since the system of Diamond indenter and NC slab will be kept at a constant vertical loading during the simulation, the loading required for different indentation depths will be calculated first. To do this, the indenter was allowed to go downward at a constant velocity of 100 m/s. This was done for a ample of time to get at least 1.5 nm of indentation depth. During the simulation, corresponding required force is recorded and plotted against the indentation depth (Fig. 7.6). These force value will be used for latter analysis.

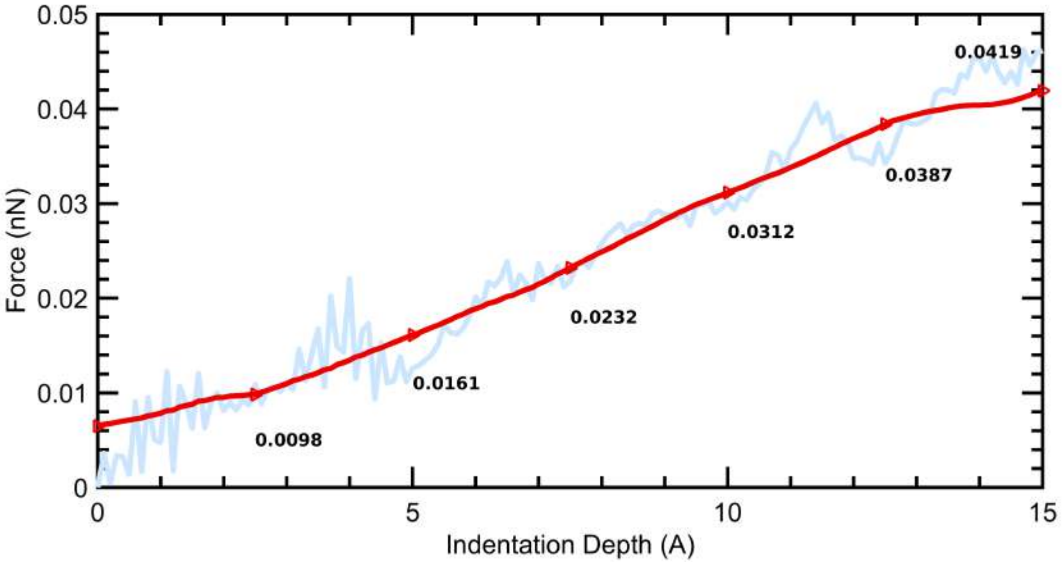

Figure 7.6: Indentation depth Vs. Required force curve to evaluate which force is to be held contanst during MD simulation for a particular indentation depth.

7.3.2 Wear Mechanism

The simulation of wear is conducted by sliding the diamond indenter at a constant velocity under the influence of a series of constant load obtained from Fig. 7.6. For a indentation depth of 2.5 angstrom, the indenter barely scratches the NC surface. Significant wear may be realized from 5 angstrom indentation depth, where the deformation of the NC slab has four distinct regions. The regions are, (i) No wear (ii) Adhering (iii) Ploughing (iv) Cutting regions, as shown in Fig. 7.7.

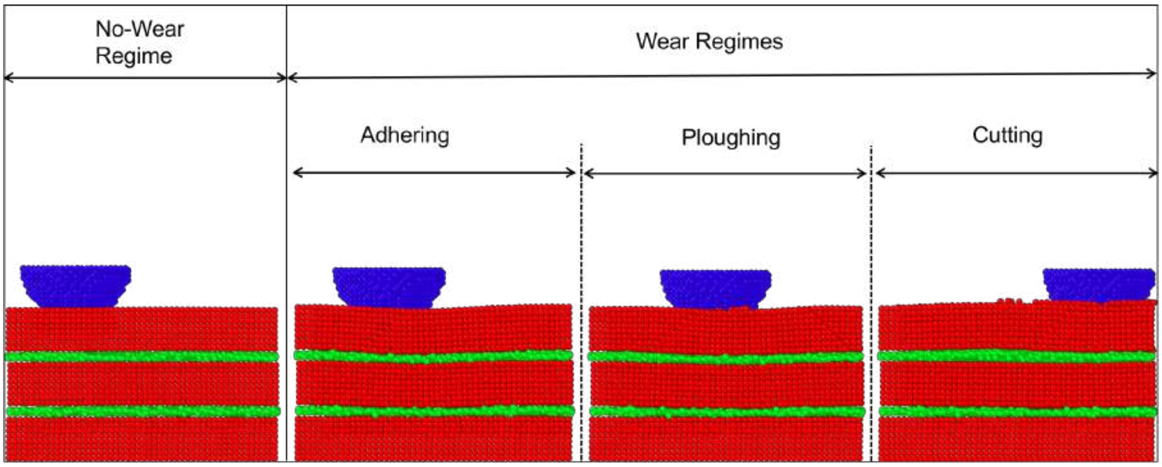

Figure 7.7: Four different wear regions at an indentation depth of 5 angstrom.

In the no-wear regime, the NC atomic lattice deforms elastically only. Following the removal of the diamond indenter, the distorted lattice is completely restored. In this instance, sliding does not lead to wear or dislocation.

During adhesion, the sliding of the diamond breaks the atomic bonds of certain surface Pt atoms. These Pt atoms then stick to and migrate over the asperity surface. They may nonetheless establish new connections with other surface atoms of Pt and return to the atomic lattice. During sliding, the preceding process occurs repeatedly, generating a structural change in the Pt lattice near the surface and producing surface roughness. Currently, dislocations are also activating the subsurface [138].

A substitution of ploughing for adhering deformation occurs afterwards. In this regime, the subsurface deformation zone becomes quite vast, and a huge number of dislocations are triggered. And lastly, cutting regions occur where atoms are removed from the surface.

At higher indentation depths, from 7.5 - 15 angstrom, ploughing and cutting regions of wear are significant. Wear process obtained from MD simulation in this study can be viewed as a series of figures from Fig. 7.8 to Fig. 7.10.

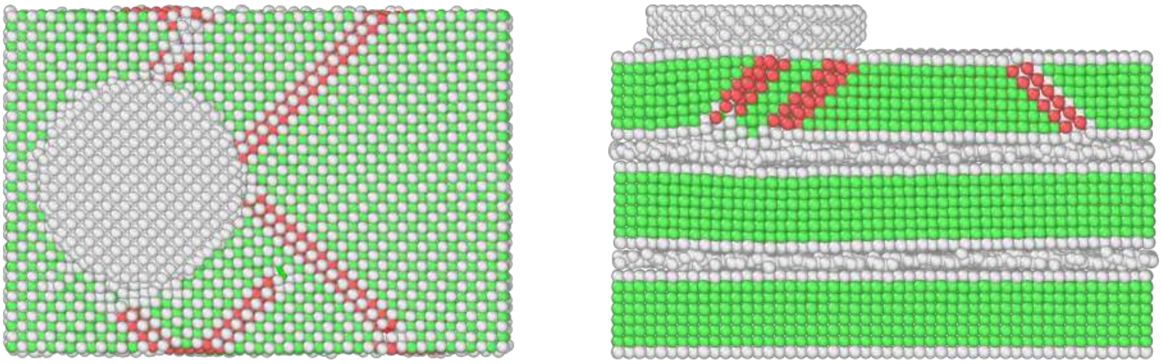

(a) Top view

(b) Front view

Figure 7.8: Dislocations occurs during wear simulation at 1 nm indentation depth.

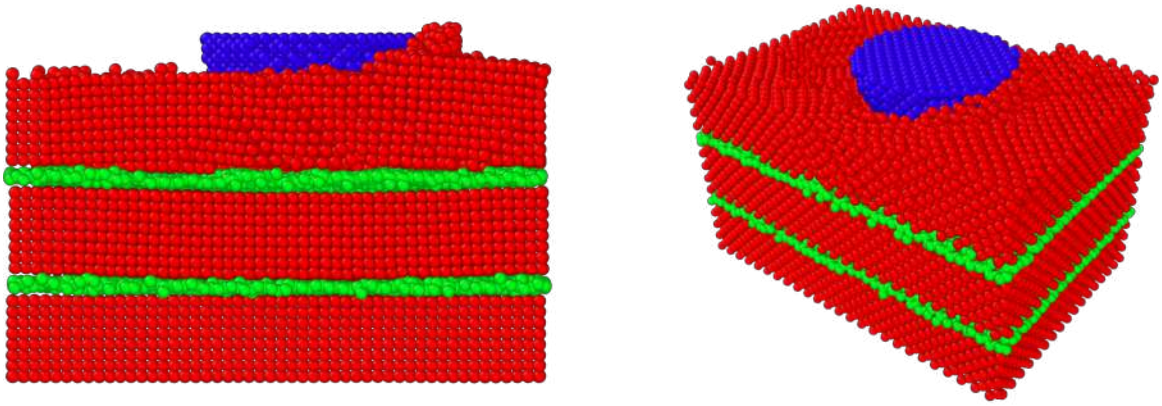

(a) Front view

(b) Perspective view

Figure 7.9: Ploughing of material from the surface at 1 nm indentation depth.

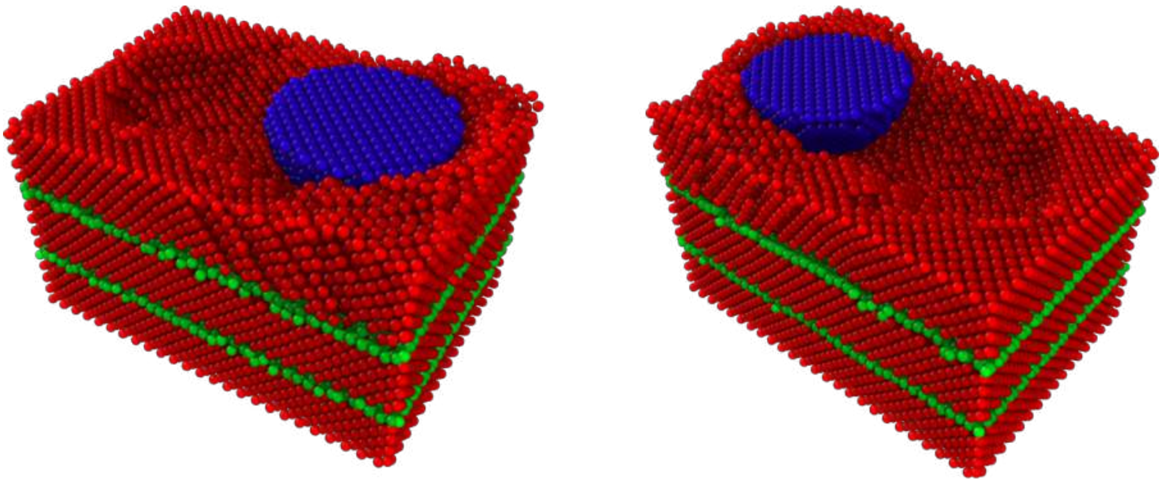

Figure 7.10: Removal of materials due to wear at 1 nm indentation depth (perspective view).

7.3.3 Wear Rate Calculation of Pt-Gr NC

Data obtained from the wear simulations at different normal loadings are used to calculate wear rate of the NC. Quantity of the lost atoms is calculated by subtracting number of atoms at each simulation steps in a predefined region from the initial number of atoms at that region. Afterwards, the calculated quantity of wear atoms is plotted against the sliding distance for different indentation depth (Fig. 7.11). Wear rate is obtained by the finding out the slope of the curves. Each of the curve is fitted to have a linear trend.

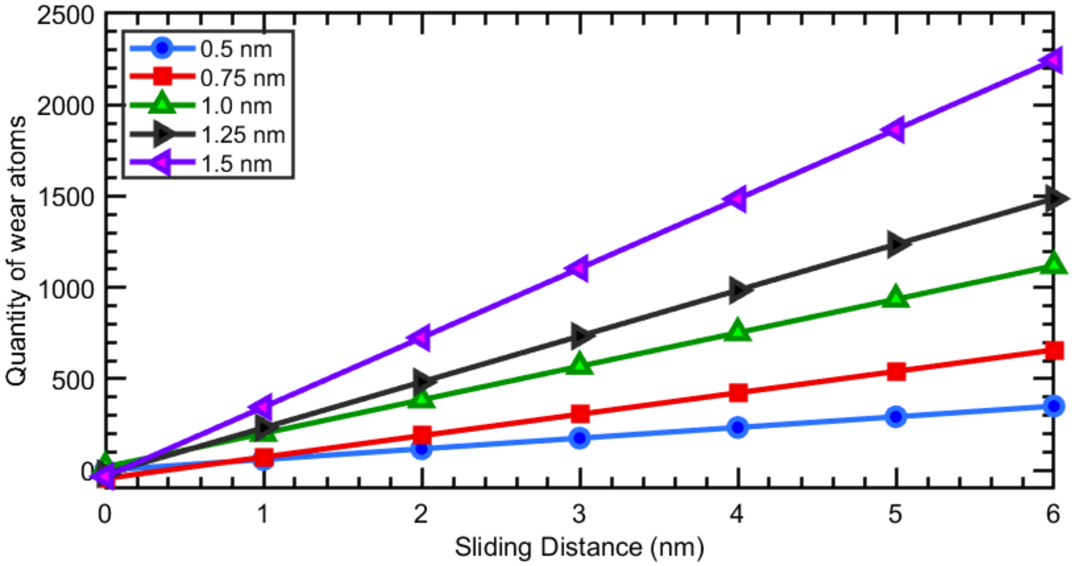

Figure 7.11: Quantity of weared atoms vs Sliding distance at different indentation depth.

Wear rates for different indentation depths and corresponding normal forces are given in the following table 7.2.

Table 7.2: Analyzed Wear rate data for NC

Indentation Depth (nm)	Wear Rate (1/nm)	Normal Force (nN)
0.5	25.6875	0.0161
0.75	117.2669	0.0232
1.0	183.5762	0.0312
1.25	250.9143	0.0387
1.5	379.78	0.0419

Individual plots of wear rate against indentation depth and normal force is depicted in the Fig. 7.12 and 7.13 respectively.

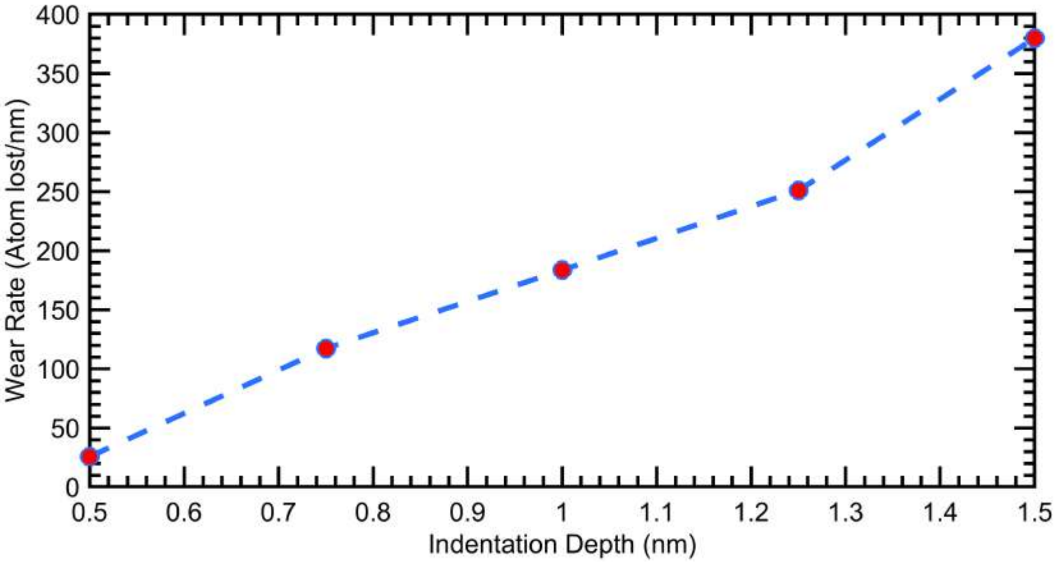

Figure 7.12: Wear rate vs Indentation depth trendline.

From the Fig. 7.11 one may conclude that, number of lost atoms is directly proportional to sliding distance. Also from Fig. 7.13 it is obtained that, as expected, the rate of wear increases with the increment in normal load. Therefore, the wear rate, obtained from MD simulations, is directly proportional to the normal load. Another form of Archard's empirical law for a mass loss of M through wear with normal load T_n and sliding distance d is: $M = kT_nD$, with k being an empirical constant [128]. So, a consistency with the Archard's law [129] is found in this study as the number of lost atoms changes linearly with both the sliding distance and normal load. The implication of this findings is that, Archard's law may be directly applicable at the nanoscale which is also found by Sha et al. [128], but in contrary to common findings [131, 139, 140].

We note that earlier experimental investigations have shown a nonlinear relationship between sliding distance and force and material loss [131, 139]. This disparity may be ex-

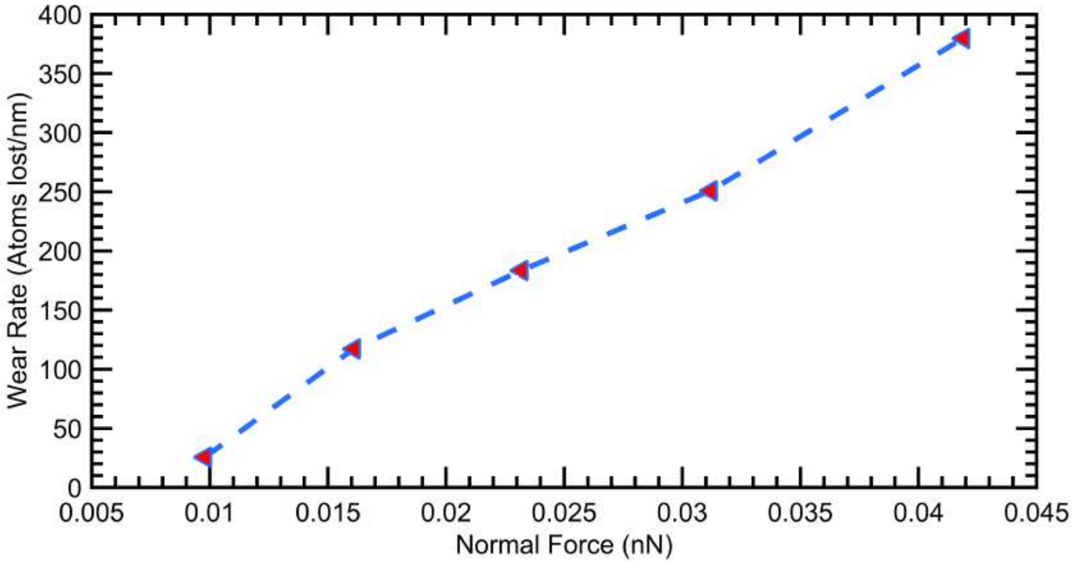

Figure 7.13: Wear rate vs. Normal force curve.

plained by the following variables: First, the sliding velocity in these tests was orders of magnitude lower than in the models, i.e. 20 m/s, which is close to the working conditions of some micromechanical systems (MEMS) [136]. It has been shown that heat activation plays a significant part in wear processes, which may result in non-linearity [131]. Therefore, it is plausible to assume that the thermal effect in slow-speed wear is substantial, but it is almost nonexistent in high-speed wear. Secondly, the surfaces of the materials utilized in these tests are often polluted with different molecules, oxides, and other chemical species, but the surfaces of the simulated samples are pristine. It has been shown that such pollutants may likewise cause nonlinearity [140]. Notably, this difference is not due to the size of the tip or the magnitude of the applied normal load, since the tip radius and range of applied normal loads in our MD simulations are equivalent to those employed in earlier research [131, 139].

7.3.4 Wear Rate of Pristine Pt

MD simulations for evaluating wear rate on pristine Pt sample is done in this study for making a comparison with that of NC in the following subsection. A sample size of 9.80975 nm X 6.67063 nm X 8.63258 nm of Pt is taken for the simulation. Previously mentioned interatomic potentials are used in this simulations, Q-SC [110] potential for Pt and SW [52] potential for diamond indenter. Initially, a simulation for obtaining force vs indentation depth relation is carried out, and the outcome is Fig: 7.14.

Afterwards, the diamond indenter is let to slide over the surface at different constant indentation depth to simulate wear in the Pt slab. Just like the findings for the NC, Pt also show

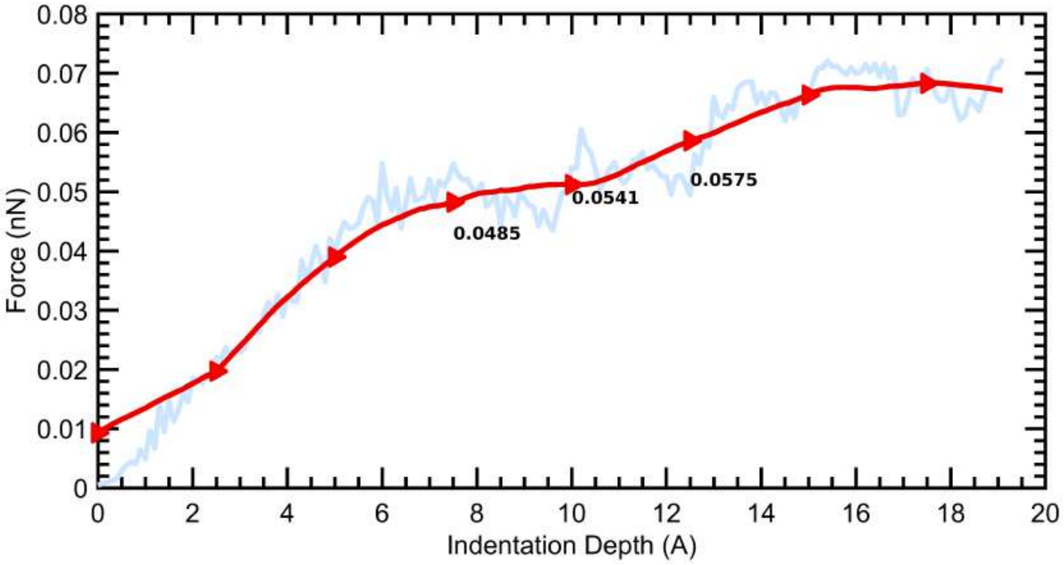

Figure 7.14: Required force vs Indentation depth for pristine Pt.

similar wear trend which can be verified from Fig. 7.15 [128].

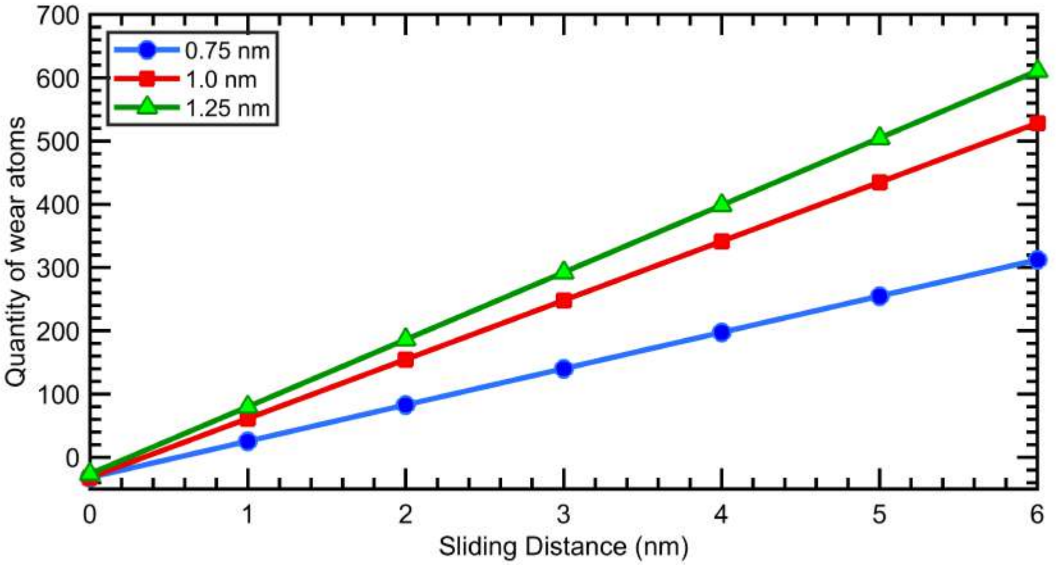

Figure 7.15: Wear rate vs Sliding distance for pristine Pt.

7.3.5 Comparison of Wear Rate between Pt and Pt-Gr NC

Table 7.3: Comparisonal Analysis between Pristine Pt and Pt-Gr NC's Wear Rate for different Indentation Depth

Indentation depth (nm)	Wear Rate (prinstine Pt) 1/nm	Wear Rate (NanoComposite) 1/nm
0.75	57.3498	117.2669
1.0	93.3805	183.5762
1.25	106.1788	250.9143

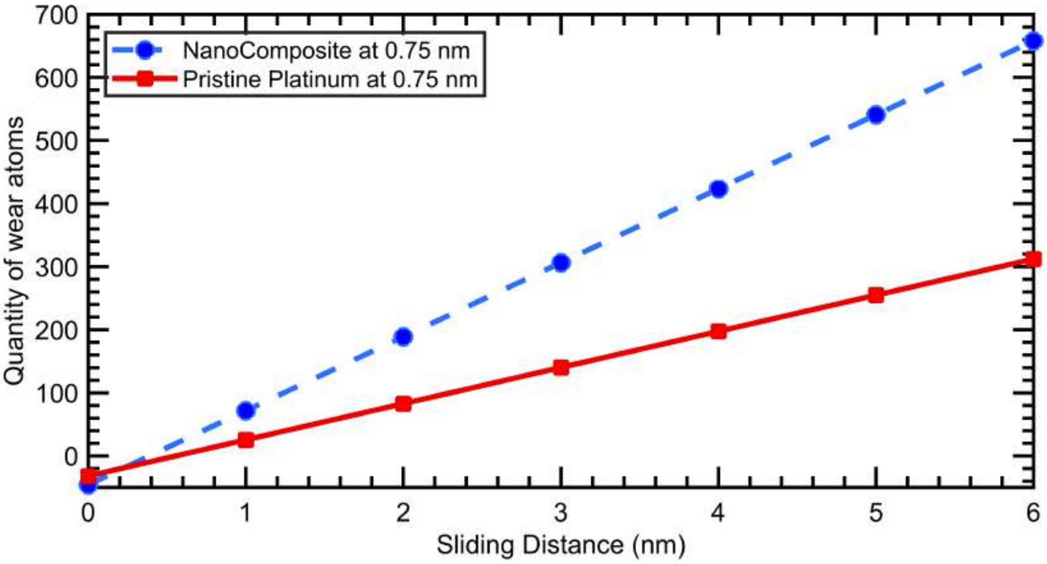

Figure 7.16: Comparison of wear rate between Pristine Pt and NC at 0.75 nm indentation depth.

From the Table 7.3 and a series of figures from Fig. 7.16 to 7.18 show that wear rate for NC is more than wear rate for pristine Pt at the same indentation depth. Although pristine Pt requires more force (refer to Fig. 7.14) than Pt-Gr NC (refer to Fig. 7.6) to obtain desired indentation depth, wear rate is more for NC.

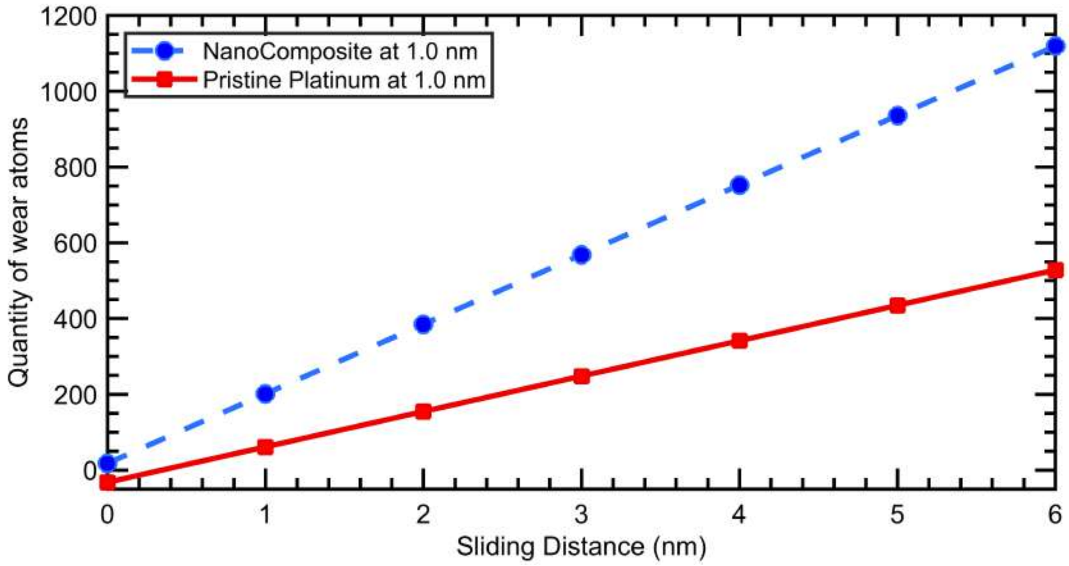

Figure 7.17: Comparison of wear rate between Pristine Pt and NC at 1.0 nm indentation depth.

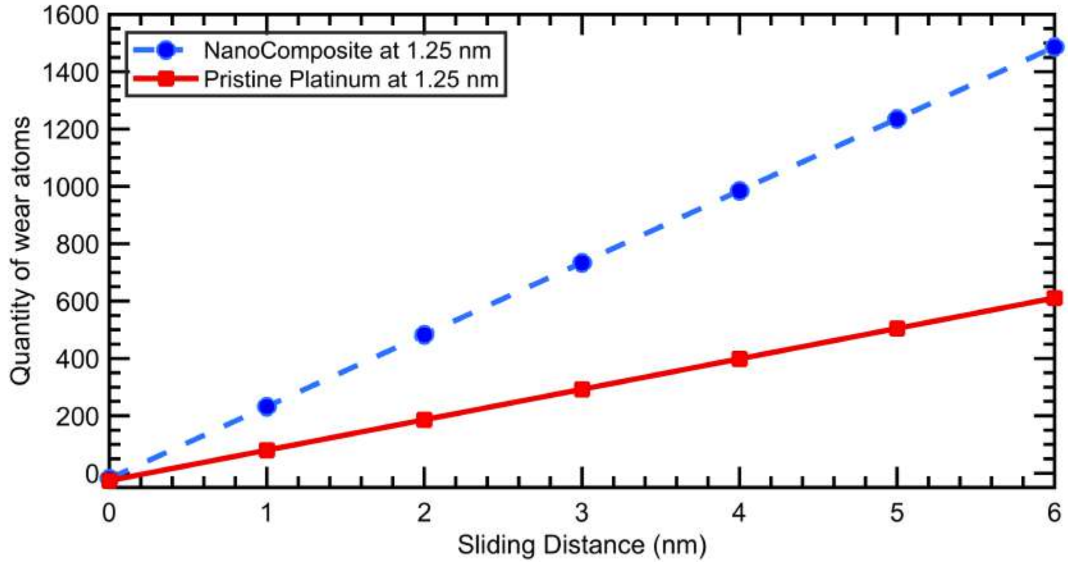

Figure 7.18: Comparison of wear rate between Pristine Pt and NC at 1.25 nm indentation depth.

7.4 Section Summary

Wear is the gradual degrading of materials that might eventually cause them to fail or become useless [139]. The complicated structure of contact between two bodies is one reason why it is so hard to grasp the underlying mechanics of wear. Advantages of MD simulations include the ability to monitor the motion of each atom, to fine-tune the sliding geometry and conditions, and to directly measure several important physical quantities, such as the number of atoms lost, the number of atoms in bonding contact at the interface, and the forces experienced by each atom [140]. The following is a summary of this chapter:

- At nanoscale, adhesive and abrasive wear is dominant.
- At a lower indentation depth, wear has four distinct regions - no wear, adhering, ploughing, and cutting.
- Number of lost atoms is directly proportional to sliding distance and normal load.
- Wear at nanoscale is consistence with the Archard's law.
- Thermal/heat activation effect on wear can be mitigated by higher sliding speed (around 100 m/s).
- Wear rate at different indentation depth for Pt-Gr NC is higher than Pristine Pt

Chapter 8

Concluding Remarks

With an aim to filling the gap in proper evaluation of mechanical properties of Pt-Gr NCs, this study has been conducted. To know how the mechanical properties are improved with the inclusion of graphene sheets into platinum, a series of molecular dynamics simulations were conducted throughout this study. Also, the underlying intricate surface mechanisms of friction and wear were also studied here. The followings are the findings gained through this research work:

- Tensile testing shows that, with the incorporation of graphene sheet into Pt boosts mechanical properties of the Pt-Gr NCs than its pristine Pt counterparts. Therefore, this NC can be used for the applications where better mechanical properties are expected.
- Inclusion of graphene layers ensures a increment in mechanical properties by entrapping dislocations up to a level.
- At a higher temperature, yield strength and ultimate stress of the Pt-Gr NCs remains almost similar whereas pristine Pt shows a declination in these properties. This finding enables the usage of Pt-Gr NCs at a higher level of temperature where early yielding is not expected.
- Pt-Gr NCs perform poorly under lateral loads. So, it is suggested to not apply for the situations under lateral loading conditions.
- Pt-Gr NCs undergoing friction force ensure stick-slip condition. Pristine Pt has a lower friction force, and so is COF, than Pt-Gr NC which enables NC to be better fit for some biosensor applications.
- Thermal activation plays a bigger part in the declination of the value of COF with the increment of temperature is verified here.

- At a higher sliding velocity, more than 250 m/s, wear may initiate on the surface.
- Adhesive and abrasive wear play an important role in the nanoscale wear mechanism.
- Number of graphene layers does not have any significant effect on the wear rate.
- Archard's empirical law for wear can be applied to nanoscale.
- There is a possibility that higher surface energy leads to increased wear rate for Pt-Gr NCs than pristine Pt.

References

[1] Filip Henrik Larsen. Molecular dynamics modeling of single asperity contact. Master's thesis, 2017.

[2] Bharat Bhushan. *Introduction to tribology*. John Wiley & Sons, 2013.

[3] C Mathew Mate and Robert W Carpick. *Tribology on the small scale: a modern textbook on friction, lubrication, and wear*. Oxford University Press, USA, 2019.

[4] Yalin Dong, Qunyang Li, and Ashlie Martini. Molecular dynamics simulation of atomic friction: A review and guide. *Journal of Vacuum Science & Technology A: Vacuum, Surfaces, and Films*, 31(3):030801, 2013.

[5] Flake C Campbell. *Structural composite materials*. ASM international, 2010.

[6] Liang Huang, Wen Zhou, Hao Xu, Lu Wang, Jie Zou, and Qiumei Zhou. Dynamic fluid states in organic-inorganic nanocomposite: Implications for shale gas recovery and co2 sequestration. *Chemical Engineering Journal*, 411:128423, 2021.

[7] Trevor William Clyne and Derek Hull. *An introduction to composite materials*. Cambridge university press, 2019.

[8] Hurang Hu, Landon Onyebueke, Ayo Abatan, et al. Characterizing and modeling mechanical properties of nanocomposites-review and evaluation. *Journal of minerals and materials characterization and engineering*, 9(04):275, 2010.

[9] Changgu Lee, Xiaoding Wei, Jeffrey W Kysar, and James Hone. Measurement of the elastic properties and intrinsic strength of monolayer graphene. *science*, 321(5887):385–388, 2008.

[10] JA Heinberg and HW Zandbergen. Superlubricity of graphite. physical reviews letters. *The American Physical Society*, 92(12), 2004.

[11] Ze Liu, Jiarui Yang, Francois Grey, Jefferson Zhe Liu, Yilun Liu, Yibing Wang, Yanlian Yang, Yao Cheng, and Quanshui Zheng. Observation of microscale superlubricity in graphite. *Physical review letters*, 108(20):205503, 2012.

[12] Alexander A Balandin, Suchismita Ghosh, Wenzhong Bao, Irene Calizo, Desalegne Teweldebrhan, Feng Miao, and Chun Ning Lau. Superior thermal conductivity of single-layer graphene. *Nano letters*, 8(3):902–907, 2008.

[13] Matthew Yankowitz, Shaowen Chen, Hryhoriy Polshyn, Yuxuan Zhang, K Watanabe, T Taniguchi, David Graf, Andrea F Young, and Cory R Dean. Tuning superconductivity in twisted bilayer graphene. *Science*, 363(6431):1059–1064, 2019.

[14] AR Alian, MAN Dewapriya, and SA Meguid. Molecular dynamics study of the reinforcement effect of graphene in multilayered polymer nanocomposites. *Materials & Design*, 124:47–57, 2017.

[15] Nariman Yousefi, Xinglin Lu, Menachem Elimelech, and Nathalie Tufenkji. Environmental performance of graphene-based 3d macrostructures. *Nature nanotechnology*, 14(2):107–119, 2019.

[16] Yongchao Si and Edward T Samulski. Exfoliated graphene separated by platinum nanoparticles. *Chemistry of Materials*, 20(21):6792–6797, 2008.

[17] Madhuri Sharon, Isaac Nandgavkar, and Maheshwar Sharon. Platinum nanocomposites and its applications: A review. *Advances in materials Research*, 6(2):129, 2017.

[18] Wu-Gui Jiang, Yao Wu, Qing-Hua Qin, Duo-Sheng Li, Xiao-Bo Liu, and Ming-Fu Fu. A molecular dynamics based cohesive zone model for predicting interfacial properties between graphene coating and aluminum. *Computational Materials Science*, 151:117–123, 2018.

[19] Chia-Liang Sun, Jheng-Sin Su, Shun-Yi Lai, and Yu-Jen Lu. Size effects of pt nanoparticle/graphene composite materials on the electrochemical sensing of hydrogen peroxide. *Journal of Nanomaterials*, 2015, 2015.

[20] Kimihisa Yamamoto, Takane Imaoka, Wang-Jae Chun, Osamu Enoki, Hideaki Katoh, Masahiro Takenaga, and Atsunori Sonoi. Size-specific catalytic activity of platinum clusters enhances oxygen reduction reactions. *Nature chemistry*, 1(5):397–402, 2009.

[21] Rikson Siburian, Takahiro Kondo, and Junji Nakamura. Size control to a subnanometer scale in platinum catalysts on graphene. *The Journal of Physical Chemistry C*, 117(7):3635–3645, 2013.

[22] Lifeng Dong, Raghavendar Reddy Sanganna Gari, Zhou Li, Michael M Craig, and Shifeng Hou. Graphene-supported platinum and platinum–ruthenium nanoparticles with high electrocatalytic activity for methanol and ethanol oxidation. *Carbon*, 48(3):781–787, 2010.

[23] Brian Seger and Prashant V Kamat. Electrocatalytically active graphene-platinum nanocomposites. role of 2-d carbon support in pem fuel cells. *The Journal of Physical Chemistry C*, 113(19):7990–7995, 2009.

[24] Yanan Tang, Zongxian Yang, and Xianqi Dai. A theoretical simulation on the catalytic oxidation of co on pt/graphene. *Physical Chemistry Chemical Physics*, 14(48):16566–16572, 2012.

[25] K Okazaki-Maeda, Y Morikawa, S Tanaka, and M Kohyama. Structures of pt clusters on graphene by first-principles calculations. *Surface Science*, 604(2):144–154, 2010.

[26] Yasuharu Okamoto. Density-functional calculations of icosahedral m13 (m= pt and au) clusters on graphene sheets and flakes. *Chemical Physics Letters*, 420(4-6):382–386, 2006.

[27] Peng Xu, Lifeng Dong, Mehdi Neek-Amal, Matthew L Ackerman, Jianhua Yu, Steven D Barber, James Kevin Schoelz, Dejun Qi, Fangfang Xu, Paul M Thibado, et al. Self-organized platinum nanoparticles on freestanding graphene. *ACS nano*, 8(3):2697–2703, 2014.

[28] Brian CH Steele and Angelika Heinzel. Materials for fuel-cell technologies. *Nature*, 414(6861):345–352, 2001.

[29] Cheng Wang, Mahesh Waje, Xin Wang, Jason M Tang, Robert C Haddon, and Yushan Yan. Proton exchange membrane fuel cells with carbon nanotube based electrodes. *Nano letters*, 4(2):345–348, 2004.

[30] Anusorn Kongkanand, Susumu Kuwabata, G Girishkumar, and Prashant Kamat. Single-wall carbon nanotubes supported platinum nanoparticles with improved electrocatalytic activity for oxygen reduction reaction. *Langmuir*, 22(5):2392–2396, 2006.

[31] Yougui Chen, Jiajun Wang, Hao Liu, Ruyin Li, Xueliang Sun, Siyu Ye, and Shanna Knights. Enhanced stability of pt electrocatalysts by nitrogen doping in cnts for pem fuel cells. *Electrochemistry communications*, 11(10):2071–2076, 2009.

[32] Sheng-Yang Huang, Prabhu Ganesan, and Branko N Popov. Development of conducting polypyrrole as corrosion-resistant catalyst support for polymer electrolyte membrane fuel cell (pemfc) application. *Applied Catalysis B: Environmental*, 93(1-2):75–81, 2009.

[33] Rod Borup, Jeremy Meyers, Bryan Pivovar, Yu Seung Kim, Rangachary Mukundan, Nancy Garland, Deborah Myers, Mahlon Wilson, Fernando Garzon, David Wood, et al. Scientific aspects of polymer electrolyte fuel cell durability and degradation. *Chemical reviews*, 107(10):3904–3951, 2007.

[34] Daping He, Kun Cheng, Huaiguang Li, Tao Peng, Feng Xu, Shichun Mu, and Mu Pan. Highly active platinum nanoparticles on graphene nanosheets with a significant improvement in stability and co tolerance. *Langmuir*, 28(8):3979–3986, 2012.

[35] Muye Feng, Xi Zhuo Jiang, and Kai H Luo. A reactive molecular dynamics simulation study of methane oxidation assisted by platinum/graphene-based catalysts. *Proceedings of the Combustion Institute*, 37(4):5473–5480, 2019.

[36] P Divya and S Ramaprabhu. Platinum–graphene hybrid nanostructure as anode and cathode electrocatalysts in proton exchange membrane fuel cells. *Journal of Materials Chemistry A*, 2(14):4912–4918, 2014.

[37] Bei Wang, Ying Wang, Jinsoo Park, Hyojun Ahn, and Guoxiu Wang. In situ synthesis of co3o4/graphene nanocomposite material for lithium-ion batteries and supercapacitors with high capacity and supercapacitance. *Journal of Alloys and Compounds*, 509(29):7778–7783, 2011.

[38] Junbo Hou, Yuyan Shao, Michael W Ellis, Robert B Moore, and Baolian Yi. Graphene-based electrochemical energy conversion and storage: fuel cells, supercapacitors and lithium ion batteries. *Physical Chemistry Chemical Physics*, 13(34):15384–15402, 2011.

[39] H Heli, H Yadegari, and A Jabbari. Graphene nanosheets-poly (o-aminophenol) nanocomposite for supercapacitor applications. *Materials Chemistry and Physics*, 134(1):21–25, 2012.

[40] Camelia Berghian-Grosan, Teodora Radu, Alexandru R Biris, Monica Dan, Cezara Voica, Fumiya Watanabe, Alexandru S Biris, and Adriana Vulcu. Platinum nanopar-

ticles coated by graphene layers: A low-metal loading catalyst for methanol oxidation in alkaline media. *Journal of Energy Chemistry*, 40:81–88, 2020.

[41] Yanjun Zhang, Mostafa Hooman, Indrajit Patra, T CH ANIL KUMAR, Hasan Sh Majdi, Samar Emad Izzat, R Sivaraman, Davood Toghraie, Maboud Hekmatifar, and Roozbeh Sabetvand. Mechanical behavior of pt-graphene porous biocompatible nanocomposites prepared by powder metallurgy using molecular dynamics simulation. *Journal of Molecular Liquids*, page 119450, 2022.

[42] P Divya and S Ramaprabhu. Hydrogen storage in platinum decorated hydrogen exfoliated graphene sheets by spillover mechanism. *Physical Chemistry Chemical Physics*, 16(48):26725–26729, 2014.

[43] Cheng-En Cheng, Chi-Yuan Lin, Chien-Hsun Shan, Shang-Yi Tsai, Ko-Wei Lin, Chen-Shiung Chang, and Forest Shih-Sen Chien. Platinum-graphene counter electrodes for dye-sensitized solar cells. *Journal of Applied Physics*, 114(1):014503, 2013.

[44] Andreas Kay and Michael Grätzel. Low cost photovoltaic modules based on dye sensitized nanocrystalline titanium dioxide and carbon powder. *Solar Energy Materials and Solar Cells*, 44(1):99–117, 1996.

[45] QW Jiang, GR Li, and XP Gao. Highly ordered tin nanotube arrays as counter electrodes for dye-sensitized solar cells. *Chemical communications*, (44):6720–6722, 2009.

[46] Chengming Wang, Liang Ma, Lingwen Liao, Song Bai, Ran Long, Ming Zuo, and Yujie Xiong. A unique platinum-graphene hybrid structure for high activity and durability in oxygen reduction reaction. *Scientific reports*, 3(1):1–7, 2013.

[47] SB Sinnott, RJ Colton, CT White, OA Shenderova, DW Brenner, and JA Harrison. Atomistic simulations of the nanometer-scale indentation of amorphous-carbon thin films. *Journal of Vacuum Science & Technology A: Vacuum, Surfaces, and Films*, 15(3):936–940, 1997.

[48] Atomsk: A tool for manipulating and converting atomic data files. https://www.sciencedirect.com/science/article/abs/pii/S0010465515002817, aug 4 2015. [Online; accessed 2022-11-11].

[49] John Edward Jones. On the determination of molecular fields.—ii. from the equation of state of a gas. *Proceedings of the Royal Society of London. Series A, Containing Papers of a Mathematical and Physical Character*, 106(738):463–477, 1924.

[50] Murray S Daw, Stephen M Foiles, and Michael I Baskes. The embedded-atom method: a review of theory and applications. *Materials Science Reports*, 9(7-8):251–310, 1993.

[51] Arthur F Voter. The embedded atom method. *Intermetallic Compounds: Principles*, 1:77, 1994.

[52] Frank H Stillinger and Thomas A Weber. Computer simulation of local order in condensed phases of silicon. *Physical review B*, 31(8):5262, 1985.

[53] D Srolovitz, K Maeda, V Vitek, and T Egami. Structural defects in amorphous solids statistical analysis of a computer model. *Philosophical Magazine A*, 44(4):847–866, 1981.

[54] Jiankuai Diao, Ken Gall, and Martin L Dunn. Surface-stress-induced phase transformation in metal nanowires. *Nature materials*, 2(10):656–660, 2003.

[55] Yuhua Wen, Yang Zhang, and Zizhong Zhu. Size-dependent effects on equilibrium stress and strain in nickel nanowires. *Physical Review B*, 76(12):125423, 2007.

[56] J Dana Honeycutt and Hans C Andersen. Molecular dynamics study of melting and freezing of small lennard-jones clusters. *Journal of Physical Chemistry*, 91(19):4950–4963, 1987.

[57] Soumya Saswati Sarangi. Study on young's modulus of metallic nanowires using classical molecular dynamics simulations. *Materials today: Proceedings*, 41:413–415, 2021.

[58] XW Zhou, RA Johnson, and HNG Wadley. Misfit-energy-increasing dislocations in vapor-deposited cofe/nife multilayers. *Physical Review B*, 69(14):144113, 2004.

[59] Jian Chen and Kwong-Yu Chan. Size-dependent mobility of platinum cluster on a graphite surface. *Molecular Simulation*, 31(6-7):527–533, 2005.

[60] Yu-Hua Wen, Rao Huang, Zi-Zhong Zhu, and Quan Wang. Mechanical properties of platinum nanowires: An atomistic investigation on single-crystalline and twinned structures. *Computational Materials Science*, 55:205–210, 2012.

[61] Steven Y. Liem and Kwong-Yu Chan. Simulation study of platinum adsorption on graphite using the sutton-chen potential. *Surface Science*, 328(1):119–128, 1995.

[62] atsim.potentials - Potential Model Tabulation for Atomic Scale Simulation — atsim.potentials documentation.

https://atsimpotentials.readthedocs.io/en/latest/index.html. [Online; accessed 2022-12-10].

[63] Charles Kittel. *Solid state physics*, volume 3. Shell Development Company, 1955.

[64] MZ Hossain, T Hao, and B Silverman. Stillinger–weber potential for elastic and fracture properties in graphene and carbon nanotubes. *Journal of Physics: Condensed Matter*, 30(5):055901, 2018.

[65] Mallika Arachchige and Nuwan Dewapriya. *Molecular dynamics study of effects of geometric defects on the mechanical properties of graphene*. PhD thesis, University of British Columbia, 2012.

[66] Luke S Walker, Victoria R Marotto, Mohammad A Rafiee, Nikhil Koratkar, and Erica L Corral. Toughening in graphene ceramic composites. *ACS nano*, 5(4):3182–3190, 2011.

[67] Peng Zhang, Lulu Ma, Feifei Fan, Zhi Zeng, Cheng Peng, Phillip E Loya, Zheng Liu, Yongji Gong, Jiangnan Zhang, Xingxiang Zhang, et al. Fracture toughness of graphene. *Nature communications*, 5(1):1–7, 2014.

[68] Teng Zhang, Xiaoyan Li, and Huajian Gao. Fracture of graphene: a review. *International Journal of Fracture*, 196(1):1–31, 2015.

[69] JJPRB Tersoff. Modeling solid-state chemistry: Interatomic potentials for multicomponent systems. *Physical review B*, 39(8):5566, 1989.

[70] J Tersoff. Empirical interatomic potential for carbon, with applications to amorphous carbon. *Physical Review Letters*, 61(25):2879, 1988.

[71] Jerry Tersoff. New empirical approach for the structure and energy of covalent systems. *Physical review B*, 37(12):6991, 1988.

[72] Carla de Tomas, Irene Suarez-Martinez, and Nigel A Marks. Graphitization of amorphous carbons: A comparative study of interatomic potentials. *Carbon*, 109:681–693, 2016.

[73] L Lindsay and DA Broido. Optimized tersoff and brenner empirical potential parameters for lattice dynamics and phonon thermal transport in carbon nanotubes and graphene. *Physical Review B*, 81(20):205441, 2010.

[74] AJ Dyson and PV Smith. Extension of the brenner empirical interatomic potential to c si h systems. *Surface science*, 355(1-3):140–150, 1996.

[75] Donald W Brenner, Olga A Shenderova, Judith A Harrison, Steven J Stuart, Boris Ni, and Susan B Sinnott. A second-generation reactive empirical bond order (rebo) potential energy expression for hydrocarbons. *Journal of Physics: Condensed Matter*, 14(4):783, 2002.

[76] Steven J Stuart, Alan B Tutein, and Judith A Harrison. A reactive potential for hydrocarbons with intermolecular interactions. *The Journal of chemical physics*, 112(14):6472–6486, 2000.

[77] F Memarian, A Fereidoon, and M Darvish Ganji. Graphene young's modulus: Molecular mechanics and dft treatments. *Superlattices and Microstructures*, 85:348–356, 2015.

[78] Hanqing Yin, H Jerry Qi, Feifei Fan, Ting Zhu, Baolin Wang, and Yujie Wei. Griffith criterion for brittle fracture in graphene. *Nano letters*, 15(3):1918–1924, 2015.

[79] Pattabhi R Budarapu, Brahmanandam Javvaji, VK Sutrakar, D Roy Mahapatra, Goangseup Zi, and Timon Rabczuk. Crack propagation in graphene. *Journal of Applied Physics*, 118(6):064307, 2015.

[80] Dieter B Brommer and Markus J Buehler. Failure of graphdiyne: structurally directed delocalized crack propagation. *Journal of Applied Mechanics*, 80(4):040908, 2013.

[81] Ashivni Shekhawat and Robert O Ritchie. Toughness and strength of nanocrystalline graphene. *Nature communications*, 7(1):1–8, 2016.

[82] Steven Y Liem and Kwong-Yu Chan. Simulation study of platinum adsorption on graphite using the sutton-chen potential. *Surface Science*, 328(1-2):119–128, 1995.

[83] Samaneh Nasiri, Christian Greff, Kai Wang, Mingjun Yang, Qianqian Li, Paolo Moretti, and Michael Zaiser. Multilayer structures of graphene and pt nanoparticles: A multiscale computational study. *Advanced Engineering Materials*, 22(9):2000207, 2020.

[84] Dennis C Rapaport and Dennis C Rapaport Rapaport. *The art of molecular dynamics simulation*. Cambridge university press, 2004.

[85] M Scott Shell. *Thermodynamics and statistical mechanics: an integrated approach*. Cambridge University Press, 2015.

[86] Daan Frenkel and Berend Smit. *Understanding molecular simulation: from algorithms to applications*, volume 1. Elsevier, 2001.

[87] Tamar Schlick, Eric Barth, and Margaret Mandziuk. Biomolecular dynamics at long timesteps: Bridging the timescale gap between simulation and experimentation. *Annual review of biophysics and biomolecular structure*, 26(1):181–222, 1997.

[88] Joseph R Davis. *Tensile testing*. ASM international, 2004.

[89] William F Hosford. *Mechanical behavior of materials*. Cambridge university press, 2010.

[90] John S Hutchinson. *Concept Development Studies in Chemistry (OpenStax)*. OpenStax CNX, 2013.

[91] A. P. Thompson, H. M. Aktulga, R. Berger, D. S. Bolintineanu, W. M. Brown, P. S. Crozier, P. J. in 't Veld, A. Kohlmeyer, S. G. Moore, T. D. Nguyen, R. Shan, M. J. Stevens, J. Tranchida, C. Trott, and S. J. Plimpton. LAMMPS - a flexible simulation tool for particle-based materials modeling at the atomic, meso, and continuum scales. *Comp. Phys. Comm.*, 271:108171, 2022.

[92] Jiankuai Diao, Ken Gall, Martin L Dunn, and Jonathan A Zimmerman. Atomistic simulations of the yielding of gold nanowires. *Acta Materialia*, 54(3):643–653, 2006.

[93] Thomas H Courtney. *Mechanical behavior of materials*. Waveland Press, 2005.

[94] Wei Cai, William Fong, Erich Elsen, and Christopher R Weinberger. Torsion and bending periodic boundary conditions for modeling the intrinsic strength of nanowires. *Journal of the Mechanics and Physics of Solids*, 56(11):3242–3258, 2008.

[95] Jiankuai Diao, Ken Gall, and Martin L Dunn. Atomistic simulation of the structure and elastic properties of gold nanowires. *Journal of the Mechanics and Physics of Solids*, 52(9):1935–1962, 2004.

[96] Bryan Harris et al. Engineering composite materials. 1999.

[97] XJ Long, B Li, L Wang, JY Huang, J Zhu, and SN Luo. Shock response of cu/graphene nanolayered composites. *Carbon*, 103:457–463, 2016.

[98] Hooke's law - Wikipedia. https://en.wikipedia.org/wiki/Hooke2017. [Online; accessed 2022-12-19].

[99] JM Gere. Mechanics of materials, brooks/cole, a division of thomson learning. *Inc., Belmont, CA*, 2004.

[100] Mohammad Din Al Amin, Mohammad Minhaz Uddin, and Md Alamgir Hossain. Molecular dynamics simulation to evaluate flexural properties of cu nanowires under different loading conditions. *North American Academic Research*, 5(9):124–137, 2022.

[101] Stephen Timoshenko. *History of strength of materials: with a brief account of the history of theory of elasticity and theory of structures*. Courier Corporation, 1953.

[102] LD Landau and EM Lifshitz. Theory of elasticity, oxford, 1986.

[103] Stephen P Timoshenko and James M Gere. Theory of elastic stability, mcgraw-hill book company. *New York*, 1961.

[104] HF Zhan and YuanTong Gu. Theoretical and numerical investigation of bending properties of cu nanowires. *Computational Materials Science*, 55:73–80, 2012.

[105] HF Zhan, YuanTong Gu, Cheng Yan, Xi-Qiao Feng, and PKDV Yarlagadda. Numerical exploration of plastic deformation mechanisms of copper nanowires with surface defects. *Computational Materials Science*, 50(12):3425–3430, 2011.

[106] ET Lilleodden, JA Zimmerman, SM Foiles, and WD Nix. Atomistic simulations of elastic deformation and dislocation nucleation during nanoindentation. *Journal of the Mechanics and Physics of Solids*, 51(5):901–920, 2003.

[107] Ian M Hutchings. Leonardo da vincis studies of friction. *Wear*, 360:51–66, 2016.

[108] Duncan Dowson. *History of tribology*. Addison-Wesley Longman Limited, 1978.

[109] Huajian Gao, Xiang Wang, Haimin Yao, Stanislav Gorb, and Eduard Arzt. Mechanics of hierarchical adhesion structures of geckos. *Mechanics of materials*, 37(2-3):275–285, 2005.

[110] Nianhuan Chen, Nobuo Maeda, Matthew Tirrell, and Jacob Israelachvili. Adhesion and friction of polymer surfaces: the effect of chain ends. *Macromolecules*, 38(8):3491–3503, 2005.

[111] Susan B Sinnott, Seong-Jun Heo, Donald W Brenner, Judith A Harrison, and Douglas L Irving. Computer simulations of nanometer-scale indentation and friction. In *Nanotribology and Nanomechanics*, pages 301–370. Springer, 2017.

[112] Daniel Matté, GL Rech, LM Leidens, JE Zorzi, AF Michels, CA Figueroa, and CA Perottoni. Molecular dynamics simulations of the isotopic effect on nanoscale friction. *Applied Physics A*, 127(9):1–9, 2021.

[113] Jun Shimizu, Hiroshi Eda, Masashi Yoritsune, and Etsuji Ohmura. Molecular dynamics simulation of friction on the atomic scale. *Nanotechnology*, 9(2):118, 1998.

[114] Matthew J Brukman, Guangtu Gao, Robert J Nemanich, and Judith A Harrison. Temperature dependence of single-asperity diamond- diamond friction elucidated using afm and md simulations. *The Journal of Physical Chemistry C*, 112(25):9358–9369, 2008.

[115] Christian Greiner, Jonathan R Felts, Zhenting Dai, William P King, and Robert W Carpick. Local nanoscale heating modulates single-asperity friction. *Nano letters*, 10(11):4640–4645, 2010.

[116] Lars Jansen, Hendrik Hölscher, Harald Fuchs, and André Schirmeisen. Temperature dependence of atomic-scale stick-slip friction. *Physical review letters*, 104(25):256101, 2010.

[117] Ludwig Prandtl. A conceptual model to the kinetic theory of solid bodies. *Z. Angew. Math. Mech*, 8:85–106, 1928.

[118] André Schirmeisen, Lars Jansen, Hendrik Hölscher, and Harald Fuchs. Temperature dependence of point contact friction on silicon. *Applied physics letters*, 88(12):123108, 2006.

[119] Xueying Zhao, Simon R Phillpot, W Gregory Sawyer, Susan B Sinnott, Scott S Perry, et al. Transition from thermal to athermal friction under cryogenic conditions. *Physical review letters*, 102(18):186102, 2009.

[120] Itay Barel, Michael Urbakh, Lars Jansen, and André Schirmeisen. Multibond dynamics of nanoscale friction: the role of temperature. *Physical Review Letters*, 104(6):066104, 2010.

[121] AE Filippov, J Klafter, and M Urbakh. Friction through dynamical formation and rupture of molecular bonds. *Physical Review Letters*, 92(13):135503, 2004.

[122] Jianping Gao, WD Luedtke, D Gourdon, M Ruths, JN Israelachvili, and Uzi Landman. Frictional forces and amontons' law: from the molecular to the macroscopic scale, 2004.

[123] O Pietrement and M Troyon. Study of the interfacial shear strength pressure dependence by modulated lateral force microscopy. *Langmuir*, 17(21):6540–6546, 2001.

[124] WC Milz and LE Sargent. Frictional characteristics of plastics. *Lubrication Eng*, 11:313–317, 1955.

[125] Kyuichiro Tanaka. Kinetic friction and dynamic elastic contact behaviour of polymers. *Wear*, 100(1-3):243–262, 1984.

[126] GV Vinogradov, GM Bartenev, AI El'Kin, and VK Mikhaylov. Effect of temperature on friction and adhesion of crystalline polymers. *Wear*, 16(3):213–219, 1970.

[127] NK Myshkin and AV Kovalev. Polymer tribology. *Sinha, S*, pages 3–37, 2009.

[128] Zhen-Dong Sha, Viacheslav Sorkin, Paulo S Branicio, Qing-Xiang Pei, Yong-Wei Zhang, and David J Srolovitz. Large-scale molecular dynamics simulations of wear in diamond-like carbon at the nanoscale. *Applied Physics Letters*, 103(7):073118, 2013.

[129] JeFoa Archard. Contact and rubbing of flat surfaces. *Journal of applied physics*, 24(8):981–988, 1953.

[130] Xiaoli Hu and Ashlie Martini. Atomistic simulation of the effect of roughness on nanoscale wear. *Computational Materials Science*, 102:208–212, 2015.

[131] B Gotsmann and MA Lantz. Quantized thermal transport across contacts of rough surfaces. *Nature materials*, 12(1):59–65, 2013.

[132] Chaiyapat Tangpatjaroen, David Grierson, Steve Shannon, Joseph E Jakes, and Izabela Szlufarska. Size dependence of nanoscale wear of silicon carbide. *ACS Applied Materials & Interfaces*, 9(2):1929–1940, 2017.

[133] Robert W Carpick, N Agrait, DF Ogletree, and Miguel Salmeron. Measurement of interfacial shear (friction) with an ultrahigh vacuum atomic force microscope. *Journal of Vacuum Science & Technology B: Microelectronics and Nanometer Structures Processing, Measurement, and Phenomena*, 14(2):1289–1295, 1996.

[134] Binquan Luan and Mark O Robbins. The breakdown of continuum models for mechanical contacts. *Nature*, 435(7044):929–932, 2005.

[135] Binquan Luan and Mark O Robbins. Contact of single asperities with varying adhesion: Comparing continuum mechanics to atomistic simulations. *Physical Review E*, 74(2):026111, 2006.

[136] Yifei Mo, Kevin T Turner, and Izabela Szlufarska. Friction laws at the nanoscale. *Nature*, 457(7233):1116–1119, 2009.

[137] Tevis DB Jacobs and Robert W Carpick. Nanoscale wear as a stress-assisted chemical reaction. *Nature nanotechnology*, 8(2):108–112, 2013.

[138] Liangchi Zhang and Hiroaki Tanaka. Towards a deeper understanding of wear and friction on the atomic scale—a molecular dynamics analysis. *Wear*, 211(1):44–53, 1997.

[139] Harish Bhaskaran, Bernd Gotsmann, Abu Sebastian, Ute Drechsler, Mark A Lantz, Michel Despont, Papot Jaroenapibal, Robert W Carpick, Yun Chen, and Kumar Sridharan. Ultralow nanoscale wear through atom-by-atom attrition in silicon-containing diamond-like carbon. *Nature nanotechnology*, 5(3):181–185, 2010.

[140] W Maw, F Stevens, SC Langford, and JT Dickinson. Single asperity tribochemical wear of silicon nitride studied by atomic force microscopy. *Journal of Applied Physics*, 92(9):5103–5109, 2002.

Appendix A

Sample LAMMPS input file

Listing A.1: Input file for tensile test simulation

```

#-----Adjustable Variables--------

variable      tmprtr equal 300.0
variable      sRate equal 0.001

# ------ INITIALIZATION ----------
clear
units              metal
dimension          3
boundary           p       s  s
atom_style         atomic
newton             on
neighbor           2.0 bin
neigh_modify       delay 5

# ----- ATOM DEFINITION ----------
read_data          NC1layers.lmp

#--------Force Fields-------------

pair_style         hybrid/overlay sw eam/alloy morse 12.0
pair_coeff         * * sw C.sw NULL C
pair_coeff         * * eam/alloy Pt_sutton.eam.alloy Pt NULL
pair_coeff         1 2 morse 0.0071 1.05 4.18 12.0

#--------Equilibration------------

min_style          cg
```

```
minimize           1e-25 1e-25 5000 10000

reset_timestep     0
timestep           0.001   # 1fs

velocity           all create ${tmprtr} 55472333 dist gaussian
fix                1 all nvt temp ${tmprtr} ${tmprtr} 0.05

thermo             1000
thermo_style       custom step temp pe lx ly lz press
                   pxx pyy pzz

run                10000

unfix              1
#---Initial Length for Strain Calculation---
variable           tmp equal ”lx”
variable           L0 equal ${tmp}
print              ”Initial Length, L0: ${L0}”

#--------------Deformation------------------
reset_timestep     0

fix                1 all npt temp ${tmprtr} ${tmprtr} 0.5
                   y 0 0 1 z 0 0 1 drag 1
fix                2 all deform 1 x erate ${sRate} units box
                   remap x

#-------------Strain-Stress----------------
variable           strain equal ”(lx - v_L0) / v_L0”
variable           stress equal ”-pxx/10000”

fix                3 all print 100 ”${strain}    ${stress}”
                   title ”Strain Stress” file
                   DataSheet_NC_Layer1_300K.txt screen no

#---------------Visualization--------------
dump               1 all cfg 250 dump/dump.tensile_*.cfg mass
                   type xs ys zs fx fy fz
dump_modify        1 element Pt C

restart            10000 restart/restart.tension

thermo             1000
thermo_style       custom step temp v_strain v_stress pe ke
```

```

run                 200000

########################################
print               "Simulation Done"
```

Appendix B

Sample Matlab Code: Bending analysis

We will be using a library to plot, which will be added path by the following code:

```
addpath(location of PlotPub library);
```

We need to analyse from where the bending is started to take effect and manipulate the data table to make a new one

```
initHeight = 47.4408; % from simulation
maxMaterialHeight = 35.64512; % from material lmp file
indenterRadius = 10; % defined in simulation file
timeStep = 0.001; % defined in simulation; in general 1 fs
factorSpeedConvert = (1e-10/1e-12); % A/fs
indenterSpeed = 10 * factorSpeedConvert; % speed in m/s

initGap = (initHeight - maxMaterialHeight) - indenterRadius;
Displacement = FD.Displacement - round(initGap);
Displacement = Displacement(Displacement >=0) * 0.1;
Force = FD.Force(Displacement >=0);
ForceMean = movmean(Force, 50);
FD_R = table(Displacement,Force, ForceMean);
writetable(FD_R);
```

Now lets Plot this

```
plt = Plot(FD_R.Displacement, FD_R.Force,
           FD_R.Displacement, FD_R.ForceMean);
```

Some Properties are needed to be tweaked

```
plt = Plot(FD_R.Displacement, FD_R.Force,
plt.Colors = {[0.8, 0.9, 1], [0.9300 0 0]};
plt.XLabel = 'Displacement (nm)';
plt.YLabel = 'Force (nN)';
plt.FontName = 'Arial';
plt.FontSize = 12;
```

Exporting the file as png

```
plt.export('force_deflection_curve.png');
```

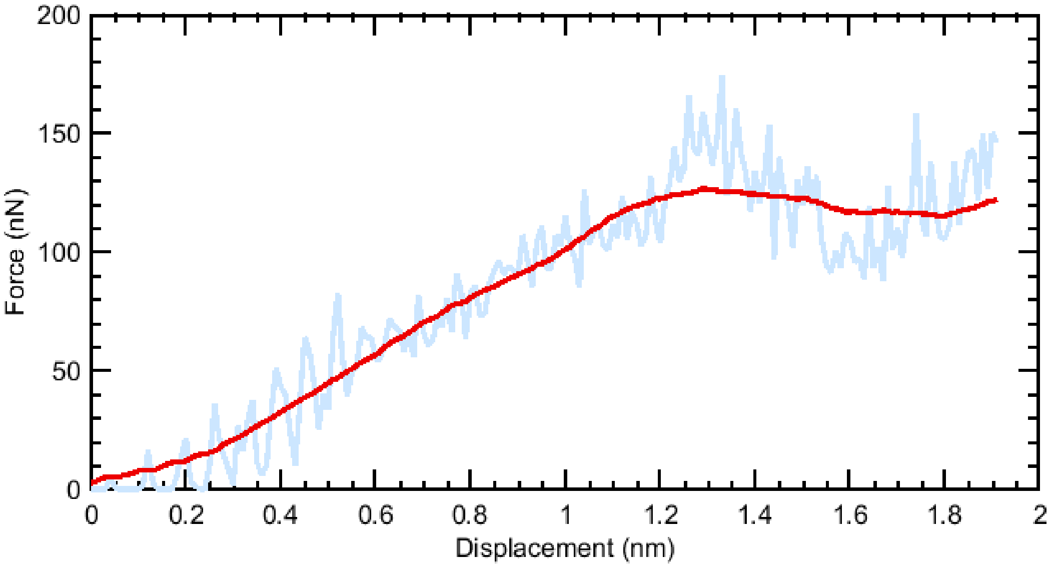

Figure B.1: force_deflection_curve.png

Now the analysis part for flexural stress

```
%input the dimensions of the simulation box
l = input('Length of the box (nm): ');
b = input('Width of the box (nm): ');
h = input(”Height of the box (nm): ”);

% Slope of the curve
% We will take the mid range of the proportional limit
forceDefSlope = polyfit(FD_R.Displacement(40:70),
                        FD_R.ForceMean(40:70),1);

% Maximum Deflection within proportional limit
% Range should be calculated from simulation movie
% Maximum deflection would be counted as nm
totFrame = input('Total Frame in Simulation: ');
failFrame = input('Last frame upto elastic limit: ');
factorToBeDeleted =
 length(FD_R.Displacement)/length(FD.Displacement);
totFrame = round(totFrame * factorToBeDeleted);
failFrame = round(failFrame * factorToBeDeleted);
rangeDef = (failFrame/totFrame) * length(FD_R.Displacement);
maxDeflection = max(FD_R.Displacement(1:round(rangeDef)));

% Equations for calculation
A = b*h; % Area
I = (b*h^3)/12; % Moment of Inertia
s = maxDeflection^2 * A / I;
k = (6*s*(140+s))/(350+(3*s));
f = k/(48 - ((192*tanh(sqrt(k)/4))/sqrt(k)));

% Euler Beam Bending Formula
eulerEq = (forceDefSlope * l^3)/(192*I);
% Modified Euler Beam Bending Formula
modEulerEq = (forceDefSlope*l^3)/(192*k*I);
% Yield Force
yieldForce = (3*f*l)/(4*h^3);
```

Lets print the values now

```
disp(”Flexural stress with Euler equation: ”
     + num2str(eulerEq(1)) + ” GPa”);
```

Flexural stress with Euler equation: 3.4509 GPa

```
disp(”Flexural stress with Modified Euler equation: ”
     + num2str(modEulerEq(1)) + ” GPa”);
```

Flexural stress with Modified Euler equation: 15.5545 GPa

```
disp("Yield force: " + num2str(yieldForce(1)) + " GPa");
```

Yield force: 0.023162 GPa